공학박사학위논문

Phase Stability and Electrical Property of Amorphous Materials for Electronic Devices Investigated by Mechanical Stress

기계적 응력 측정을 통한 전자 소자용 비정질 재료의 상 안정성과 전기적 특성 연구

2014년 8월

서울대학교 대학원

재료공학부

조 주 영

기계적 응력 측정을 통한 전자 소자용 비정질 재료의 상 안정성과 전기적 특성 연구

PHASE STABILITY AND ELECTRICAL PROPERTY OF AMORPHOUS MATERIALS FOR ELECTRONIC DEVICES INVESTIGATED BY MECHANICAL STRESS

지도교수: 주 영 창

이 논문을 공학박사 학위논문으로 제출함

2014년 8월

서울대학교 대학원

재료공학부

조 주 영

조 주 영의 박사학위 논문을 인준함

2014년 7월

위 원 장	김 기 범	(인)
부 위 원 장	주 영 창	(인)
위 원	한 승 우	(인)
위 원	안 동 호	(인)
위 원	최 인 석	(인)

ABSTRACT

Phase Stability and Electrical Property of Amorphous Materials for Electronic Devices Investigated by Mechanical Stress

Ju-Young Cho
Department of Materials Science and Engineering
The Graduate School
Seoul National University

Amorphous materials have been applied in multi-functional devices because of their unique properties, which originate from disordered atomic structures and are distinct from crystalline materials. The characteristic transformation behavior and associated changes in the electrical properties of amorphous phase change materials allows them to be used in phase-change random access memory (PcRAM). In addition, the uniformity over large areas, transparency and high carrier mobility of amorphous oxide semiconductors allow them to be used in thin-film transistors (TFTs) for large displays.

However, electronic devices based on amorphous materials have suffered from reliability issues due to their phase instability. In contrast to crystalline solids, amorphous materials are not in equilibrium; therefore, several structural changes occur (e.g., structural relaxation, glass transition and crystallization), which lead to changes in their material properties as a function of time or temperature.

Therefore, it is crucial to characterize and tune the structural stability of amorphous materials to be consistent with the device characteristics. An experimental mechanical

stress analysis using substrate curvature measurement was utilized to detect structural changes. In addition, a fundamental theoretical understanding of the unique structural features of amorphous materials was established based on atomic-scale networks.

To attain high switching speeds and stability of PcRAM, the characteristic kinetics of crystallization in amorphous phase change materials (non-Arrhenius temperature dependence of the crystal growth velocity) need to be explored. The crystallization temperature (T_x), glass transition temperature (T_g), and super-cooled liquid region (T_x - T_g) of amorphous $Ge_2Sb_2Te_5$ (GST) films doped with various elements were measured using mechanical stress analysis. In addition, the viscosity and the fragility were determined from the heating rate dependence of T_g to describe the atomic mobility. The distinct effects of the dopants originated from the changes in free volume and bonding enthalpy by interstitial and substitutional doping. In comparison to the PcRAM characteristics, the effects of doping on the phase stability and atomic mobility successfully match the data retention and SET speed, respectively.

The time-dependent drift of resistance in amorphous GST leads to reliability problems in PcRAM, which is called resistance drift. The microscopic origin of resistance drift has been explained using several models, including the defect annihilation model and the strained bandgap model. To reveal the relationship between the microscopic model of kinetic behaviors in glass (e.g., structural relaxation) and resistance drift, novel real-time measurements of mechanical stress and electrical resistance were conducted on amorphous GST films. The time-dependent resistance was calculated based on the model and compared to the measured resistance and showed that defect annihilation can explain the time-dependent drift of resistance in amorphous GST films.

Amorphous In-Ga-Zn-O (a-IGZO) is a promising active material for thin-film transistors (TFT); however, it experiences structural instability, which originates from

the surface. The surface-to-volume ratios of a-IGZO films were varied by changing the thickness. Using mechanical stress analysis, T_g (423 - 562 ℃) and fragility (18 - 26) were observed in a-IGZO films. Based on the thickness dependence of T_g and fragility, the structural stability of a-IGZO was reduced significantly as the thickness decreased due to the effect of the unstable surface layer.

This study investigated the phase stability and electrical properties of amorphous materials and unraveled the physics that are relevant to the microscopic origins of the structural changes using mechanical stress analysis. A thorough analysis of the experimental data in conjunction with theoretical models helped to build a framework to describe and explain the unconventional properties of amorphous materials that are used in electronic devices.

Keywords: Amorphous materials, crystallization, phase-change random access memory (PcRAM), $Ge_2Sb_2Te_5$, In-Ga-Zn-O, mechanical stress analysis

***Student Number*:** 2009-20641

Table of Contents

LIST OF TABLES

LIST OF FIGURES

Figure 2.4 Schematic of the transformation of a liquid to an amorphous material by rapid cooling. A solid material with a disordered structure (like frozen liquid) will form as the glass transition temperature is reached and is referred to as glass.

Figure 2.5 The Angell plot shows the temperature dependence of viscosity (or relaxation time) in the super-cooled liquid. Fragility is quantified by measuring the slope of the logarithm of the viscosity as a function of T_g/T at $T = T_g$.

Figure 2.6 Mapping of physical properties of phase change materials with various compositions. Two coordinates are used: *s-p* hybridization (i.e., "covalency", which is determined by the split between the valence s- and p-states) on the y-axis and ionicity on the x-axis.

Figure 2.7 Crystal-growth rates of Si, SiO_2 and $Ge_2Sb_2Te_5$ as a function of temperature. While Si and SiO_2 show classic Arrhenius behaviors (strong glasses), $Ge_2Sb_2Te_5$ displays a very different fragile behavior.

Figure 2.8 Schematic image of orbital drawings that determine the carrier transport in crystalline and amorphous semiconductors for (a) covalent bonding systems and (b) ionic bonding systems. For the conventional case of covalent semiconductors (e.g., a-Si or crystalline Si), carrier transport occurs via sp^3 orbitals, which are strongly sensitive to the bond angle of the atomic network.

Figure 2.9 (a) Tendency of amorphous formation (phase stability of the amorphous state) of In_2O_3-Ga_2O_3-ZnO thin films for various stoichiometries. Measured data are denoted by closed circles, and unmeasured data are denoted by open circles. (b) High phase stability of amorphous In-Ga-Zn-O due to the large size and charge mismatch between the ions, which leads to high stability.

Figure 2.10 (a) Schematic description of the less-constrained bond in the surface region, which results in high atomic mobility. (b) Fraction of $X^{[5]}Al$ in an amorphous Al_2O_3 thin film as a function of a decrease in the deposition thickness from 1.4 mm to 5 nm.

Figure 2.11 Substrate curvature due to mechanical stress in the thin film caused by volumetric changes in the thin film.

Figure 2.12 (a) Schematic of the bending of a thin plate when a biaxial stress is developed on the upper face; the stress distribution is shown in the cross-section. (b) Schematic of the radius of curvature for a bending plate.

Figure 2.13 Force equilibrium in a thin film on a substrate, which results in the edge force being divided into the normal stress and the bending moment.

Figure 2.14 Schematic of film with volumetric changes removed from the substrate and attached to the substrate. In the removed film, the isotropic volume change occurs in the film. If the film is attached to the substrate, biaxial strain is produced.

Figure 3.1 Dopant concentrations in the $Ge_2Sb_2Te_5$ films as a function of deposition conditions detected by Rutherford backscattering spectrometry (RBS). (a) N concentration as a function of the N_2 flow rate. (b) Bi concentration as a function of the DC power of the $Ge_2Bi_2Te_5$ target. (c) C concentration as a function of the RF power of the C target. (d) Al concentration as a function of the RF power of the Al target.

Figure 3.2 Schematic of the substrate curvature measurement system using a multi-beam optical sensor (MOS). An array of parallel beams irradiates the bended substrate and is reflected. The reflected beams are detected by a CCD camera [*k*-Space Associates, Inc.].

Figure 3.3 Real-time substrate curvature measurement using a multi-beam optical sensor (MOS) set up in the laboratory. The curvature is determined from the beam spacing, and the biaxial stress of the film was then determined from the changes in curvature according to the Stoney equation.

Figure 4.9 (a) Apparent activation energy and (b) fragility obtained from the linear slopes in Figure 4.8(b) at $T = T_g$ for pure and Al-, Bi-, C- and N-GST.

Figure 4.10 Extrapolated curves of the logarithm of the viscosity as a function of T_g/T according to the Vogel-Fulcher-Tammann relation for (a) Al 8.5 at.% GST, (b) Bi 9.6 at.% GST, (c) C 10 at.% GST and (d) N 10 at.% GST in comparison with pure GST and Arrhenius behavior.

Figure 4.11 (a) Extrapolated curves of the logarithm of the viscosity as a function of the reciprocal of temperature according to the Vogel-Fulcher-Tammann relation for Al 8.5 at.%, Bi 9.6 at.% C 10 at.% and N 10 at.% GST (Arrhenius behavior) in comparison with pure GST. (b) Magnified view of (a).

Figure 4.12 Maps of amorphous $Ge_2Sb_2Te_5$ tuned by various dopants as a function of (a) glass transition temperature (T_g) and fragility and (b) glass transition temperature (T_g) and the super-cooled liquid region ($T_x - T_g$). The vertical axis describes the thermal stability against crystallization (bonding enthalpy), and the horizontal axis describes the atomic mobility (free volume).

Figure 4.13 Map of PcRAM characteristics as a function of 10 yr data retention and SET time for various phase change materials and dopants[1-13] showing the successful match with Figure 4.12.

CHAPTER 1

Introduction

1.1. Electronic devices employing amorphous materials

The evolution of micro- and nano-electronics is moving toward multi-functional and process-friendly devices. This evolution of devices necessarily requires the development of component materials that determine the performance and the reliability of the devices. The usual choice for active materials in micro- and nano-electronics has been crystalline semiconducting materials, which have periodicity in their atomic structure. Crystalline semiconductors have been superior candidates due to their high carrier mobility, which results in good device performance. However, because electronics have encountered difficulties with increasing speed and decreasing size, the need for devices with new operating principles has increased. As large energy devices (e.g., solar cells) and display devices have developed, the need for low-cost and process-friendly devices has also increased.

Amorphous materials, which form a subgroup of amorphous semiconductors, have been actively applied in multi-functional and process-friendly devices because of their unique properties.[1] Amorphous material refers to solid materials with disordered atomic structures similar to liquid materials and distinct from crystalline materials with ordered atomic structures.

The disordered structure of amorphous materials impedes the motion of the mobile electrons that make up the electrical current in the material and results in lower mobility than in crystalline materials. The combination of the insulating characteristics of amorphous materials and the transformation characteristics of amorphous semiconductors enables their application in storage devices (e.g., phase change random access memory, PcRAM).

In addition, the use of amorphous materials enables low temperature processes because there is no need for subsequent crystallization followed by the synthesis of film, which usually requires a high temperature. Low temperature processes are important in selecting the component material in the design of devices. Furthermore, in contrast to the fact that grain boundaries are present in crystal structures, amorphous materials contain no grain boundaries because there is no regularity (e.g., amorphous Si and amorphous oxide semiconductors). Therefore, amorphous materials can be used to maintain uniform properties over large areas.

In applications of amorphous materials, it is crucial to characterize and describe the unconventional properties of the materials that are relevant to the device characteristics. Achieving this goal requires a breakthrough in our understanding of the unique structural features of amorphous materials that depend on atomic-scale networks.

1.2. Practical issues in PcRAM

Among the many material systems, chalcogenides, and particularly the subgroup of phase change materials, exhibit extremely short crystallization times (a few nanoseconds). However, crystallization in this class of materials is accompanied by significant changes in optical and electrical properties.[2] In addition, the crystallization behavior can be controlled to occur only in a very small area of a few nanometers. Because of this unique combination of properties, phase change materials are employed in rewriteable optical data storage media. More recently, they have been implemented in phase-change random access memory (PcRAM), which is an ultra-fast, highly integrated nonvolatile memory device.

The operating principle of PcRAM is the reversible amorphous-to-crystalline phase transitions in a phase change material. As depicted in **Figure 1.1(a)**, the logical state of PcRAM is determined by the difference in resistance between the amorphous and crystalline states; the amorphous state is characterized by a disordered structure, which results in a high resistance (equivalent to a binary '0'). Conversely, the crystalline state is characterized by an ordered structure that results in a low resistance (equivalent to a binary '1'). The switch from the crystalline state to the amorphous state is referred to as the RESET and is induced by amorphization. The switch from the amorphous state to the crystalline state is referred to as the SET and is induced by crystallization. **Figure 1.1(b)** shows a schematic of a single PcRAM cell with the most typical mushroom-shaped structure.[3] The switching process described above only occurs in the programmable region that is triggered by electric current-induced heating in the heater. The logical state of the programmable region is controlled by the temperature change induced by the electrical pulses as depicted in **Figure 1.1(c)**.[3]

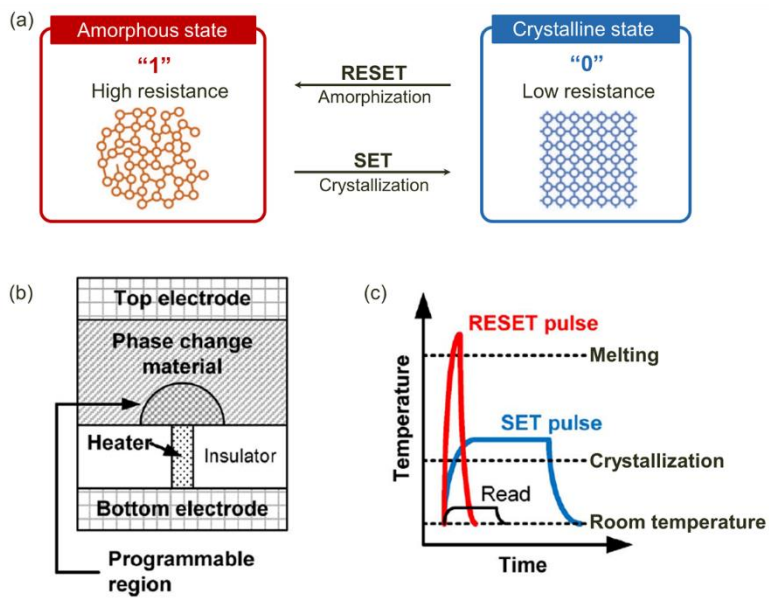

Figure 1.1 (a) The operating principle of PcRAM is the reversible amorphous-to-crystalline phase transitions in a phase change material. (b) Schematic cross-section of a single PcRAM cell with the most typical mushroom-shaped structure.[3] (c) The logical state of the programmable region is determined by a temperature change induced by electrical pulses.[3]

The operating principle of PcRAM enables non-volatility and a relatively rapid switching speed (~a few tens of nanoseconds),[4] which will be successfully commercialized in the near future in the market of nonvolatile memory as an alternative to flash memory technology. However, PcRAM also suffers from reliability issues, such as resistance drift[5] and retention issues,[6] that originate from the instability of the amorphous state of phase change materials.

First, the loss of information stored in the high-resistance state, which is called data retention loss, inhibits the reliability of PcRAM. As shown in **Figure 1.2(a)**, the resistance of a RESET state of a PcRAM cell decreases with time at an elevated temperature (180 ℃); this is data retention loss induced by crystallization. Arrhenius fitting of the failure time as a function of $1/kT$ is used to predict the failure time of a PcRAM cell as shown in **Figure 1.2(b)**.[7] This problem stems from crystallization kinetics, which describe the interplay of time and temperature on the amorphous state. While crystallization can occur at very short time scales (~a few nanoseconds) at a high temperature, it can also take a very long time (~a few decades) at a low temperature for the same compound, as depicted in **Figure 1.3**. Fast crystallization at elevated temperatures determines the SET speed of phase change memory (i.e., the maximum speed to write information), so faster crystallization behavior is advantageous for the operation speed of PcRAM. In contrast, crystallization that occurs at low temperatures is a major cause of data retention loss, which negatively affects the reliability of PcRAM. Hence, we need to identify materials that enable rapid crystallization at elevated temperatures but are very stable at and above room temperature. Achieving this goal requires a breakthrough in our understanding of this unique class of materials.

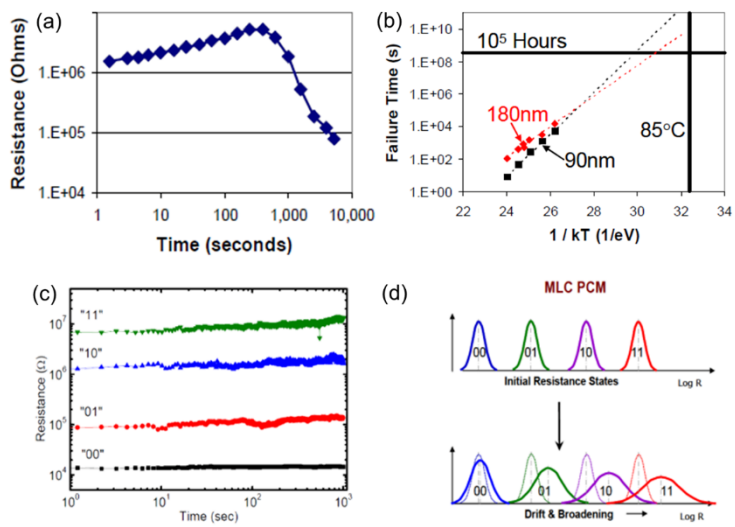

Figure 1.2 (a) Resistance curve of the RESET state of a PcRAM cell as a function of time at isothermal annealing at 180 ℃, which describes data retention loss induced by crystallization. (b) Arrhenius fitting of the failure time as a function of $1/kT$ to extract the failure time at a relatively low temperature of 85 ℃. This Arrhenius fitting allows the failure time of the PcRAM cell to be predicted.[7] (c) Time-dependent resistance of the RESET state of a PcRAM cell at room temperature ($T < T_g$).[8] (d) Impact of the resistance drift on the multi-level cell (MLC) PcRAM.[9]

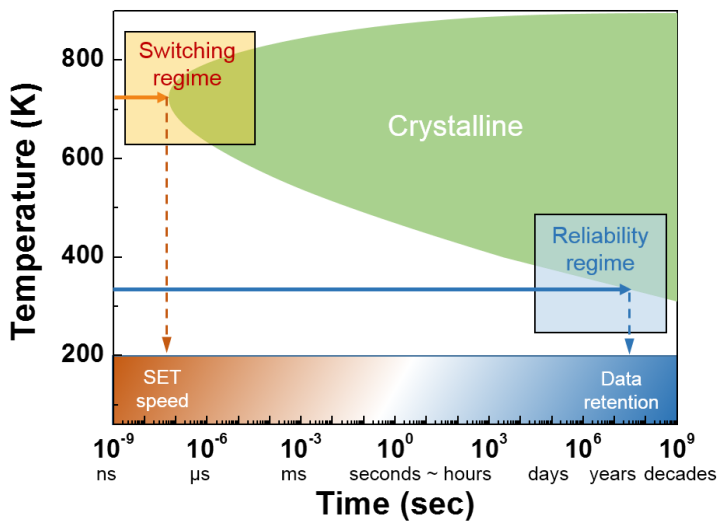

Figure 1.3 Time-Temperature-Transformation (TTT) diagram showing the relationship between the crystallization kinetics and PcRAM characteristics. Switching regime: the crystallization time at high temperatures is the SET speed. Reliability regime: the crystallization time at low temperatures is the data retention time.

Second, **Figure 1.2(c)** shows the resistance drift, which is a steady increase in the resistance of the amorphous state of phase-change materials.[10-13] The development of PcRAM technology into multi-level cell (MLC) storage devices, which have more than two intermediate resistance levels,[14] results in the overlap of resistance between phases[14] and leads to reliability issues in PcRAM as depicted in **Figure 1.2(d)**. The microscopic origin of resistance drift has been explained using several models, including the defect annihilation model and the strained bandgap model.[10, 11, 15] The metastable nature of amorphous materials results in time-dependent properties due to their self-stabilization process, which is called structural relaxation[16] and will be covered in detail in **Sec. 2.1.2** and **Sec. 2.1.5**.

Verification of the origin of the resistance drift is important in improving the reliability of PcRAM. As depicted in **Figure 1.4**, the defect annihilation model claims that resistance drift originates from defect annihilation in amorphous GST; i.e., an intrinsic origin. Conversely, the strained bandgap model claims that resistance drift originates from residual stress relaxation in amorphous GST; i.e., an extrinsic origin. As a result, the solution for minimizing the resistance drift should be based on the appropriate model: the development of amorphous materials that resist defect annihilation or an optimized design for the minimization of the residual stress.

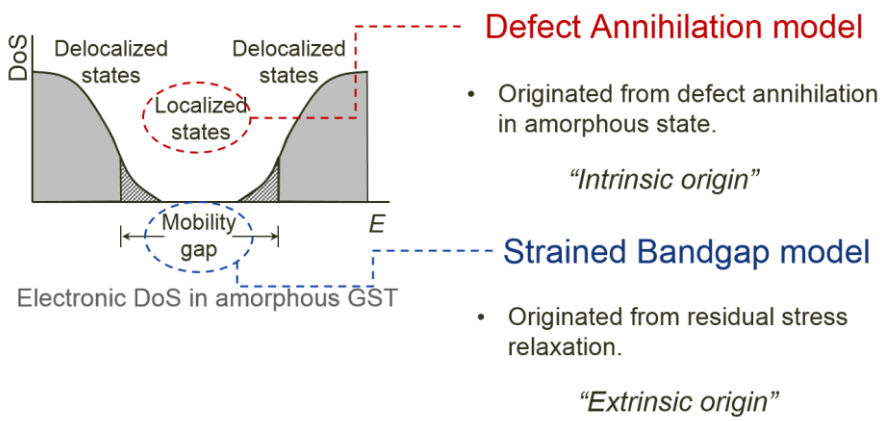

Figure 1.4 Description of the electronic density of state for an amorphous GST and the features relevant to resistance drift models: the defect annihilation model and the strained bandgap model.

1.3. Practical issues in amorphous oxide semiconductor TFTs

Amorphous oxide semiconductors have been actively pursued as an alternative for amorphous silicon (a-Si) in thin-film transistors (TFTs) due to their transparency, flexibility,[17] large area uniformity and low process temperature, which make them highly applicable to numerous future applications because they can be utilized as an as-deposited amorphous phase without subsequent crystallization.

Most popular approach is amorphous In-Ga-Zn-O (a-IGZO), which exhibits a high carrier mobility (5 - 50 $cm^2/V{\cdot}s$).[18] As a result, IGZO TFTs are expected to significantly improve the operation speed, resolution and size of flat panel displays. In addition, a-IGZO TFTs are expected to be ideal for organic light-emitting diodes (OLEDs). **Figure 1.5(a)** shows an a-IGZO TFT on a flexible substrate.

However, a-IGZO exhibits unstable characteristics as a TFT; the mobility and threshold voltage drift during thermal annealing, illumination and bias stress[19-22] cause long-term device reliability issues. Recently, thermally induced changes in the bandgap, such as those shown in **Figures 1.5(b)** and **(c),** have been reported along with the film density of a-IGZO[23]; these changes may be responsible for the unstable TFT characteristics. Structural relaxation, including changes in the structural properties of a-IGZO (e.g., network reconfiguration), occur at much lower temperatures than T_x.[23] The stability of a-IGZO films is significantly lowered by the surface effect; the drift in a-IGZO TFT characteristics likely originates from the structural instability of the surface layer rather than bulk instability. Therefore, developing stable amorphous materials based on an understanding of the characteristics of a-IGZO is required to design reliable and high-performance TFT devices.

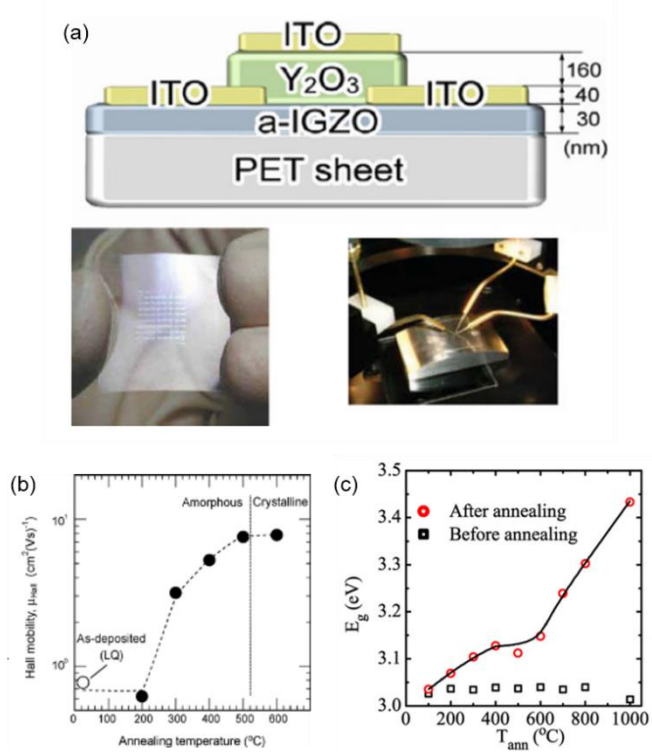

Figure 1.5 (a) Schematic of a top-gate flexible transparent TFT using an a-IGZO film as an active layer fabricated on a PET substrate.[17, 18] (b) The structural instability of a-IGZO leads to drift of the TFT characteristics (e.g., mobility, V_{th})[22] (c) Band gap energy (E_g) as a function of annealing temperature.[23]

1.4. Objective of the thesis

The application of amorphous materials to devices has practical issues that are mainly the result of their inherently metastable nature. Because amorphous material is not in equilibrium and is metastable compared to its counterpart, crystalline material, it suffers from unintended property changes (e.g., electrical properties) associated with temperature-dependent and time-dependent phase and structural changes. Therefore, it is important to characterize the phase and structural changes in amorphous semiconductors to develop high performance and highly stable amorphous-based electronic devices.

However, the methods used to detect structural changes in amorphous materials are limited due to their random structure and the slight signal changes associated with structural changes. We propose using mechanical stress analysis to investigate the volumetric and viscosity changes in amorphous thin films by utilizing the substrate curvature measurement system with a multi-beam optical sensor.[24]

The objective of this thesis is to investigate the crystallization temperature (T_x), glass transition temperature (T_g), super-cooled liquid region (T_x - T_g), viscosity and fragility of amorphous GST films, which are relevant to PcRAM characteristics, using mechanical stress. Interstitial (C, N) and substitutional doping (Bi, Al) are used to change the bond networks. The relationship between the bond networks of phase change materials and the resulting material properties are established. The results provide a guideline for obtaining high performance and reliability in PcRAM.

The second objective is to identify the time-dependent drift of resistance in amorphous phase change materials that leads to instabilities in PcRAM. To determine the origin of the resistance drift, mechanical stress relaxation and electrical resistance

measurements are conducted on amorphous GST thin films under the same sample conditions.

The origin of resistance drift according to the proposed models can be verified by the quantitative analysis of mechanical stress relaxation and electrical resistance drift measurements in thin film structures.

The final objective is to examine the inherently structural instability of a-IGZO films that are relevant to the characteristics of TFT devices. The glass transition and fragility of a-IGZO film are investigated using mechanical stress analysis. From the dependence of these behaviors on film thickness, we determine that the structural instability near the glass transition temperature originates from the surface layer. At temperatures below the glass transition temperature, we find that the structural relaxation of glass is attributed to viscous flow that relieves the residual stress and densification. Our study offers a physical understanding of the mechanisms that govern the structural instability of amorphous materials.

A thorough analysis of the experimental data in conjunction with theoretical models will help build a framework to describe and explain the unconventional properties of amorphous semiconductors that are used in PcRAM as well as a-IGZO TFT devices.

1.5. Organization of the thesis

This thesis consists of eight chapters. In Chapter 2, the principles of amorphous materials are reviewed, and the basic theory and characteristic features of phase change materials and amorphous oxide semiconductors are explained in detail. The basic theory of mechanical stress in thin films is also discussed in Chapter 2. Chapter 3 describes the

experimental procedure, including the fabrication of the samples and the mechanical stress analysis using the substrate curvature measurement system. In Chapter 4, the effects of doping on the glass transition and crystallization of amorphous $Ge_2Sb_2Te_5$ and PcRAM characteristics is presented. Chapter 5 discusses the effects of doping on the strain energy in crystalline $Ge_2Sb_2Te_5$. Chapter 6 describes the structural relaxation of amorphous $Ge_2Sb_2Te_5$ and the resistance drift in PcRAM. Chapter 7 discusses the effects of an unstable surface on the glass transition of amorphous In-Ga-Zn-O for thin film transistors. Chapter 8 summarizes the results of this study.

CHAPTER 2

Theoretical background

2.1. Principles of amorphous materials

2.1.1. Atomic structure

Figure 2.1 shows schematic diagrams of amorphous and crystalline atomic structures. The crystalline structure has a regular atomic arrangement in a 3-d periodic array. The crystal structure exhibits regularity over long distances along the crystal lattice, which is called long-range order. In contrast, the amorphous structure is disordered and randomly distributed.[1, 25] This means that there is no periodicity; however, it is not completely irregular. Rather, it has an atomic structure over a regular atomic-scale called the short-range order. The unique atomic configurations of amorphous materials lead to characteristic material properties (e.g., high mechanical strength, large elastic strain limit, low carrier mobility and uniform properties over large areas). Therefore, amorphous materials have actively been applied to machinery and sporting goods as well as multi-functional and process-friendly electronic devices.

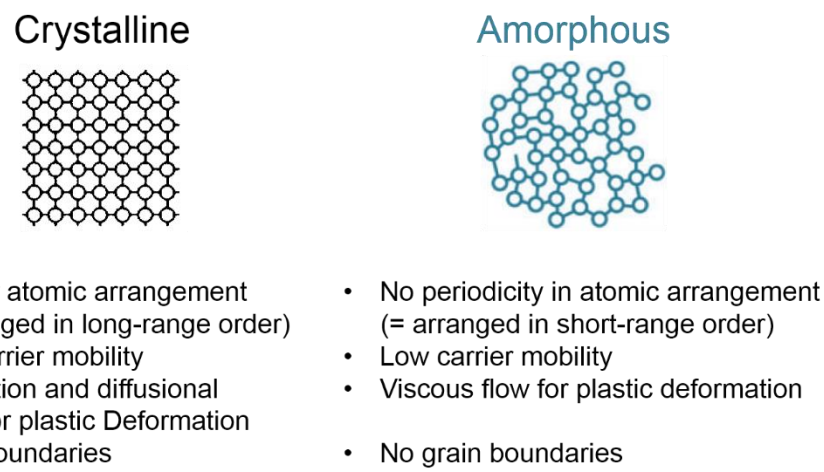

Figure 2.1 Schematic diagrams of amorphous and crystalline atomic structures. The crystalline structure has a regular atomic arrangement in a 3-dimensional periodic array, while the amorphous structure is a nearly random disordered structure.

Most solid materials have a periodicity in their atomic structure; i.e., the atoms are arranged periodically in the crystal lattice. In contrast, liquid materials have a disordered atomic arrangement with a high degree of freedom in their atomic movements. When a liquid is cooled below its melting point, the liquid material solidifies into a disordered atomic arrangement with regularly arranged atoms. However, if the liquid solidifies by quenching at a high cooling rate, the atoms in the liquid material do not have enough time to arrange into a periodic structure; as a result, solid materials with disordered atomic structures similar to the liquid materials form, which are referred to as amorphous materials.

2.1.2. Structural changes

Figure 2.2(a) shows a schematic of volumetric changes (or energy in a broad sense) as a function of temperature. Generally, when a liquid with a highly disordered atomic structure is cooled to the melting point (T_m), the liquid solidifies into a crystalline material with an ordered structure following the arrow in **Figure 2.2(b)**. If the crystalline solid is heated again to an elevated temperature, the solid follows a similar path as when it was cooled.

However, as the cooling rate is increased, the liquid does not crystallize immediately and cools below the melting point while maintaining its liquid-like characteristics as depicted in **Figure 2.2(c)**. This state is referred to as super-cooled liquid. When the temperature is decreased, the degree of super-cooling increases, and the driving force of nucleation is greatly increased. However, nucleation will be hindered by the reduced atomic mobility due to the low temperature. As a result, when the cooling is fast enough, atomic movement is not sufficient to cause nucleation. A solid material with a disordered

structure (like frozen liquid) would form as the glass transition temperature is reached; this material is referred to as glass.

When the glass is heated again to an elevated temperature, the glass will undergo structural changes in several steps.[26] **Figure 2.2(d)** shows the volumetric changes as a function of temperature; the arrows indicate the path of volumetric changes associated with the structural changes in amorphous materials that are associated with heating. It should be noted that the material properties shown below are only applicable to the heating of glass and are not applicable to cooling from a super-cooled liquid.

The *glass transition* refers to the phenomenon in which the solid-like glass changes to a liquid-like super-cooled liquid above a certain temperature (the glass transition temperature, T_g). As depicted in **Figure 2.2(d)**, the glass transition is accompanied by a gradual volume expansion with heating due to the difference in thermal expansion between the glass and the super-cooled liquid. Because the glass transition accompanies the softening of the glass, it provides sufficient atomic mobility for crystallization to occur. Therefore, crystallization below T_g is extremely slow due to the high energy barrier for atomic rearrangement, and T_g can be regarded as the minimum limit of T_x.

Crystallization refers to the phenomenon in which an irregular atomic structure of the amorphous state changes to a regular atomic structure of a crystalline state above a certain temperature (the crystallization temperature, T_x). The high atomic mobility of the super-cooled liquid allows crystallization before reaching T_m. As depicted in **Figure 2.2(d)**, crystallization is accompanied by abrupt volume shrinkage[27] due to the difference in density between the amorphous and crystalline material.

The *super-cooled liquid region* refers to the temperature range between T_x and T_g and is therefore determined by T_x - T_g. If this value is large, super-cooled liquid is likely present in a wide temperature range and suppresses crystallization at elevated

temperatures. Because T_x - T_g is the temperature interval in which the temperature increases before crystallization, this parameter can be regarded as a quantitative measure of the thermal stability of the amorphous material.

Structural relaxation refers to the time-dependent self-stabilization process of glass below T_g. Structural relaxation accompanies structural changes due to the local rearrangement of atoms to reach a more stable state due to metastability, as indicated by the downward-pointing arrows in the direction of volume shrinkage or decreasing energy in **Figure 2.2(d).** An as-prepared glass is thermodynamically unstable compared to its equilibrium state (the liquid state for the same temperature as indicated by the dashed line below T_g). Its free energy could be lowered by structural changes toward the metastable equilibrium configuration, which is called structural relaxation. This phenomenon would be manifested by continuous changes in all of the physical properties, including volume and mechanical stress, with time.

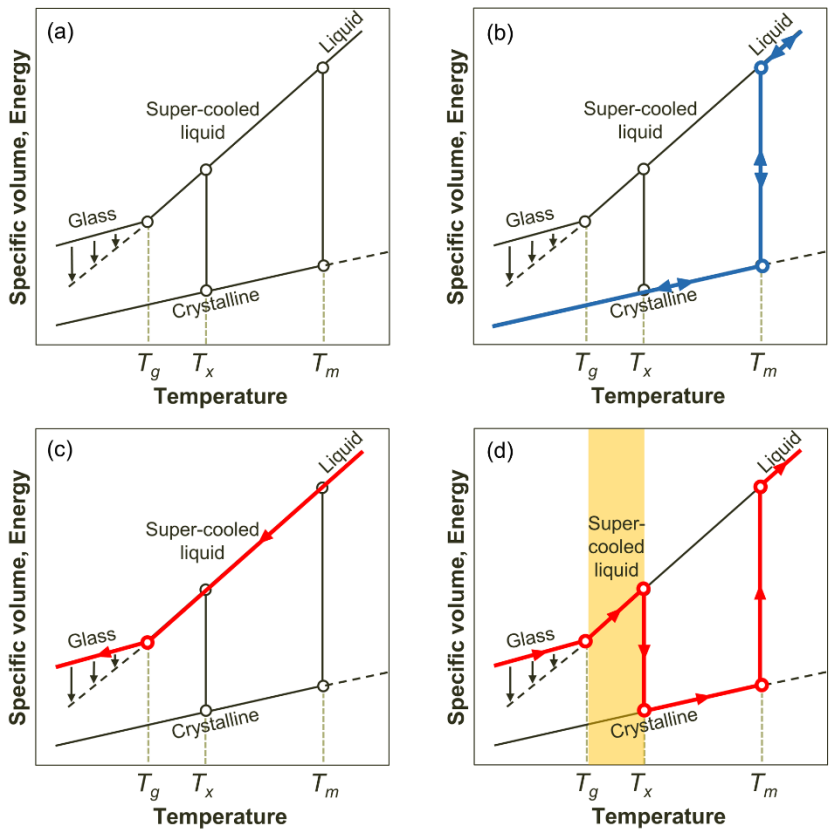

Figure 2.2 (a) Schematic of the volumetric changes (or energy) of materials as a function of temperature. (b) The formation of a crystalline solid when the liquid is cooled at a relatively low cooling rate. (c) The formation of glass when the liquid is cooled at relatively high cooling rate. (d) The volumetric change of glass associated with structural relaxation, the glass transition, crystallization and melting.

2.1.3. Viscosity

Viscosity is a quantitative measure of the resistance to flow in liquids. Various behaviors that accompany flows in amorphous materials, including glass and super-cooled liquid, can also be described using the concept of viscosity because of the liquid-like structure of amorphous materials. Viscosity has an enormous significance in the description of amorphous materials for the following reasons. First, it can describe the thermodynamic and kinetic behaviors of amorphous materials (e.g., glass transition, crystallization and structural relaxation, all of which are accompanied by atomic arrangements) as was discussed in **Sec. 2.1.2**. Second, it can also describe the plastic deformations that are relevant to amorphous materials. In this section, the viscosity changes associated with the thermodynamic and kinetic behaviors of amorphous materials are discussed. The viscosity changes associated with plastic deformation will be discussed in the theoretical background of mechanical stress in **Sec. 2.3.4**.

The theory of the flow defect model has facilitated a microscopic description of viscosity that is relevant to flows in amorphous materials.[28, 29] In this model, a flow defect is regarded as the center at which the flow of the atom occurs. In the case of an amorphous material with covalent bond networks, the flow defect can be regarded as an unoccupied bond, which is also referred to as a dangling bond. In the case of amorphous materials with ionic or metallic bond networks, a flow defect can be regarded as a free volume. Theoretically, the free volume of an amorphous material is defined as the region that is not occupied by spherical atoms in the case of metallic or ionic materials. **Figure 2.3** shows a schematic of individual atomic flows, which are the basic component of macroscopic flows and consequently determine the viscosity. When no external force is applied to the system, the chances of jumping across the energy barrier ΔG^m will be

equal in both directions. However, when an external force (τ) is applied to the system, the chances of jumping in the forward direction are greater due to the decrease in the energy barrier by as much as $\Delta G/2$. The parameter τ can be regarded as 1) the driving force for the reaction in the manner of the kinetic behaviors (e.g., the glass transition, crystallization and structural relaxation) and 2) the mechanical stress that causes deformation in the manner of the mechanical behavior.

The viscosity of amorphous materials changes with structural changes (e.g., structural relaxation, the glass transition, crystallization and melting) that occur with heating. **Figure 2.4** shows the logarithm of viscosity as a function of temperature, and the arrows indicate the path of the viscosity change associated with the heating. Below T_g, the glass experiences a moderate decrease in viscosity with increasing temperature. Generally, the glass transition temperature T_g is defined when the viscosity reaches 10^{12} Pa-s. When the temperature is increased above T_g, the super-cooled liquid experiences a rapid drop in viscosity, which provides sufficient atomic mobility for crystallization to occur.

Because crystallization is defined as the phenomenon in which the amorphous state changes to the crystalline state with fewer flow defects, crystallization is accompanied by an abrupt increase in viscosity due to the denser (less flow defects) crystalline structure as shown in **Figure 2.4.**

Structural relaxation accompanies the structural changes due to the local rearrangement of atoms to reach equilibrium as indicated by the upward-pointing arrows in the direction of increased viscosity in **Figure 2.4**. Therefore, this phenomenon is manifested by time-dependent viscosity changes. The relevant model will be covered in detail in **Sec. 2.1.6**.

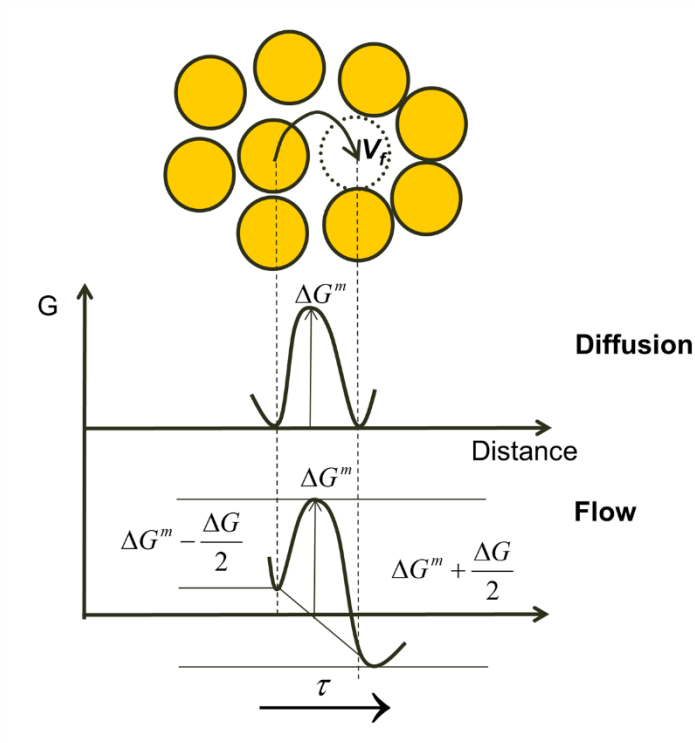

Figure 2.3 Illustration of an individual atomic flow in an amorphous material based on the concept of free volume.[28]

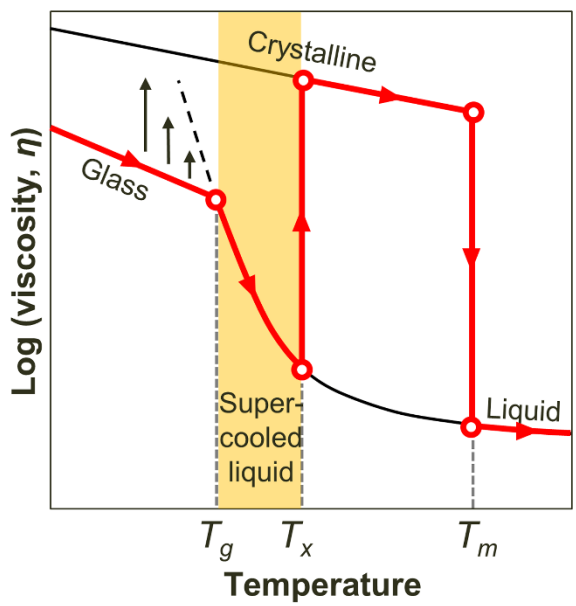

Figure 2.4 Schematic of the transformation of a liquid to an amorphous material by rapid cooling. A solid material with a disordered structure (like frozen liquid) will form as the glass transition temperature is reached and is referred to as glass.

2.1.4. Fragility in super-cooled liquid

One of the important properties of a super-cooled liquid is the temperature dependence of viscosity, which is crucial for determination of the crystallization rate at the core of the crystallization. Moreover, the temperature dependence of viscosity has an important role in determining the structural stability.

The well-known "Angell plot"[30, 31] for the logarithm of the viscosity (or the relaxation time) as a function of T_g/T in a super-cooled liquid is introduced in **Figure 2.5** and clearly illustrates the temperature dependence of viscosity. Angell suggested the use of the reciprocal of the temperature normalized to T_g for a direct comparison of different materials with different networks and bondings (i.e., usually corresponds to different T_g.).

In some super-cooled liquids, *Arrhenius behavior* is observed; the logarithm of the viscosity is assumed to be linearly related to the reciprocal of the temperature:

$$\eta = \eta_0 \exp\left(\frac{E}{kT}\right) \tag{2.1}$$

Accordingly, the activation energy of viscosity (E) is independent of the temperature, k is the Boltzmann constant, and η_0 is a constant. To describe temperature-dependent viscosity and the relevant behaviors (e.g., the glass transition and crystallization), we only have to measure E, which is a manageable task. Arrhenius behavior is generally found in materials with a covalent bond (e.g., Si, SiO_2 and other materials with tetrahedral networks). These substances are referred to as *strong* liquids and are characterized by small differences of amorphous and crystalline structure.

However, deviations from Arrhenius behavior can occur depending on the material.[30, 32-34] This non-Arrhenius behavior is described as *Vogel-Fulcher-Tammann behavior*, which is expressed as follows:[35]

$$\eta = \eta_0 \exp\left(\frac{DT_0}{T - T_0}\right) \tag{2.2}$$

where D and T_0 are fitting parameters. This Vogel-Fulcher-Tammann equation generally best fits the experimental data of super-cooled liquids with non-Arrhenius behavior. As shown in **Figure 2.5**, the temperature dependence of the viscosity at low temperatures and high temperatures is not associated with a strong relationship such as the Arrhenius relationship. For this reason, direct measurement of the viscosity at a high temperature is required to describe the temperature dependence of viscosity and the relevant behaviors. Polymers consisting of Van der Waals bonds or ionic bonds show Vogel-Fulcher-Tammann behavior. These substances are referred to as *fragile* liquids and are characterized by relatively large free volumes in their structures. Surprisingly, chalcogenides with covalent bond networks also have fragile behaviors.[36] The temperature dependence of viscosity is important because it can also be utilized to describe the crystallization behavior of certain materials. Because the viscosity is strongly related to the crystal-growth velocity, fragile behavior enables faster crystallization at high temperatures than strong behavior.

Fragility has been introduced to quantify the deviation from Arrhenius behavior of the viscosity to temperature in various materials.[30] The fragility is quantified by measuring the slope of the logarithm of the viscosity as a function of T_g/T at $T = T_g$. The fragility (m), can be obtained by using the equation:

$$m = \left.\frac{d\log\eta(T)}{d(T_g/T)}\right|_{T=T_g} = \left.\frac{d\log\tau(T)}{d(T_g/T)}\right|_{T=T_g} \tag{2.3}$$

If m has a value of approximately 16, the amorphous material is classified as a strong glass with the Arrhenius model; on the other hand, a much larger value of m (e.g., $m \sim 90$) is classified as a fragile liquid with the non-Arrhenius model. The fragility can be regarded as a universal criterion of the kinetic stability in various amorphous materials.

For the experimental characterization of the fragility, Arrhenius behavior is assumed only at $T = T_g$. Because non-Arrhenius relaxation causes the activation energy of relaxation to vary with temperature, the apparent activation energy for relaxation (E) is provided at T_g as follows:

$$\tau = \tau_0 \exp\left(\frac{E}{kT}\right) \tag{2.4}$$

where τ_0 is a constant. The apparent activation energy of relaxation (E) is defined only at $T = T_g$. Combining **Eq. (2.3)** and **Eq. (2.4)** gives a simpler form of the fragility as a function of E for relaxation:[33, 37]

$$m = \frac{E}{\ln 10 RT_g} \tag{2.5}$$

E can be extracted from the kinetic nature of the glass transition using the Moynihan

plot.[38] T_g is generally observed to shift towards higher temperatures as the heating rate increases, and this characteristic shift of T_g is used to determine E. The derivation of the Moynihan plot is described below.[38] When a sample is heated at a heating rate of β, the time (Δt) for the temperature change (ΔT) can be described. This equation means that a higher β leads to a lower Δt.

$$\Delta t = \frac{\Delta T}{\beta} \tag{2.6}$$

The relaxation time (τ) can be defined as the time required to reach a certain energy state and is given by following equation:

$$\left(\frac{dH}{dt}\right) \cdot \tau = \Delta H \tag{2.7}$$

As was explored in **Eq. (2.4)**, τ is a function of temperature and decreases with increasing temperature.

The relaxation times and time durations for the temperature changes at three different states are listed here, The glass state ($T < T_g$) shows $\Delta t \ll \tau$ because relaxation is unlikely to occur in this state. In contrast, the super-cooled liquid state ($T > T_g$) shows $\Delta t \gg \tau$ because relaxation occurs easily in this state. As a result, the glass transition temperature ($T = T_g$) shows $\Delta t \sim \tau$, at which liquid-like behavior begins. As was described above, Δt decreases for higher values of β. Therefore, for the glass transition, a greater ΔT is required to lower τ, which enables the condition $\Delta t \sim \tau$. For $\Delta t \sim \tau$ at $T = T_g$, combining **Eq. (2.4)** and **Eq. (2.6)** gives following equation:

$$\frac{\Delta T}{\beta} = \tau_0 \exp\left(\frac{E}{RT}\right)\Bigg|_{T=Tg} \tag{2.8}$$

Taking the natural logarithm of both sides of **Eq. (2.8)** gives:[38]

$$\ln \beta = -\frac{E}{RT_g} + C \tag{2.9}$$

where β is the heating rate in K/min, and C is a constant. The value of E obtained using this relation can be utilized to extract the fragility m[39-43] using **Eq. (2.5)**.

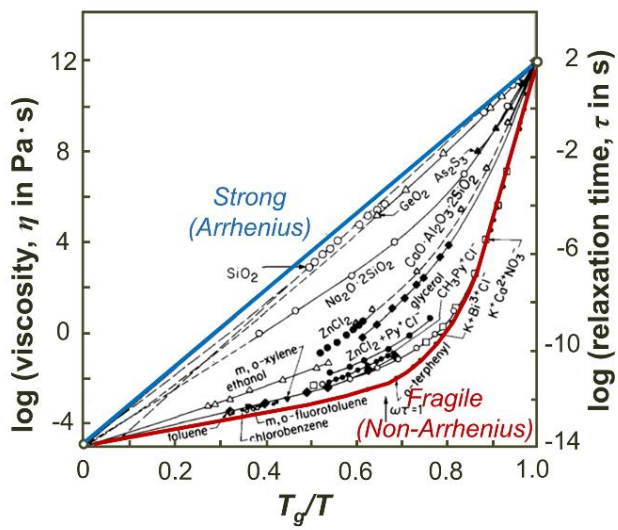

Figure 2.5 The Angell plot[30] shows the temperature dependence of viscosity (or relaxation time) in the super-cooled liquid. Fragility is quantified by measuring the slope of the logarithm of the viscosity as a function of T_g/T at $T = T_g$.

2.1.5. Structural relaxation in glass

As was addressed in **Sec. 2.1.2.**, glass is thermodynamically unstable and decreases its free energy by structural changes toward its equilibrium state. This time-dependent self-stabilization process of glass below T_g is structural relaxation. Structural relaxation is accompanied by continuous changes of material properties, most importantly viscosity. At low temperatures far below T_g, the viscosity of glass is observed to increase with time; this time-dependent viscosity is induced by structural relaxation as indicated by the upward-pointing arrows in **Figure 2.4**.

The viscosity of glass is expressed as the reciprocal of the concentration of flow defects as follows:[16, 44]

$$\eta = \frac{kT}{n_f k_r (\gamma_0 \upsilon_0)^2} \tag{2.10}$$

where n_f is the concentration of flow defects, k_r is the jump frequency of flow defects, γ_0 is the shear strain per jump of a flow defect, and υ_0 is the volume of a flow defect. The analytical solution can also be obtained from **Eq. (2.10)**:

$$n_f(t) \cdot \eta(t) = n_{f,0} \cdot \eta_0 \tag{2.11}$$

where η_0 is the initial viscosity at the beginning of structural relaxation ($t = 0$), and $n_{f,0}$ is the initial concentration of flow defects at the beginning of structural relaxation ($t = 0$). The time-dependent viscosity change induced by structural relaxation is described by the annihilation (or creation) of flow defects:

$$\frac{d\eta}{dt} \propto -\frac{1}{n_f^2}\frac{dn_f}{dt} \tag{2.12a}$$

$$\frac{d\eta}{dt} \propto -\frac{1}{n_f}\frac{dn_f}{dt} \tag{2.12b}$$

Eq. (2.12a) is called bimolecular defect annihilation and describes defect annihilation by the interaction of two flow defects. **Eq. (2.12b)** is called unimolecular defect annihilation and describes annihilation of only one flow defect. For covalently bonded glass, annihilation of a flow defect occurs when two unoccupied bonds come together to form one covalent bond. Therefore, the use of the bimolecular annihilation model is no surprise. The model is less obvious in metallic or ionic glass compared to the case of covalently bonded amorphous materials.

$$\frac{dn_f}{dt} = -k_r n_f^2 \tag{2.13a}$$

$$\frac{dn_f}{dt} = -k_r n_f \tag{2.13b}$$

Combining **Eq. (2.12a)** and **Eq. (2.13a)** gives the time-independent $d\eta/dt$, which is proportional to k_r. As a result of integration, a linear increase in viscosity with time is obtained at temperatures far below T_g:

$$\eta(t) = \eta_0 + kt \tag{2.14a}$$

where k is time-independent $d\eta/dt$. By combining **Eq. (2.12b)** and **Eq. (2.13b)**, the exponential increase in viscosity with time is obtained at temperatures far below T_g:

$$\eta(t) = \eta_0 \exp(k_r t) \tag{2.14b}$$

However, it should be noted that as equilibrium is approached, the linear dependency of viscosity with time disappears, and the rate of viscosity change is saturated near T_g.

2.2. Principles of amorphous semiconductors

2.2.1. Phase change materials

The *bond characteristics* of the amorphous and crystalline states determine the characteristic behavior of a phase change material.[45] Covalent bonding is employed in amorphous phase change materials; however, crystalline phase change materials utilize resonance bonding, which is a special variant of covalent bonding. In a resonance bonding system, the resulting electronic structure is obtained by the superposition of all possible configurations.[45] This type of bonding is common in organic molecules (e.g., benzene) but is rare in inorganic solids.

Figure 2.6 shows the mapping of the physical properties of phase change materials for various material compositions.[2] Two coordinates are used: *s-p* hybridization (i.e., "covalency", which is determined by the split between the valence s- and p-states) on the y-axis and ionicity on the x-axis. Phase change materials are located in a small region that is characterized by low ionicity and low *s-p* hybridization.

The *crystallization kinetics* of a phase change material are one of the most crucial theories regarding the application of PcRAM because the operating principle of PcRAM is determined by its crystallization kinetics. The crystallization rates as well as the relevant material properties (e.g., viscosity, relaxation time) of phase change materials do not follow the Arrhenius relationship with respect to temperature as depicted in **Figure 2.7**. If the crystallization of phase change materials can be described by Arrhenius behavior, we only have to understand the relationship between stoichiometry and the relevant activation barrier, which is a manageable task. However, at the core of the crystallization kinetics of phase change materials is the unusual temperature

dependence of the crystal growth velocity. In **Figure 2.7**, both Si and SiO_2 can be described well by an Arrhenius law. In contrast, the phase change material $Ge_2Sb_2Te_5$ shows pronounced deviations from an Arrhenius behavior. This is attributed to the so-called fragile behavior, which describes a pronounced non-Arrhenius behavior (Vogel-Fulcher-Tammann relation).[36, 46, 47]

Doping in phase change materials can be utilized to control the bond characteristics that are relevant to the crystallization kinetics. As mentioned in **Sec. 2.1.4.**, bond networks control the temperature dependence of the viscosity, which is relevant to the crystallization behavior. To facilitate this concept, the bond networks in amorphous GST were modified by inserting various dopants. Generally, several substances are utilized as dopants, including N[48-50], C[51, 52], Bi[53, 54] and other metals (Al[55, 56], Ag[57-59], Cu[56] and etc.), to attain high performance and high reliability of PcRAM. Each dopant has its own effect on the structural properties of GST; elements with relatively small atomic radii, such as C and N, will be located in the free volume (interstitial dopants), while elements with relatively large atomic radii, such as Al and Bi, will more likely be located in the substitutional positions (substitutional dopants) of Ge, Sb or Te. The bonding enthalpies of the amorphous GST will also be significantly altered by the features of the dopants, such as the electronegativity or local atomic arrangement. C, N and Al increase the total bonding enthalpy, while Bi decreases the total bonding enthalpy. The structural effects of the dopants are listed in **Table 2.1**.

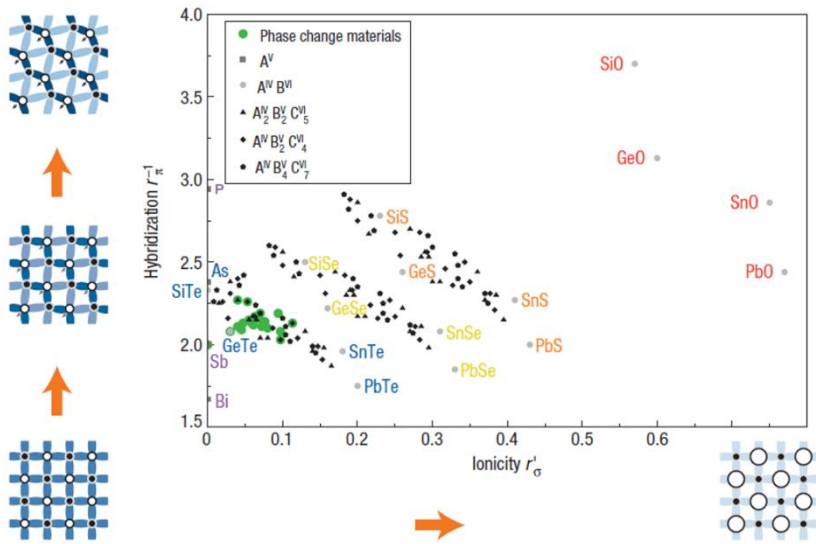

Figure 2.6 Mapping of physical properties of phase change materials with various compositions. Two coordinates are used: *s-p* hybridization (i.e., "covalency", which is determined by the split between the valence s- and p-states) on the y-axis and ionicity on the x-axis.[2]

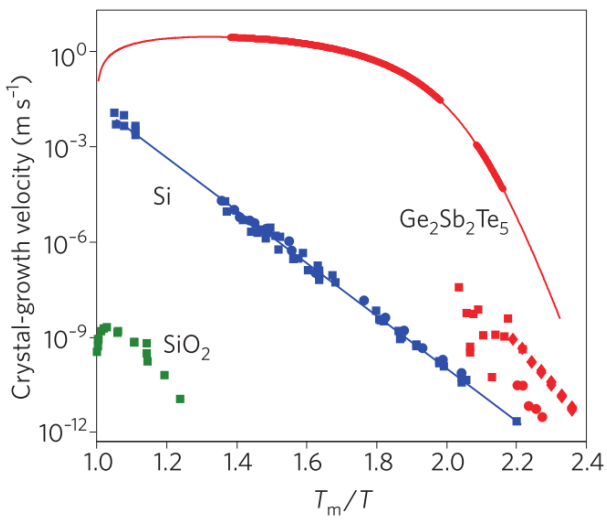

Figure 2.7 Crystal-growth rates of Si, SiO_2 and $Ge_2Sb_2Te_5$ as a function of temperature.[47] While Si and SiO_2 show classic Arrhenius behaviors (strong glasses), $Ge_2Sb_2Te_5$ displays a very different fragile behavior.

Table 2.1 Comparison of the structural features of the dopants that are relevant to $Ge_2Sb_2Te_5$.

	C doping	N doping	Al doping	Bi doping
Structural effect	Interstitial (Free volume occupation)		Substitutional (Atomic position)	
Preferred bonds	C-Ge, C-Te, C-C	Ge-N	Al-Sb, Al-Te	Bi-Te

2.2.2. Amorphous oxide semiconductors

The *bond characteristics* of amorphous oxide semiconductors (e.g., a-IGZO) exhibit an unconventional shape compared to the bonding characteristics of a-Si. The bonding of oxide semiconductors is characterized by an ionic bond. The high carrier mobility (5 - 50 $cm^2/V{\cdot}s$) of a-IGZO compared to a-Si originates from the structural features of the ionic bonding characteristics that are distinct from the covalent bonding.

Figure 2.8 shows a schematic image of orbital drawings that determine the carrier transport in crystalline and amorphous semiconductors for covalent systems and ionic systems. For the conventional case of covalent semiconductors (e.g., a-Si or crystalline Si), carrier transport occurs via sp^3 orbitals, which are strongly sensitive to the bond angle of the atomic network. Therefore, the disordered structure of the amorphous state restricts carrier transport as depicted in **Figure 2.8(a)**.

For the ionic semiconductors, spheres indicate the metal *s* orbitals. The neighboring metal *s* orbitals overlap, as shown in **Figure 2.8(b)**; as a result, the carrier transport is insensitive to the bond angles, and the disordered structure of the amorphous state of the ionic semiconductors maintains the high carrier mobility.

The *structural stability* of amorphous oxide semiconductors is highly sensitive to its composition; as shown in **Figure 2.9(a)**, ZnO and In_2O_3 are highly unstable amorphous states because the crystalline state forms when it is deposited at room temperature. Conversely, in multi-component oxide semiconductors with different ionic sizes and charges, the structural stability of an amorphous state is improved.[60] In ionic or metallic glass systems, multiple components (more than 3 elements) generally lead to increasing resistance to crystallization by forming a randomly packed structure with a high packing density,[61] as described in **Figure 2.9(b)**.[62]

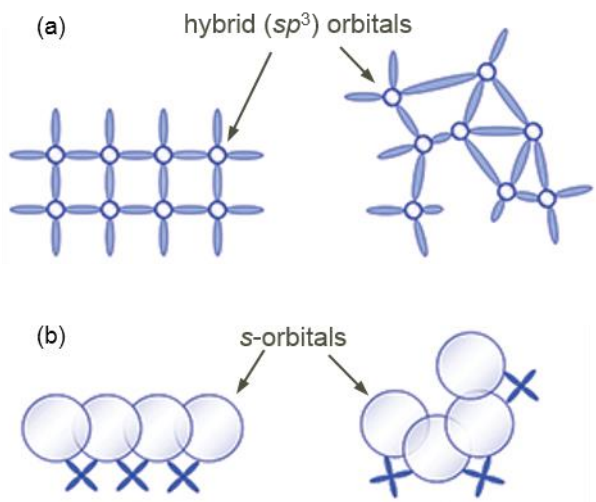

Figure 2.8 Schematic image of orbital drawings that determine the carrier transport in crystalline and amorphous semiconductors for (a) covalent bonding systems and (b) ionic bonding systems. For the conventional case of covalent semiconductors (e.g., a-Si or crystalline Si), carrier transport occurs via sp^3 orbitals, which are strongly sensitive to the bond angle of the atomic network.[63]

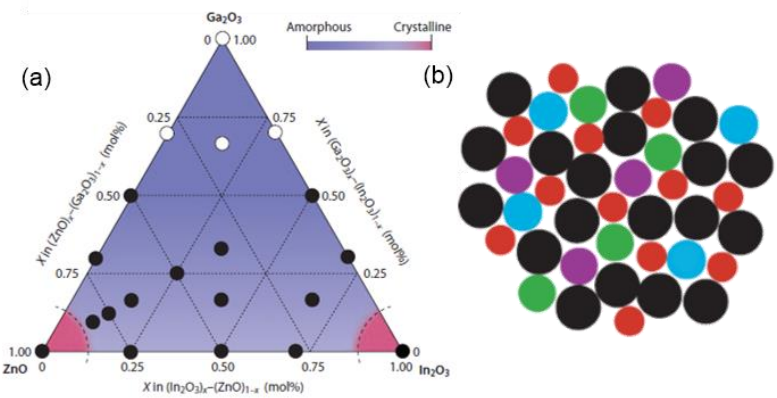

Figure 2.9 (a) Tendency of amorphous formation (phase stability of the amorphous state) of In_2O_3-Ga_2O_3-ZnO thin films for various stoichiometries. Measured data are denoted by closed circles, and unmeasured data are denoted by open circles.[60] (b) High phase stability of amorphous In-Ga-Zn-O due to the large size and charge mismatch between the ions, which leads to high stability.[62]

The *surface effect*, however, can degrade the inherently high stability of a-IGZO as an amorphous state. Especially when a-IGZO is utilized as a thin film structure in electronic applications, the high surface-to-volume ratio of the film can lead to surface-originated instability. The surface instability of thin films is a serious issue and has been reported by other researchers; unconstrained bonds on the surface are reported to be associated with a high mobility of atoms.[64]

As depicted in **Figure 2.10(a)**, the atoms in the bulk region are constrained by neighboring atoms, and their local environment is highly restricted. Instead, atoms that are located on a free surface are constrained by fewer neighboring atoms than the atoms in the bulk region, which likely results in less binding energy. This structural difference between atoms in the bulk region and on the free surface leads to higher atomic mobility of atoms on the free surfaces.[64]

Surface-originated instabilities have been observed for many polymeric glasses with relatively weakly bounded atomic structures.[65-77] However, distinct coordination distributions on surfaces have also been observed for amorphous Al_2O_3 films.[78, 79] **Figure 2.10(b)** shows the changes in the coordination of amorphous Al_2O_3 thin film near the surface of the film, which is manifested by a decrease in the fractions of high-energy clusters ($X^{[5]}Al$) with a decrease in film thickness from 1.4 mm to 5 nm.[78]

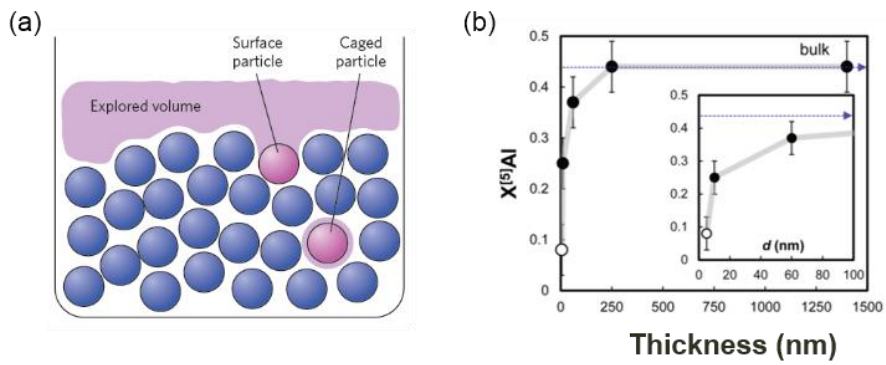

Figure 2.10 (a) Schematic description of the less-constrained bond in the surface region, which results in high atomic mobility.[64] (b) Fraction of $X^{[5]}Al$ in an amorphous Al_2O_3 thin film as a function of a decrease in the deposition thickness from 1.4 mm to 5 nm.[78]

2.3. Mechanical stress in amorphous films

In current applications in micro- and nano-electronics, the use of thin films is crucial to achieve high performance and low cost devices. However, the reliability of these devices is restricted by the mechanical stress of the thin film, which limits the lifetime. Mechanical stress in the thin film causes substrate failures as well as film debonding or cracking, which results in catastrophic failures in electronic device applications. Mechanical stress in the thin film forms because the films are constrained by a substrate. There are several origins for the stress. First, thermal stress can originate from the difference in thermal expansion coefficients between the substrate and the film. Second, epitaxial stress can originate from the mismatch of the crystalline lattice parameters between the substrate and the film. Finally, the volumetric change in a thin film associated with the phase and structural changes that were addressed in the previous section would also produce stress changes. For these reasons, characterization of mechanical stress is important not only as a measurement tool for the residual stress in the film that causes device failure but also for investigating the phase and structural changes in amorphous materials, including glass transition, crystallization, structural relaxation and viscous flow.

2.3.1. Characterization of stress in films

Thin films are defined as films that are much thinner than the thickness of the substrate on which the film is attached. To describe the mechanics of stress in a thin film on a substrate, we assume the case in which a stress-free film with a small lateral dimension (compared to the lateral dimension of the substrate) is attached to the substrate, and the film expands horizontally. When the film is not attached to the substrate, the film is

stress-free; however, the film undergoes elastic deformation that changes the dimension of the film relative to the dimension of the substrate. As a result of the elastic deformation, stress is produced in the thin film. The stress in the thin film can be expressed as a biaxial stress, and the biaxial modulus can be obtained by solving the constitutive equations according to Hooke's law. No stress occurs in the direction normal to the substrate ($\sigma_z = 0$), and an isotropic film ($\varepsilon_x = \varepsilon_y = \varepsilon$, so $\sigma_x = \sigma_y = \sigma$) is assumed:

$$\sigma = Y\varepsilon = \frac{E}{1-\nu}\varepsilon \tag{2.15}$$

where Y is the biaxial modulus of the film, and ε is the biaxial strain.

The biaxial stress in the thin film leads to bending of the substrate. **Figure 2.11** shows a schematic of the bending of the substrate induced by a change in the lateral dimension (or volume change) of the thin film. If the lateral dimension increases (volume expansion), compressive stress will be produced, and the curvature of the substrate would be negative. Conversely, if the lateral dimension decreases (volume shrinkage), tensile stress will be produced, and the curvature of the substrate will be positive. Therefore, the stress in the thin film can be measured by measuring the curvature, as will be addressed in **Sec. 2.3.2**.

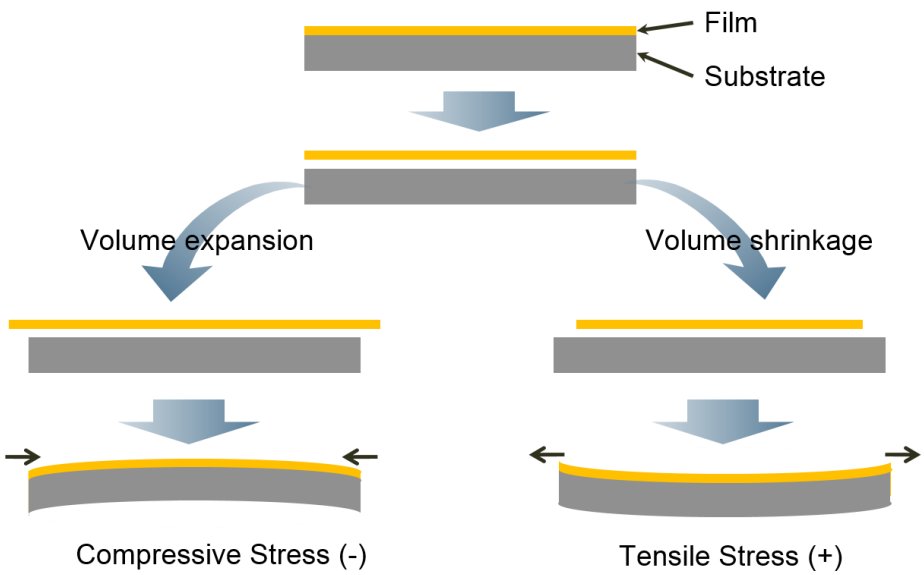

Figure 2.11 Substrate curvature due to mechanical stress in the thin film caused by volumetric changes in the thin film.

2.3.2. Substrate curvature and the Stoney equation

Mechanical stresses can arise in a thin film because the film is grown on and is therefore fixed to a substrate. As will be explained in detail below, a volume change in the film and heating of the sample, among other processes, will result in stresses because the expansion or contraction of the film is constrained by the substrate. During growth, so-called deposition stresses can be generated.

To derive the relationship between the substrate curvature and the stress in the film, biaxial bending of a thin plate is assumed as depicted in **Figure 2.12(a)**. M indicates the bending moment per unit length that will eventually cause the bending. The stress distribution in the thin plate is depicted in cross-section in **Figure 2.12(a)**. Because the thin plate is under biaxial bending conditions, the z-axis stress is zero, and the stress along the horizontal axis (film stress) is a function of *z* as shown in **Figure 2.12(a)** and as follows:

$$\sigma_{xx} = \sigma_{yy} = \alpha z, \quad \sigma_{zz} = 0 \tag{2.16}$$

When the thickness of the plate is h, the relationship between the stress along the horizontal axes and the bending moment is expressed by the following equation:

$$M = \int_{-\frac{h}{2}}^{\frac{h}{2}} \sigma_{xx} z dz = \alpha \int_{-\frac{h}{2}}^{\frac{h}{2}} z^2 dz = \alpha \frac{h^3}{12} \tag{2.17}$$

$$\sigma_{xx} = \sigma_{yy} = \frac{12M}{h^3} z \tag{2.18}$$

where the components of stress other than σ_{xx} and σ_{yy} are zero.

The relationship between the maximum bending strain (tensile) and curvature is derived here. Based on the stress distribution and the schematic in **Figure 2.12(b)**, the maximum strain is determined to be at $z = \pm h/2$. The equation is expressed as follows:

$$\varepsilon_{xx}^{Max} = \varepsilon_{xx}(z = \frac{h}{2}) = \frac{(R + \frac{h}{2})\theta - R\theta}{R\theta} = \frac{h}{2R} \tag{2.19}$$

where R is the radius of curvature of the plate. From **Eq. (2.19)**, the relationship between the maximum strain and the curvature (K) is obtained by the following equation:

$$K = \frac{1}{R} = \frac{-2\varepsilon_{xx}(z = \frac{h}{2})}{h} \tag{2.20}$$

The relationship between the strain and the bending moment is derived next. Using Hooke's law for the biaxial stress state in **Eq. (2.15)**, the strain at $z = h/2$ is transformed to the stress at $z = h/2$ as follows:

$$\varepsilon_{xx}(z = \frac{h}{2}) = \frac{1-\nu}{E}\sigma_{xx}(z = \frac{h}{2}) \tag{2.21}$$

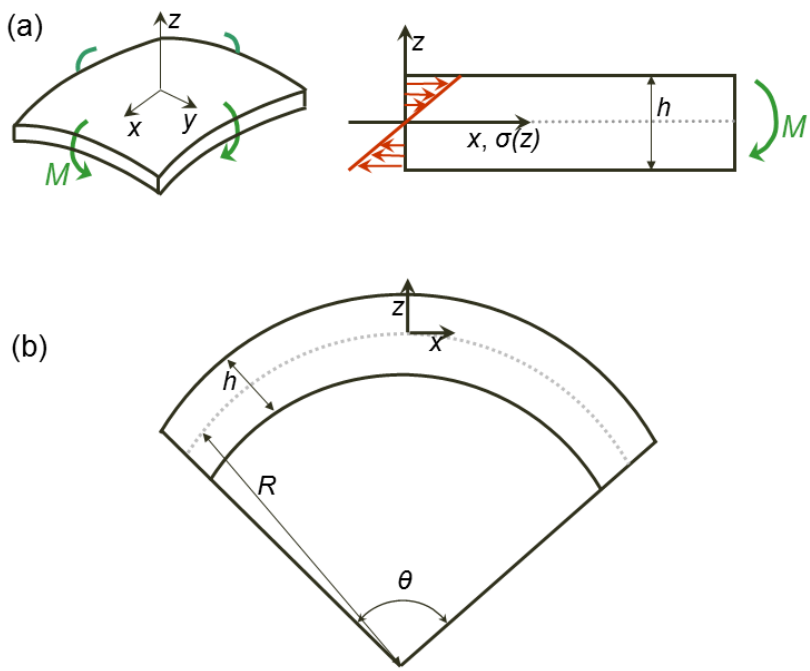

Figure 2.12 (a) Schematic of the bending of a thin plate when a biaxial stress is developed on the upper face; the stress distribution is shown in the cross-section. (b) Schematic of the radius of curvature for a bending plate.

Combining **Eq. (2.18)** and **Eq. (2.20)** gives the relationship between the bending moment and the curvature by the following equation:

$$K = -\frac{(1-\nu)}{E}\frac{12M}{h^3} \tag{2.22}$$

To apply to the status of the thin plate to the status of a thin film on the substrate, force equilibrium in the thin film on the substrate system should be considered. As depicted in **Figure 2.13**, a tensile force in the film produces a biaxial tensile stress, while a compressive force on the substrate produces biaxial compression and biaxial bending in the substrate (σ_f is the biaxial tension of the film). In other words, the edge force is divided into the bending moment and the normal stress. As a result, the bending moment in the substrate determines the curvature of the substrate by the following equation:

$$M = -\sigma_f h_f \frac{h_s}{2} \tag{2.23}$$

If **Eq. (2.23)** is combined with **Eq. (2.22)**, the substrate curvature induced by the stress in the thin film is expressed by the well-known Stoney equation:

$$\sigma_f = Y_s \frac{h_s^2}{6h_f} K = Y_s \frac{h_s^2}{6h_f R} \tag{2.24}$$

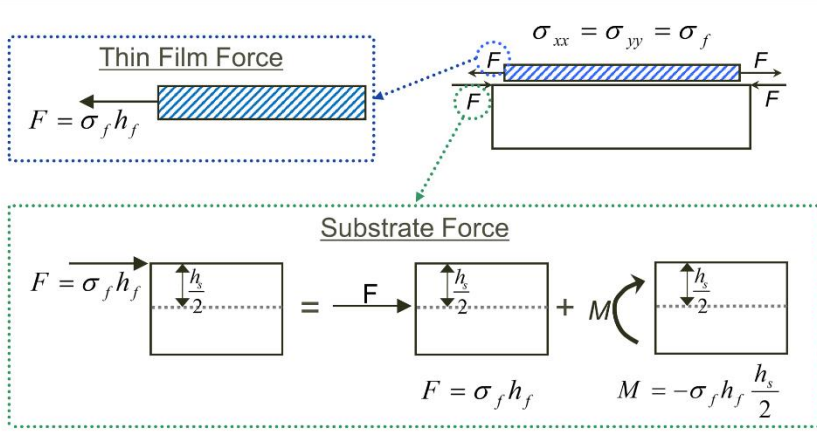

Figure 2.13 Force equilibrium in a thin film on a substrate, which results in the edge force being divided into the normal stress and the bending moment.

where Y_s is the biaxial elastic modulus of the substrate, and h_s and h_f are the thicknesses of the film and the substrate, respectively. It should be noted that the film stress depends only on the elastic properties of the substrate and the dimensions of the film and substrate, which means that the elastic properties of the film are not required for the calculation.

2.3.3. Elastic deformation

When an external force is applied to a solid, deformation occurs. If the solid returns to its original state when the external force is removed, the deformation is referred to as elastic deformation. The origin of the stress observed in an amorphous thin film that results in elastic deformation is described below, including thermal stress and volumetric stress.

Thermal stress is produced by heating or cooling of the film on the substrate due to the difference in the coefficients of thermal expansion (CTE) between the thin film and the substrate, which will produce thermal strains as follows:

$$\varepsilon_{thermal} = (\alpha_s - \alpha_f) \cdot \Delta T \tag{2.25}$$

where α_s is the coefficient of thermal expansion of the substrate, α_f is the coefficient of thermal expansion of the film, and ΔT is the temperature difference between the final and initial states of the sample. This thermal strain is translated to a biaxial stress using Hooke's law for a biaxial stress state in **Eq. (2.15)**:

$$\frac{d\sigma}{dT} = k = Y_f(\alpha_s - \alpha_f) \tag{2.26}$$

where Y_f is the biaxial modulus of the film. Measurements of the thermal stress with continuous heating can be used to determine the biaxial modulus and the coefficient of thermal expansion of the film. Because there are two unknown parameters (e.g., Y_f and α_f), measurements of $d\sigma/dT$ for the same thin film on two different substrates with well-known biaxial moduli and coefficients of thermal expansion are required to determine the two parameters, which is known as the two wafer method.

Volumetric stress is produced by isotropic and elastic volume changes of the thin film (as a result of phase transformation; e.g., crystallization). To calculate the volumetric strain, the film is assumed to be removed from the substrate as shown in **Figure 2.14**. With a change in volume of ΔV, the isotropic elastic volumetric strain is determined as follows:

$$\frac{\Delta V}{V} = 3\varepsilon_0 \tag{2.27}$$

Biaxial strain as high as $\varepsilon_{xx} = -\varepsilon_0$ is required to match the lateral dimension of the film and the substrate. The volumetric elastic stress ($\Delta\sigma_{elast}$) is determined by the following equation according to the biaxial strain (and volumetric strain).

$$\Delta\sigma_{elast} = Y_f \cdot \varepsilon_{xx} = -Y_f \cdot \varepsilon_0 \tag{2.28}$$

The decrease in film thickness along the *z*-axis is determined by two effects: the volumetric strain, ε_0, and the contraction along the *z*-axis due to expansion along the *x* and *y*-axes of the film. The final film thickness, ε_z, is determined as follows:

$$\varepsilon_z = \varepsilon_0 + \left(\frac{2\nu}{1-\nu} \right) \cdot \varepsilon_0 \tag{2.29}$$

Combining **Eq. (2.28)** and **Eq. (2.29)** gives:[16]

$$\Delta\sigma_{elast} = -Y_f \frac{1\text{-}\nu}{1+\nu} \varepsilon_z \tag{2.30}$$

The elastic volumetric stress in the thin film on the substrate is provided by the thickness change in the thin film associated with the volume change.

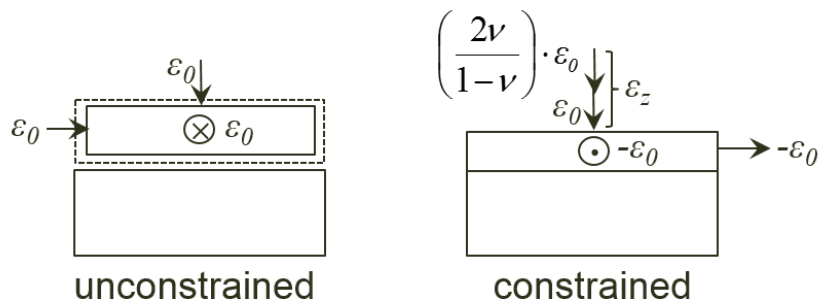

Figure 2.14 Schematic of film with volumetric changes removed from the substrate and attached to the substrate. In the removed film, the isotropic volume change occurs in the film. If the film is attached to the substrate, biaxial strain is produced.

2.3.4. Plastic deformation

If the external force is greater, the deformation undergoes irreversible changes that are known as yielding. Deformation above this yield point is referred to as plastic deformation.

Unlike elastic deformation, plastic deformation requires permanent changes in the atomic structures. In crystalline materials, plastic deformation is achieved by the motion of dislocations through the crystalline lattice. The dislocation is a line defect that causes slip between crystalline planes when they pass, which results in plastic deformation in the crystalline solids.

If a crystalline material experiences time-dependent plastic deformation, the deformation mechanism induced by diffusion needs to be considered in addition to the deformation mechanism induced by dislocation. This time-dependent plastic deformation in a crystalline material is referred to as creep[80].

Glass is not able to rely on plastic deformation induced by dislocation motion because there is no crystalline lattice in which dislocations can move. Instead, time-dependent plastic deformation triggered by diffusion can occur in glass due to the characteristic liquid-like structure. Plastic deformation in glass induced by diffusion is referred to as viscous flow.

Viscous flow is a time-dependent plastic deformation mechanism that relies on the diffusional motion of atoms in the glass structure. Because viscous flow occurs at the centers of flow defects, its deformation behavior is controlled by the viscosity as described by following equation:

$$\tau = \eta \cdot \dot{\gamma} \tag{2.31}$$

where $\dot{\gamma}$ is a strain rate, and τ is the shear stress that causes plastic deformation.

The viscous flow of amorphous materials occurs in the direction of the residual stress in the film to be relieved and becomes zero as a result. If we assume isothermal conditions (T = const.), the total biaxial strain of the film constrained on the substrate will be constant over time as follows:

$$\varepsilon_e + \varepsilon_p = const. \tag{2.32}$$

where ε_e is the elastic biaxial strain, and ε_p is the plastic biaxial strain. When **Eq. (2.32)** is differentiated with respect to time:

$$\dot{\varepsilon}_e + \dot{\varepsilon}_p = 0 \tag{2.33}$$

where ε_e is the elastic biaxial strain rate, and ε_p is the plastic biaxial strain rate. Hooke's law for the elastic biaxial stress condition in **Eq. (2.15)** was used to derive the elastic biaxial strain rate, which can be determined by following equation:

$$\dot{\varepsilon}_e = \frac{\dot{\sigma}}{Y_f} \tag{2.34}$$

For the derivation of the plastic biaxial strain rate, equivalent stresses were introduced as suggested by Von Mises. Because the viscous flow is independent of the basis, equivalent stresses and strains that are independent of the choice of basis were introduced. Based on the calculation procedure and considering the pure shear stress

case and the pure biaxial stress case, the equation for the plastic biaxial strain rate is obtained as follows:

$$\dot{\varepsilon}_p = \frac{\sigma}{6\eta} \tag{2.35}$$

The relationship between the biaxial stress of the film and the viscosity in accordance with the concept of viscous flow at a constant temperature is found by combining **Eq. (2.33)**, **Eq. (2.34)** and **Eq. (2.35)**:

$$\frac{\sigma}{6\eta} + \frac{\dot{\sigma}}{Y_f} = 0 \tag{2.36}$$

The viscous flow in an amorphous thin film on a substrate for a biaxial stress in the thin film for isothermal conditions (T = const.) can be described using **Eq. (2.36)**. If the viscosity is assumed to be time independent, the equation for the viscous flow can be expressed in a simple form as follows:

$$\ln\left(\frac{\sigma(t)}{\sigma_0}\right) = -\frac{Y_f}{6\eta}t \tag{2.37}$$

where σ_0 is the stress at $t = 0$. This equation describes the time-dependent stress change associated with viscous flow; i.e., stress relaxation. However, it should be noted that this equation was developed with the assumption of time-independent viscosity. The model for time-independent viscosity induced by structural relaxation was addressed in **Sec.**

2.1.5. For constant temperature, combining the time dependence of viscosity in **Eq. (2.14a)** (bimolecular defect annihilation model) and **Eq. (2.14b)** (unimolecular defect annihilation model) with the stress and viscosity relationship in **Eq. (2.36)** gives:

$$\ln\left(\frac{\sigma(t)}{\sigma_0}\right) = -\frac{Y_f}{6k}\ln\left(1+\frac{k}{\eta_0}t\right) \tag{2.38a}$$

$$\ln\left(\frac{\sigma(t)}{\sigma_0}\right) = -\frac{Y_f}{6k_r\eta_0}(1-\exp(-k_r t)) \tag{2.38b}$$

The stress relaxation with time can be described using these models, and the associated viscosity change with time can be obtained using the parameters (e.g., k, k_r and η_0). This time-dependence of viscosity is also important for understanding the kinetics of defect annihilation. The change in defect concentration with time can be obtained by combining the time-dependent viscosity and **Eq. (2.11)**.

CHAPTER 3

Experimental procedures

3.1. Sample preparation

To study the amorphous phase change materials, amorphous $Ge_2Sb_2Te_5$ (GST) thin films were deposited onto Si (or glass) substrates using direct current (DC) or radio frequency (RF) magnetron sputtering. Various dopants were inserted into the GST films during deposition. The individual deposition conditions for the GST films with the various dopants are listed in **Table 3.1**. For N doping of GST, DC magnetron sputtering was used at room temperature, and the working pressure was 3 mTorr. The ambient conditions in the vacuum chamber were controlled by the flow rate of N_2 gas (2 to 12 sccm) with Ar gas (fixed to 40 sccm) used to control the N concentration in the GST thin film. For the Bi-doped GST, DC magnetron sputtering was used at room temperature, and the working pressure was 3 mTorr. Co-sputtering of the $Ge_2Sb_2Te_5$ target and the $Ge_2Bi_2Te_5$ target was used. Several DC powers of the $Ge_2Bi_2Te_5$ target (5 to 40 W) were used with a fixed DC power of the $Ge_2Sb_2Te_5$ target (80 W) to control the Bi concentration in the GST thin film. For C doping of GST, RF magnetron sputtering

was used at room temperature with a working pressure of 0.5 mTorr. Co-sputtering of the $Ge_2Sb_2Te_5$ target and the C target was used. Several RF powers of the C target (11 to 89 W) with a fixed RF power of the $Ge_2Sb_2Te_5$ target (30 W) were used to control the C concentration in the GST thin film. For the Al-doped GST, RF magnetron sputtering was used at room temperature with a working pressure of 0.5 mTorr. Co-sputtering of the $Ge_2Sb_2Te_5$ target and the Al target was used. Several RF powers of the Al target (5 to 30 W) and a fixed RF power of the $Ge_2Sb_2Te_5$ target (30 W) were used to control the Al concentration in the GST thin film. The concentration of dopants in the GST film were determined using Rutherford backscattering spectrometry (RBS) as shown in **Figure 3.1**. The phases of all of the as-deposited GST thin films were observed to be amorphous and were confirmed by grazing incident x-ray diffraction (GIXRD, New D8 Advance).

To study the amorphous oxide semiconductors, amorphous $In_{25}Ga_{44}Zn_{31}O_x$ films were prepared on Si substrates by RF magnetron sputtering of a single $InGaZnO_x$ target at room temperature. The working pressure was 5 mTorr. The thickness of the IGZO films was varied from 20 nm to 300 nm by controlling the deposition time. The RF power of the $InGaZnO_x$ target was 50 W, and the gas mixing ratio was Ar/O_2 = 99/1. The amorphous state of the as-deposited IGZO film was confirmed by GIXRD.

The thickness of the Si substrate was reduced from 525 μm to 100-300 μm using chemical mechanical polishing (CMP) to improve the sensitivity of the mechanical stress analysis according to the Stoney equation, which will be described in **Sec. 3.2.3**. The As-CMP thinned Si substrate was subsequently heated to 500 ℃ for 24 hours before deposition of the film to unbend the substrate ($K \sim \pm 0.005\ m^{-1}$).

Table 3.1 Sputtering conditions for the preparation of the $Ge_2Sb_2Te_5$ films.

	Target	**Power**	**Gas flow**
$Ge_2Sb_2Te_5$ (GST)	$Ge_2Sb_2Te_5$	DC 80 W	Ar: 40 sccm
N-doped GST	$Ge_2Sb_2Te_5$	DC 80 W	Ar: 40 sccm N_2: 2-12 sccm
Bi-doped GST	$Ge_2Sb_2Te_5$	DC 80 W	Ar: 40 sccm
	$Ge_2Bi_2Te_5$	DC 5-40 W	
$Ge_2Sb_2Te_5$ (GST)	$Ge_2Sb_2Te_5$	RF 30 W	Ar: 20 sccm
C-doped GST	$Ge_2Sb_2Te_5$	RF 30 W	Ar: 20 sccm
	C	RF 11-89 W	
Al-doped GST	$Ge_2Sb_2Te_5$	RF 30 W	Ar: 20 sccm
	Al	RF 5-30 W	

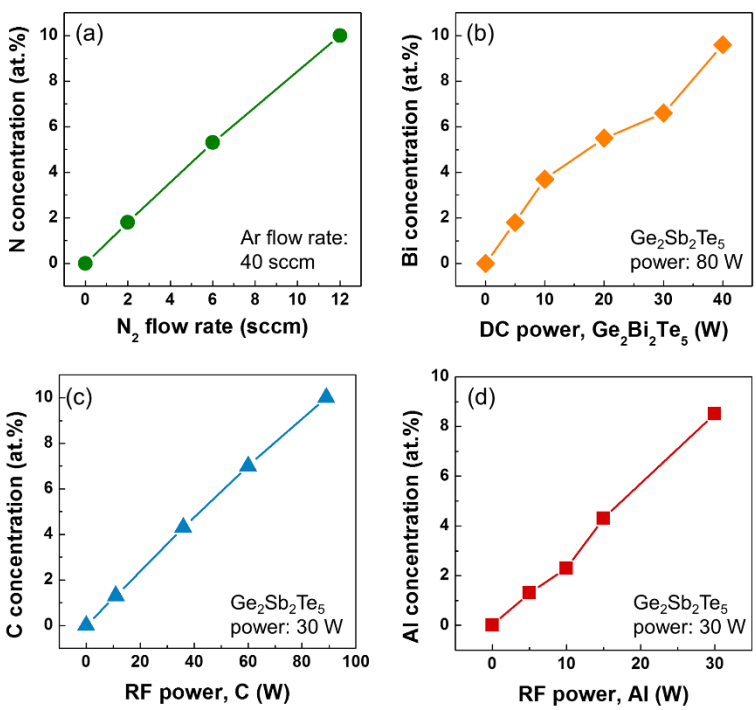

Figure 3.1 Dopant concentrations in the $Ge_2Sb_2Te_5$ films as a function of deposition conditions detected by Rutherford backscattering spectrometry (RBS). (a) N concentration as a function of the N_2 flow rate. (b) Bi concentration as a function of the DC power of the $Ge_2Bi_2Te_5$ target. (c) C concentration as a function of the RF power of the C target. (d) Al concentration as a function of the RF power of the Al target.

3.2. Mechanical stress analysis

3.2.1. Investigation of structural changes in amorphous films

Differential scanning calorimetry (DSC), reflectivity, and x-ray diffraction were used to investigate the structural changes of the amorphous materials. Crystallization is relatively easy to detect because of the significant changes in the relevant material properties, while detecting the glass transition is difficult due to the small changes in those properties. DSC is the most commonly used method; however, it is unsuitable for thin films. Although the thickness changes at the glass transition, the optical path of a film is too small to detect the slight change in thickness that is associated with the glass transition. We propose measuring the stress changes due to volume change in the horizontal direction rather than in the normal direction. Small changes in the volume of the film cause substantial changes in the curvature of the film/substrate system.[24] A change in the volume of the film of 0.015 % produces a change in thickness of ~0.005 % and a stress change of ~5 MPa (assuming elastic behavior) in a detectable range (> ~1 MPa for a 300-nm-thick film on a 100-μm-thick Si substrate) as described in **Sec. 3.2.3**. Thus, we suggest analyzing the biaxial mechanical stress in thin films to measure the structural changes in amorphous thin films (see the comparison in **Table 3.2**).

Table 3.2 Comparison of methods of measuring structural changes in amorphous materials.

	Measurement	**Crystalli-zation**	**Glass transition**	**Structural relaxation**	**Limitations**
Ellipsometry	Film thickness	O	Δ	O	Oxide films only
DSC	Heat capacity	O	Δ	X	Powder preferred
XRD	Crystal structure	O	X	X	Crystalline only
Optical analysis	Reflectivity	O	X	X	Reflective films only
Electrical analysis	Resistance	O	X	O	
Mechanical analysis	**Biaxial film stress**	**O**	**O**	**O**	**Thin films only**

3.2.2. Operating principles

To measure the volumetric changes associated with the structural changes in amorphous materials and the viscosity changes associated with viscous flow and structural relaxation, the mechanical stress of the thin film is quantified. To measure the mechanical stress in the thin film, a substrate curvature measurement system using a k-Space® multi-beam optical sensor (MOS) was developed. The substrate curvature measurement system using MOS is a non-destructive measurement technique that detects the change in curvature of a substrate associated with the stress evolution in a thin film. The measured curvature is translated to the mechanical stress of the thin film using the Stoney equation in **Eq. (2.24)**. This measurement method can be utilized for real-time measurements of the stress evolution in thin films during heat cycling as well as under isothermal annealing conditions.

Figure 3.2 shows the principle of the substrate curvature measurement system using MOS. An array of parallel beams illuminates the film on the bended substrate, and the spacings of the reflected beams are detected by a charge-coupled device (CCD) camera. The change in curvature of the substrate (ΔK) is obtained from the deflection of the parallel beams reflected from the surface of the film by the following equation:

$$\Delta\kappa = \left(\frac{\delta d}{d_0}\right)\frac{\cos\alpha}{2L} \tag{3.1}$$

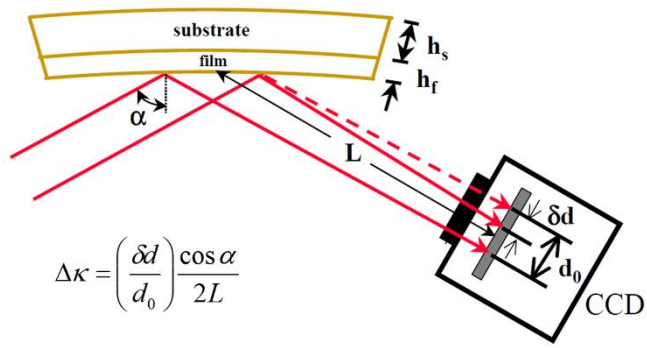

Figure 3.2 Schematic of the substrate curvature measurement system using a multi-beam optical sensor (MOS). An array of parallel beams irradiates the bended substrate and is reflected. The reflected beams are detected by a CCD camera [*k*-Space Associates, Inc.].

where L is the distance between the CCD and the film, α is the angle between the beam and the normal direction to the film, δd is the difference in the spacing of the incident beams and the reflected beams, d_0 is the beam spacing of the incident beams, and $\delta d/d_0$ is the differential spacing. The obtained curvature change (ΔK) can be translated to the mechanical stress of the film using the Stoney equation in **Eq. (2.24)**.

3.2.3. Set-up used in this study

To facilitate the real-time measurement of the stress evolution in a thin film during heat cycling or isothermal annealing, the sample heating system with MOS was set up in a vacuum chamber as shown in **Figure 3.3**. The MOS is located on top of the chamber, and the incident beam irradiates the sample on the heating stage in the chamber. The base pressure of the chamber is set to approximately 5×10^{-6} Torr, and the atmosphere in the chamber can be controlled by inserting N_2, Ar or O_2 gas. The working pressure is set to 3 - 5 Torr to avoid interference of the beam due to air convection at elevated temperatures. A 4-in-diameter heating stage is located in the chamber to apply the heat to the sample. For a heating range from room temperature to 620 ℃, the maximum heating rate is 5 K/min. For a heating range from room temperature to 400 ℃, the maximum heating rate is 20 K/min.

A 20 mm by 20 mm sample holder is set up to minimize the drift of the sample due to vibrations or thermal expansion. The lateral dimension of the sample (thin film on substrate) is 19 mm by 19 mm. A thermocouple with the same dimensions and structure is located on the heating stage to measure the real-time temperature changes of the sample. A feed-through is located on the side of the chamber to transport the signal in and out of the chamber (e.g., electrical resistance, temperature)

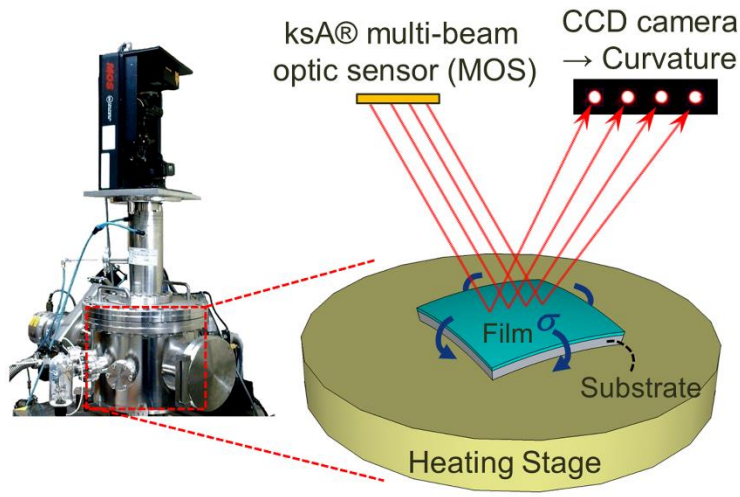

Figure 3.3 Real-time substrate curvature measurement using a multi-beam optical sensor (MOS) set up in the laboratory. The curvature is determined from the beam spacing, and the biaxial stress of the film was then determined from the changes in curvature according to the Stoney equation.

Real-time electrical and mechanical analysis by substrate curvature measurements was used to investigate the mechanical stress and electrical resistance. **Figure 3.4** shows a schematic image of the real-time substrate curvature measurement used to measure the mechanical stress and electrical resistance under the same conditions. This method utilizes the GST that is metal-wired to the edge to measure the electrical resistance while measuring the curvature of the substrate using the multi-beam optical system. A Keithley 2400 SourceMeter® was utilized for the electrical characterization.

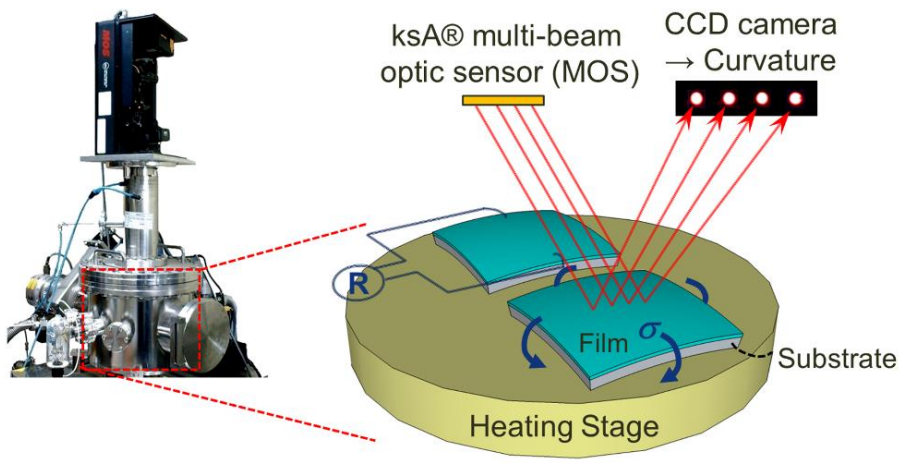

Figure 3.4 Real-time substrate curvature measurement using a multi-beam optical sensor (MOS) set up in laboratory to measure the mechanical stress and electrical resistance under the same conditions.

3.2.4. Resolution and sensitivity

Resolution **Figure 3.5(a)** shows the curvature of a 50-nm-thick IGZO film on a 100-μm-thick Si substrate during heating from room temperature to 300 ℃. The red line indicates the linear fit of the curvature change with the assumption of thermal strain evolution (**Sec. 2.3.3**). **Figure 3.5(b)** shows the difference between the measured data and the fitted line. The standard deviation of the curvature is 0.0017 m^{-1} for heating from room temperature to 300 ℃. Because the data are randomly distributed, there is no directional drift in the signal. The standard deviation of the curvature corresponds to the minimum detectable curvature of the set-up at Seoul National University.

Sensitivity The resolution obtained above is the minimum detectable curvature; however, this curvature must be translated to the minimum detectable stress. In accordance with the Stoney equation in **Eq. (2.24)**, the minimum detectable stress can be determined from the thickness of the film (h_f) and the thickness of the substrate (h_s). The sensitivity of the mechanical stress measurement (the ratio between the stress in the thin film (σ_f) and the curvature of the substrate (ΔK)) is inversely proportional to the square of h_s and is proportional to h_f. Therefore, the minimum detectable stress decreases as h_s decreases, and h_f is larger for the same minimum detectable curvature.

As determined from the resolution of curvature in **Figure 3.5(b)**, the minimum detectable curvature during heating (from room temperature to 300 ℃) is 0.0017 m^{-1}. **Figure 3.5(c)** shows the linear curve of the minimum detectable stress as a function of the minimum detectable curvature according to the Stoney equation given in **Eq. (2.24)**. For the set-up at Seoul National University, the minimum detectable stress is determined to be 1.0 MPa for h_s of 100 μm and h_f of 300 nm.

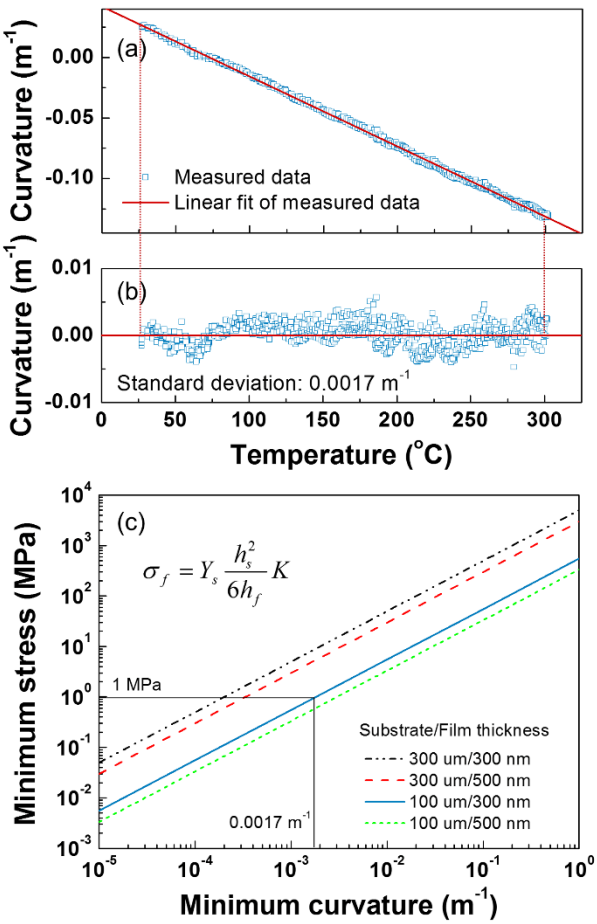

Figure 3.5 (a) Curvature of a 50-nm-thick a-IGZO film on a 100-μm-thick Si substrate during heating from room temperature to 300 ℃. The red line indicates the linear fit of the curvature change with the assumption of thermal strain evolution. (b) The difference between the measured data and the fitted line; the standard deviation of the curvature is 0.0017 m^{-1} for the heating conditions in (a). (c) The minimum detectable stress as a function of the minimum detectable curvature according to the Stoney equation.

CHAPTER 4

Effects of doping on the phase stability of amorphous Ge-Sb-Te

4.1. Introduction

Loss of the information stored in the high-resistance state, which is called data retention loss, inhibits the reliability and limits the competitiveness of PcRAM. This problem stems from the crystallization kinetics, which describe the interplay of time and temperature on the amorphous state. The SET speed and data retention of PcRAM are determined by the crystallization kinetics of phase change materials; because crystallization at high temperature determines the SET speed, it needs to be fast. Meanwhile, crystallization at low temperature determines the data retention loss; hence, it should be limited.[6] Achieving this goal requires a breakthrough in our understanding of this unique class of materials. As discussed in **Sec. 2.2.1.**, phase change materials are the inorganic solids with the highest fragility. In other words, the crystallization behaviors at low and high temperatures are not completely independent but do not have a strong relationship, such as the Arrhenius relationship.

These unique characteristics of amorphous phase change materials have two important consequences. First, this behavior helps amorphous phase change materials achieve high stability at low temperatures and rapid crystallization at higher temperatures because the characteristics of crystallization at low and high temperatures are not strongly related. This implies that different atomic mechanisms operate at high and low temperatures. Second, it is possible to predict the crystallization behavior over the entire temperature range only if the non-Arrhenius crystallization kinetics of a given phase change material are understood.

For this reason, experiments have recently been proposed to rapidly and directly measure crystallization at high temperatures. M. Wuttig *et al.* measured the crystallization rates of amorphous phase change materials that are rapidly melt-quenched using a reflectance measurement with a laser.[46] A. L. Greer *et al.* investigated the crystallization kinetics of phase change materials using ultra-fast differential scanning calorimetry (DSC).[36] Based on these experiments, the crystallization rate of the entire temperature interval from room temperature to the melting point was intensively investigated.

To understand the crystallization behavior of amorphous phase change materials, mechanical stress analysis was used to investigate the volumetric and viscosity changes in amorphous thin films utilizing the substrate curvature measurement system with a multi-beam optical sensor.[24]

To control the crystallization behavior of the phase change material, several substances are utilized as dopants, such as N, C, Al and Bi. Depending on the nature of the elements of these dopants, the short range order, bonding enthalpy and other structural features are altered; thus, the structural stabilities of the phase change materials vary with the doping. Many of the structural changes and relevant crystallization

behaviors associated with doping have been identified through the theoretical and experimental studies described in **Table 2.1**.

In this study, we employed a mechanical analysis to monitor the glass transition and crystallization of amorphous GST films with C, N, Al and Bi doping. Based on the theoretical and experimental analyses, the effect of doping on the amorphous structure was determined. This task is crucial because device cell characterization, which is time-consuming, can be replaced by simple thin film characterization.

4.2. Experiments

Amorphous $Ge_2Sb_2Te_5$ films were deposited onto Si wafers by DC magnetron sputtering at room temperature. The gun power and the chamber pressure were 80 W and 3 mTorr, respectively. Al-, Bi-, C- and N-doped GST films were prepared according to the deposition conditions and doping concentration described in **Sec. 3.1**.

The substrate curvature measurement system with a multi-beam optical sensor (kSA Multibeam Optical System) depicted in **Figure 3.3** was used to determine the mechanical stress in the film during thermal cycling in an N_2 atmosphere at 5 Torr.

4.3. Stress evolution during heat cycling

Stress change curves of amorphous GST films as a function of temperature upon heating are shown in **Figure 4.1**. Positive and negative values indicate tensile and compressive stresses, respectively, in the film. When the temperature increases to

~70 ℃ at a heating rate of 1 K/min, the stress was compressive because the film has a larger coefficient of thermal expansion (CTE) than the Si wafer (denoted as 1). From 70-120 ℃, the stress became tensile, which indicates that volume shrinkage occurred in the film associated with structural relaxation (denoted as 2). After heating above ~150 ℃, the stress rapidly became more tensile, which indicates that the volume decreased by crystallization (denoted as 4); this temperature is thus T_x, which was confirmed by the increase in the reflected intensity measured at the same time as the stress data. Stress relaxation occurs above T_x to relieve the stress that built up during the crystallization process.

For the Al-doped GST (Al-GST) films shown in **Figure 4.2(a)**, T_x increased with increasing Al concentration, which was detected by the delayed temperature of the abrupt tensile stress evolution. Conversely, Bi-doped GST (Bi-GST) shows decreasing T_x with increasing Bi concentration, as shown in **Figure 4.2(b)**. As indicated in **Figure 4.3(a)**, the stress-temperature curves of C-doped GST (C-GST) also showed increasing values of T_x with increasing C concentration. The stress-temperature curve of N-doped GST (N-GST) in **Figure 4.3(d)** also shows increases in T_x with N concentration, which is similar to the case of C-GST. T_x increases with Al, C and N doping but decreases with Bi doping.

However, the stress change curves as a function of temperature for C- and N-GST exhibit different behaviors from those of Al- and Bi-GST. Above 150-200 ℃, the stress became compressive, which was never observed in pure Al- and Bi-GST. This change is the glass transition, which makes this temperature T_g (denoted as 3); the volume increases. T_g increases with C and N doping, and the narrow regions of super-c ooled liquid (T_x - $T_g \approx 0$) of pure GST become wider for C and N doping; thi s is shown in **Figures 4.3(c)** and **(d)**.

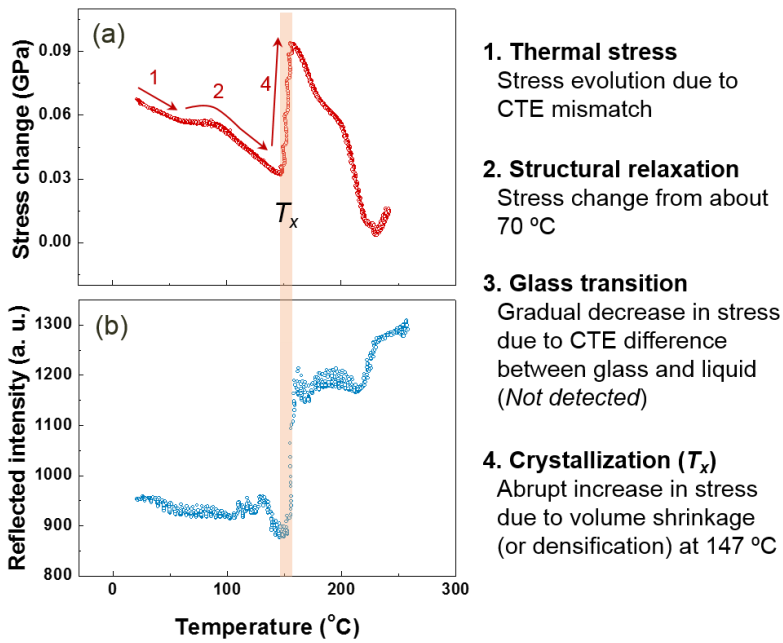

Figure 4.1 (a) Stress change and (b) reflected intensity of a pure GST film during heat cycling. The crystallization temperature is denoted as T_x. Inflection points in the curve of stress change as a function of temperature indicate structural changes in the GST film.

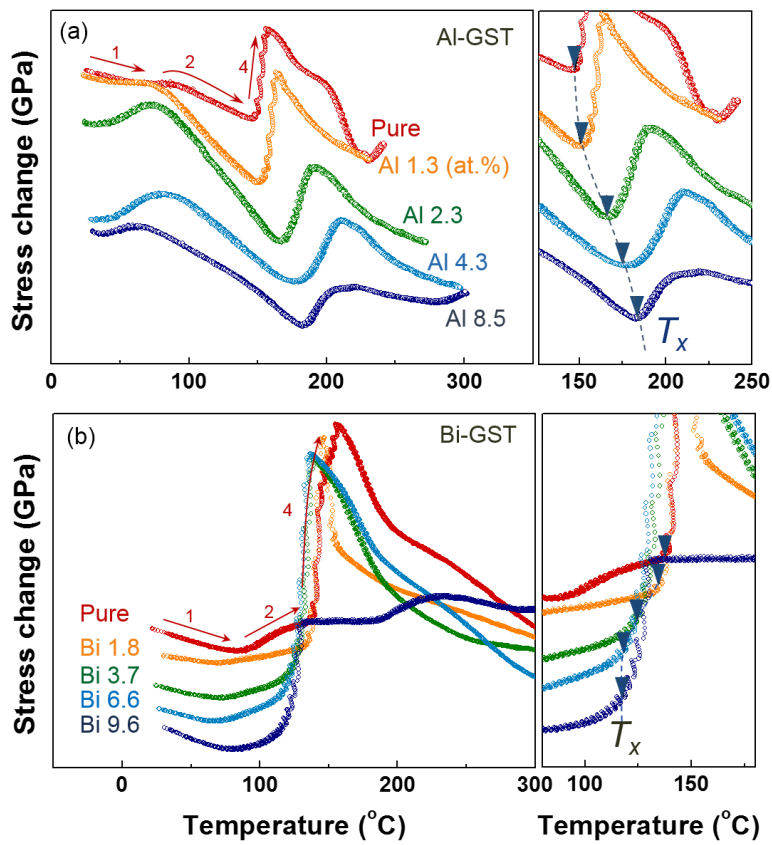

Figure 4.2 Stress-temperature curves of (a) Al-doped and (b) Bi-doped GST films during heating. Magnified views are shown on the right side of each graph (arrows indicate T_x). Stress changes associated with thermal expansion, structural relaxation and crystallization are denoted as 1, 2 and 4, respectively.

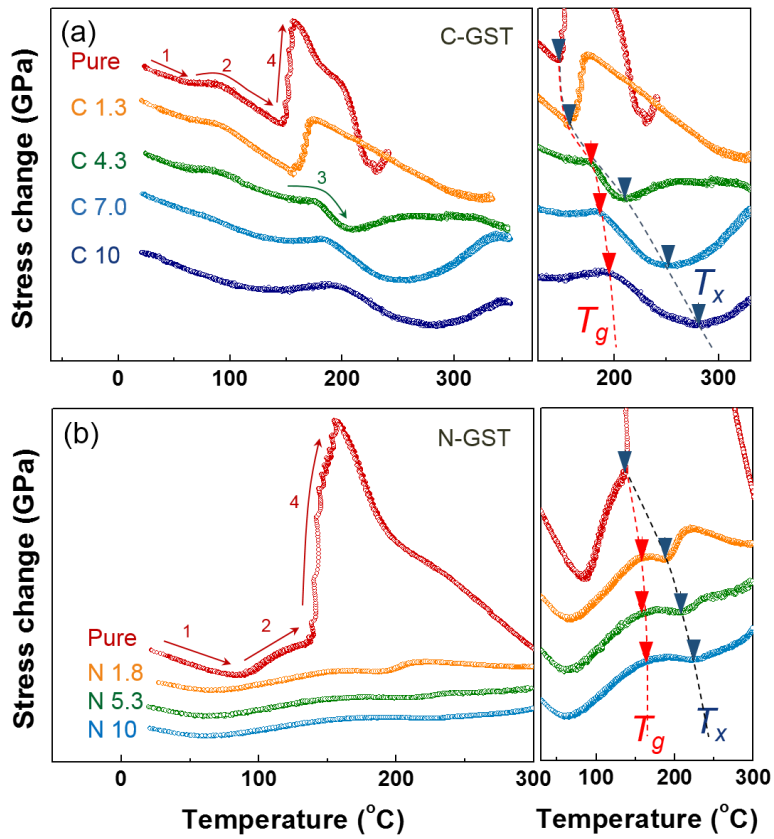

Figure 4.3 Stress-temperature curves of (a) C-doped and (b) N-doped GST films during heating. Magnified views are shown on the right side of each graph (arrows indicate T_x and T_g). Stress changes associated with thermal expansion, structural relaxation, glass transition and crystallization are denoted as 1, 2, 3 and 4, respectively.

4.4. Structural changes in amorphous GST

4.4.1. Crystallization

T_x increases with Al, C and N doping, while Bi doping decreases T_x as shown in **Figure 4.4(a). Figure 4.4(b)** shows the dependence of the glass transition temperature (T_g) as a function of Al, Bi, C and N concentration determined from the stress change-temperature curves in **Figure 4.2** and **Figure 4.3**. T_g increases with Al, C and N doping and decreases with Bi doping. Conversely, **Figure 4.4(c)** shows completely different effects of doping for the super-cooled liquid region (T_x - T_g). The narrow super-cooled liquid regions (T_x - $T_g \approx 0$) of pure GST are maintained in Al and Bi but widen with C and N doping. The different effects of doping on T_g and T_x - T_g can be explained by different atomic mechanisms: bonding enthalpy and free volume.

4.4.2. Glass transition

The glass transition refers to the phenomenon in which a solid-like glass changes to a liquid-like super-cooled liquid. Because the amorphous network is partially destroyed upon reaching T_g, especially in covalent bonding systems of amorphous phase change materials, a larger bonding enthalpy leads to a higher T_g.[81, 82] Consequently, the glass transition temperature (T_g) is a *bonding enthalpy-related factor*, which is determined mainly by the bonding enthalpy in amorphous phase change materials. Because T_g is the minimum temperature at which crystallization can occur, T_g can be regarded as a quantitative measure of the *thermal stability against crystallization* at low temperatures.

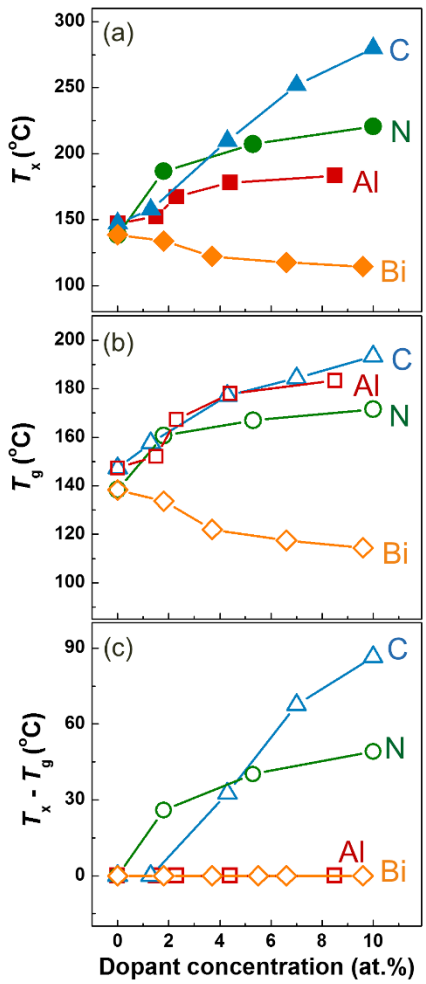

Figure 4.4 (a) T_x, (b) T_g and (c) T_x - T_g as a function of dopant concentrations of Al, Bi, C and N in GST films.

At temperatures above T_g, super-cooled liquid of pure GST experiences a rapid increase in atomic mobility with temperature, which provides sufficient mobility for crystallization to occur. Crystallization below T_g is extremely slow due to the high energy barrier for atomic rearrangement, and T_g can be regarded as the lower limit of T_x. Therefore, T_x is considered to be T_g for pure, Al- and Bi-GST, and T_g is not detected because $T_x \approx T_g$.

Doping in GST changes the bonding enthalpy by substitution of bonding or additional bonding. C-GST is known to produce additional bonding, such as C-Ge, C-Te and C-C bonds, N-GST produces additional N-Ge bonding, and Al-GST produces additional bonding of Al-Sb and Al-Te. In contrast, Bi-GST substitutes bonds from Sb-Te to Bi-Te, which causes weaker bonding. The changes of bonding enthalpies associated with doping explain the changes of T_g. Because T_g is the minimum temperature at which crystallization can occur, a higher T_g can be regarded as higher thermal stability against crystallization at temperatures below T_x. Therefore, it is expected that Al, C and N-GST lead to higher thermal stability, while Bi-GST leads to lower thermal stability compared to pure GST.

4.4.3. Super-cooled liquid region

At temperatures above T_g, the super-cooled liquid experiences a rapid increase in atomic mobility as a function of temperature, which is then sufficient for crystallization to occur. Therefore, the temperature dependence of atomic mobility controls crystallization in the super-cooled liquid region. If the increase in atomic mobility above T_g is abrupt, crystallization will be accelerated due to the easy atomic rearrangement, which results in a narrow super-cooled liquid region. Conversely, if the increase in

atomic mobility above T_g is gradual, crystallization will be delayed due to difficult atomic rearrangement, which results in a higher T_x - T_g. Because the free volume in an amorphous network acts as the center of the atomic arrangement, a larger amount of free volume leads to an abrupt increase in atomic mobility above T_g and a lower T_x - T_g. Therefore, the super-cooled liquid region (T_x - T_g) is a *free volume-related factor*, which is determined mainly by the free volume in amorphous phase change materials. The super-cooled liquid region can be regarded as a quantitative measure of the *atomic mobility during crystallization* at high temperatures.

The measurement and comparison of T_g and T_x enable us to obtain the super-cooled liquid region, which is defined as $T_x - T_g$. The values of T_x and T_g ($T_x \approx T_g$) in pure GST are similar due to the narrow super-cooled liquid region. Because T_g is not detected in Al- and Bi-GST, Al and Bi doping do not change the features of the narrow super-cooled liquid region. However, in C- and N-GST, the super-cooled liquid region becomes wider ($T_x > T_g$) with increasing dopant concentration.

Schematics of the structural changes associated with doping are shown in **Figures 4.5(a)-(c)**. As depicted in **Figure 4.5(a)**, abundant amounts of free volume are contained in pure GST, and the highly mobile nature is attributed to this free volume. Al and Bi are known to be substitutional dopants that occupy sites of constitutive atoms, and the free volume in the system will not be significantly occupied as shown in **Figure 4.5(b)**. This structural feature of Al- and Bi-GST results in the high atomic mobility in the system, which is manifested in a lower T_x - T_g. In contrast, C and N are both known to be interstitial dopants and occupy free volume sites as depicted in **Figure 4.5(c)**.[49, 83] These structural features of C and N-GST result in the lower atomic mobilities of the systems, which are manifested in higher T_x - T_g.

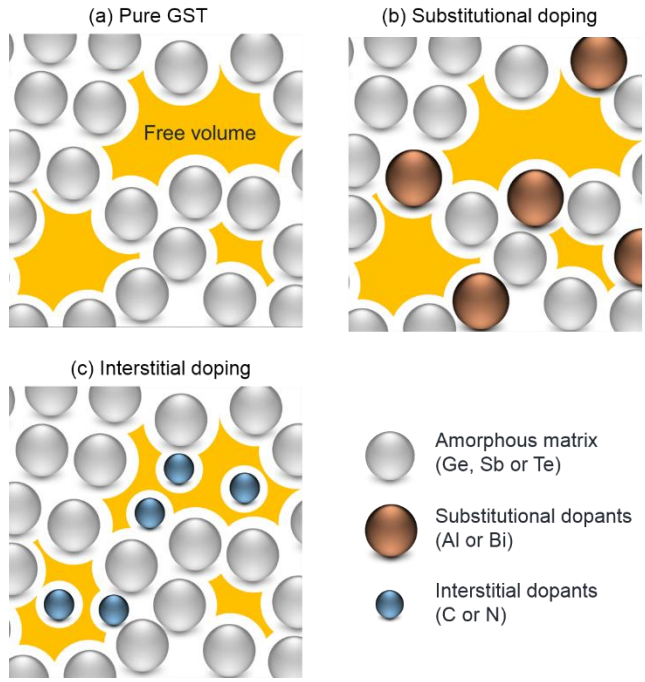

Figure 4.5 Schematic images of the structural changes in (a) pure GST, (b) substitutional doping and (c) interstitial doping.

4.4.4. Model for the effects of doping

Figure 4.6 illustrates the difference between the bonding enthalpy-related factor and the free volume-related factor by showing schematics of atomic mobility vs. temperature. When the temperature of glass increases above T_g, the super-cooled liquid experiences a rapid increase in atomic mobility. Because the amorphous network needs to be partially destroyed upon reaching T_g, a lower bonding enthalpy leads to a lower T_g as in Bi-GST. Conversely, a higher bonding enthalpy results in a higher T_g as in Al-GST. The narrow super-cooled liquid region is maintained in Al- and Bi-GST. Because the free volume in the network acts as the center of the atomic arrangement, a larger amount of free volume leads to an abrupt increase in atomic mobility above T_g and a lower T_x - T_g. If the free volume decreases, crystallization will be delayed due to the difficult atomic rearrangement, which results in a higher T_x - T_g as in the case of C- and N-GST.

4.5. Viscosity of amorphous GST

4.5.1. Fragility

To facilitate the discussions presented in **Sec. 4.4.4.**, it is useful to represent the atomic mobility of GST as a function of temperature. It is expected that Al- and Bi-GST, which have lower T_x - T_g, experience abrupt increases in atomic mobility with temperature, while C- and N-GST, which have higher T_x - T_g, experience gradual increases in atomic mobility with temperature. To identify the effect of doping on the temperature dependence of atomic mobility, the viscosity was examined.

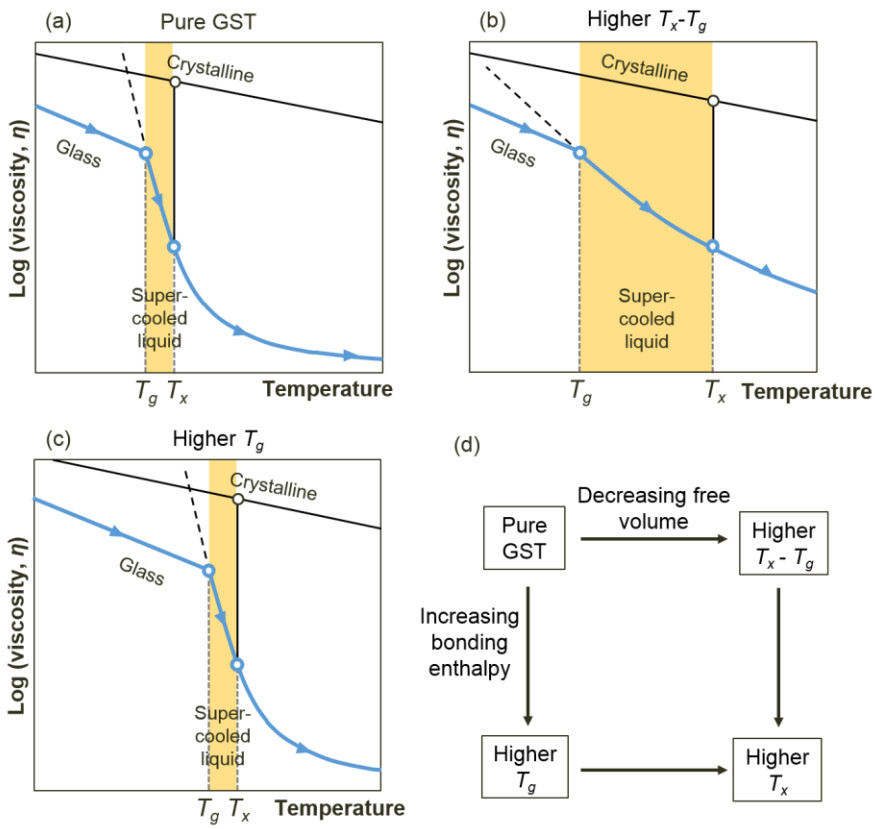

Figure 4.6 Schematics of the reciprocal of atomic mobility as a function of temperature in amorphous materials, which describes the difference between the bonding enth alpy-related factor and the free volume-related factor.

As discussed in **Sec. 2.1.3**, viscosity is the resistance to atomic flow. The relaxation time, which is the time required for structural changes from non-equilibrium to equilibrium. The viscosity and the relaxation time have similar temperature dependencies and physical meanings (e.g., inversely proportional to atomic mobility).

The temperature dependence of the viscosity in a super-cooled liquid is believed to be a result of structural changes in amorphous GST by different dopings. Therefore, the temperature dependence of the viscosity h(η) can be utilized to determine the well-known universal criterion for the kinetic stability of an amorphous structure, fragility.[30] The fragility (m) is determined by the deviation of the relaxation time vs. temperature from the Arrhenius relationship, which was shown in **Eq. (2.3)**:[30]

$$m = \left.\frac{d\log\eta(T)}{d(T_g/T)}\right|_{T=Tg} = \left.\frac{d\log\tau(T)}{d(T_g/T)}\right|_{T=Tg} \tag{2.3}$$

Strong and fragile super-cooled liquids are classified as follows. As m approaches 16, the Arrhenius relationship yields, and the liquid is categorized as "strong". Larger values of m reveal non-Arrhenius relationships and are categorized as "fragile". Detailed explanations are provided in **Sec. 2.1.4**. This non-Arrhenius relaxation causes the activation energy for relaxation to vary with temperature; therefore, the apparent activation energy for relaxation (E) was defined at T_g for the experimental characterization. This apparent activation energy for relaxation (E) can be extracted from the kinetic nature of the glass transition according to the Moynihan plot.[38] A shift of T_g towards higher temperatures as the heating rate increases is generally observed, and this characteristic shift of T_g is used to calculate E in **Eq. (2.9)**:[38]

$$\ln \beta = -\frac{E}{RT_g} + C \tag{2.9}$$

where β is the heating rate (K/min), and C is constant.

Figure 4.7 shows the dependence of the stress evolution on the heating rate (1.0, 2.5, 6.5, 13 and 20 K/min) during heating of GST films that are doped with various dopants. The inflection points indicate that T_g and T_x increase as the heating rate increases. With increases in the heating rate, T_g of doped GST also increases. The T_g values are obtained from the stress change-temperature curves for the various heating rates. The linear dependences of ln β on $1/T_g$ for Al, Bi, C and N-GST using the dependence of T_g on the heating rate are shown in **Figure 4.8(a)**. The slopes of the linear dependences are equal to *E/R* according to the Moynihan plot.

From the linear slope of **Figure 4.8(b)** at $T = T_g$, the apparent activation energy (*E*) and the fragilities (*m*) were obtained and are depicted in **Figures 4.9(a)** and **(b)**, respectively. Pure GST has *m* = ~47, which indicates that it is relatively fragile. Compared to pure GST, *m* significantly decreases with C and N doping to *m* = ~20 for 10 at.% C and 10 at.% N GST, which indicates that they are relatively strong. However, Al and Bi-GST show negligible changes of *m*. A. L. Greer *et al.* recently reported that pure GST is fragile (*m* = ~90), which is highly mobile.[36] The significant decrease in *m* with C and N doping in this study indicates that the highly mobile nature of pure GST can be easily altered. However, Al and Bi doping has a negligible effect on the fragility. The inconsistencies between dopants can be attributed to the different structural changes associated with the different dopants, especially to the free volume of the amorphous GST.

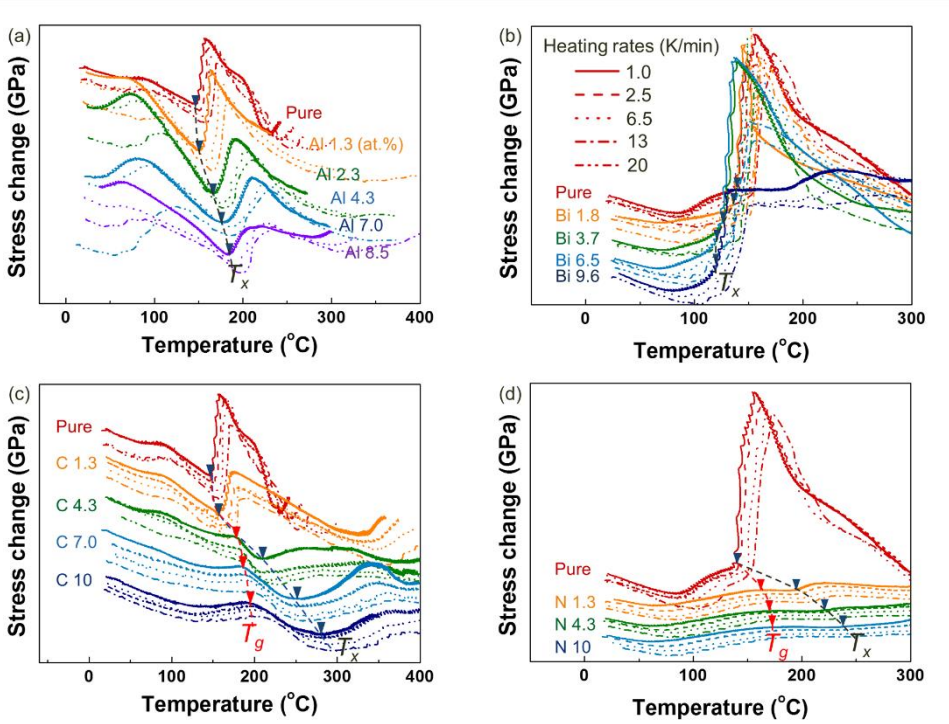

Figure 4.7 (a) Stress-temperature curves of (a) Al-doped, (b) Bi-doped, (c) C-doped, and (d) N-doped GST films during heating for different heating rates (from 1.0 to 20 K/min).

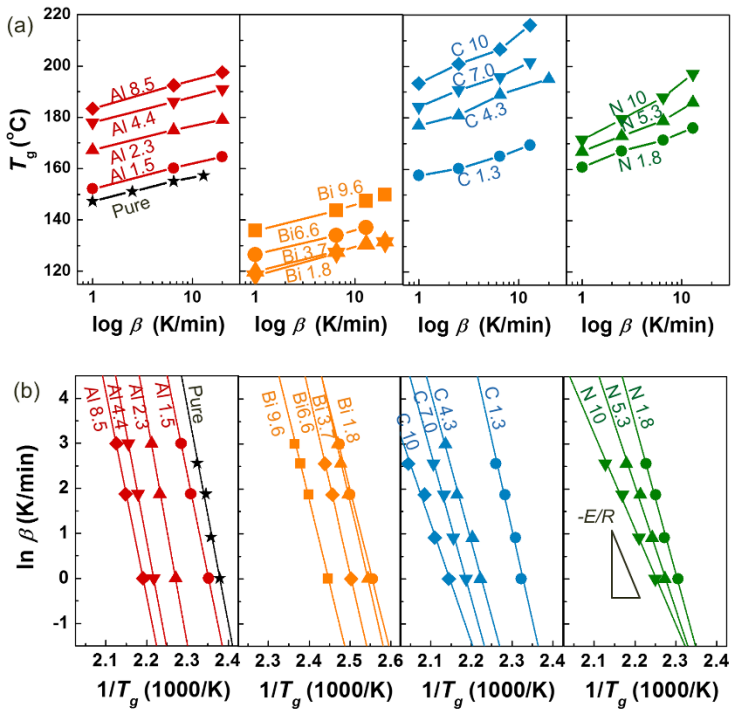

Figure 4.8 (a) Dependence of T_g on heating rates (β) and (b) linear dependences of ln β on 1/T_g for Al-, Bi-, C- and N-GST.

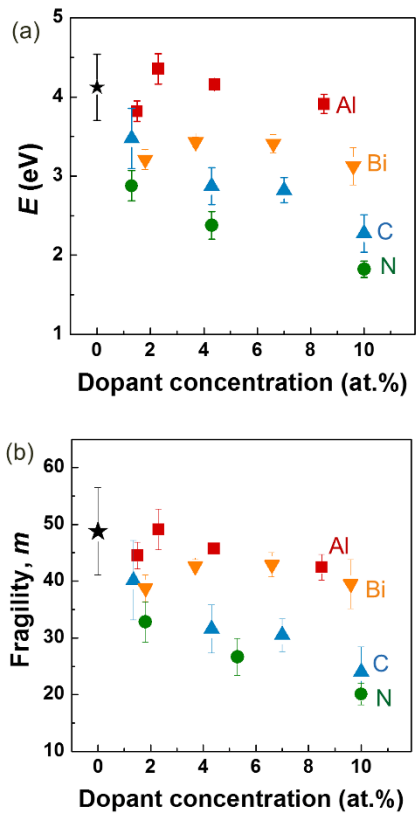

Figure 4.9 (a) Apparent activation energy and (b) fragility obtained from the linear slopes in Figure 4.8(b) at $T = T_g$ for pure and Al-, Bi-, C- and N-GST.

4.5.2. Vogel-Fulcher-Tammann extrapolation

The calculated values of E can be utilized to extrapolate the curves of viscosity as a function of temperature because it is important for predicting the crystallization kinetics at high temperatures (similar to the switching temperature of the PcRAM cell.)

To describe the temperature dependence of viscosity (η) or the relaxation time (τ) in a fragile liquid with non-Arrhenius behavior, the Vogel-Fulcher-Tammann equation generally best fits the experimental data of a super-cooled liquid with non-Arrhenius behavior:

$$\eta = \eta_0 \exp\left(\frac{DT_0}{T - T_0}\right) \tag{2.2}$$

where D and T_0 are fitting parameters. For the extrapolation, the obtained fragilities were used to define the linear slope of the logarithm of the viscosity as a function of T_g/T (known as the Angell plot) at T_g. For further extrapolation, $\eta = 10^{12}$ Pa-s ($\tau = 10^2$ s) at $T = T_g$ and $\eta = 10^{-4}$ (s) ($\tau = 10^{-14}$ s) at $T \sim \infty$ are assumed. Based on the Vogel-Fulcher-Tammann equation, the logarithm of the viscosity as a function of T_g/T for pure GST and Al 8.5 at.%, Bi 9.6 at.%, C 10 at.% and N 10% doped GST were obtained and are shown in **Figure 4.10**.

Figures 4.10(a) and **(b)** show the large deviations of pure, Al-GST and Bi-GST from Arrhenius behavior, which results in relatively rapid decreases in η and τ (rapid increases in atomic mobility) with temperature. **Figures 4.10(c)** and **(d)** show the smaller deviations of C-GST and N-GST from Arrhenius behavior, which results in gradual decreases in η and τ (gradual increases in atomic mobility) with temperature.

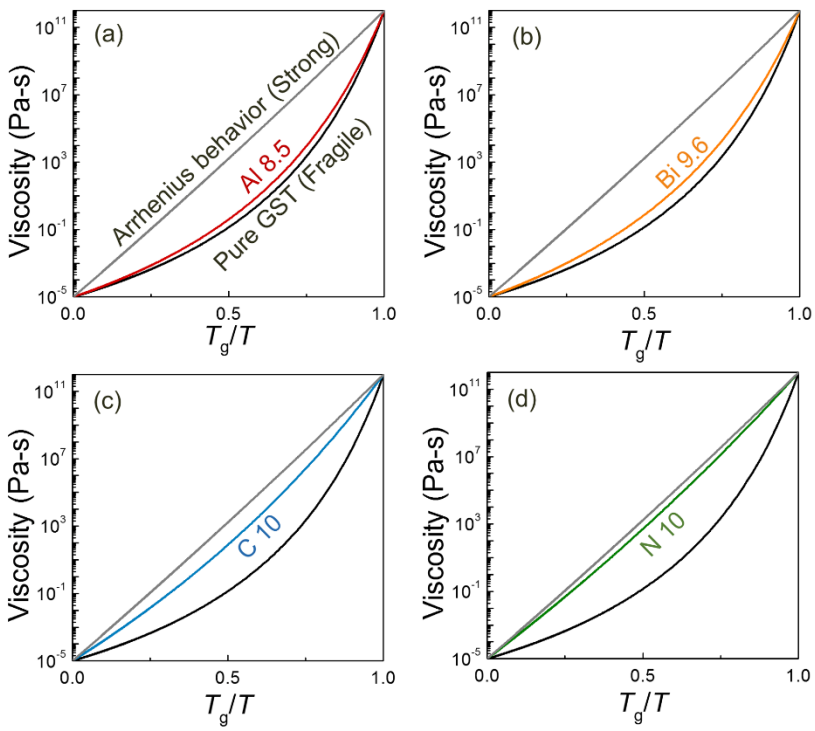

Figure 4.10 Extrapolated curves of the logarithm of the viscosity as a function of T_g/T according to the Vogel-Fulcher-Tammann relation for (a) Al 8.5 at.% GST, (b) Bi 9.6 at.% GST, (c) C 10 at.% GST and (d) N 10 at.% GST in comparison with pure GST and Arrhenius behavior.

Extrapolated curves of the logarithm of the viscosity as a function of temperature were also obtained for Al 8.5 at.%, Bi 9.6 at.%, C 10 at.% and N 10 at.% GST according to the Vogel-Fulcher-Tammann relation in comparison with pure GST and are depicted in **Figure 4.11(a)**. The T_g at which the viscosity is equal to 10^{12} Pa-s is denoted by arrows. T_g changes with doping, and these changes are associated with the bonding enthalpy as discussed in **Sec. 4.4.2.** This result is consistent with the model of the relationship between T_x - T_g and atomic mobility shown in **Figure 4.11(a)**.

The estimation of the crystallization growth rate is important in the prediction of the SET speed of PcRAM.. The crystallization growth rates (U_{growth}) were estimated using the relationship between the effective diffusivity D and η, which is known as the Stokes-Einstein relation (only valid at $T \geq T_m$) as follows:

$$D = \frac{kT}{3\pi a \eta} \tag{4.1}$$

$$U_{growth} = \frac{D}{a} \tag{4.2}$$

where a is a jump frequency that is usually determined from the effective atomic diameter ($d_{average} \sim 0.268$ nm for GST). U_{growth} were obtained from the viscosities of GST films in **Figure 4.11(b)** with various dopant concentrations at $T = 900$ K (the temperature where $T \geq T_m$) as shown in **Table 4.1**. U_{growth} significantly increases for C 10 at.% and N 10 at.% GST films, which indicates significant decreases in atomic mobility. However, in the cases of Al 8.5 at.% and Bi 9.6 at.% GST films, U_{growth} shows only slight increases, which allows higher atomic mobility at high temperatures.

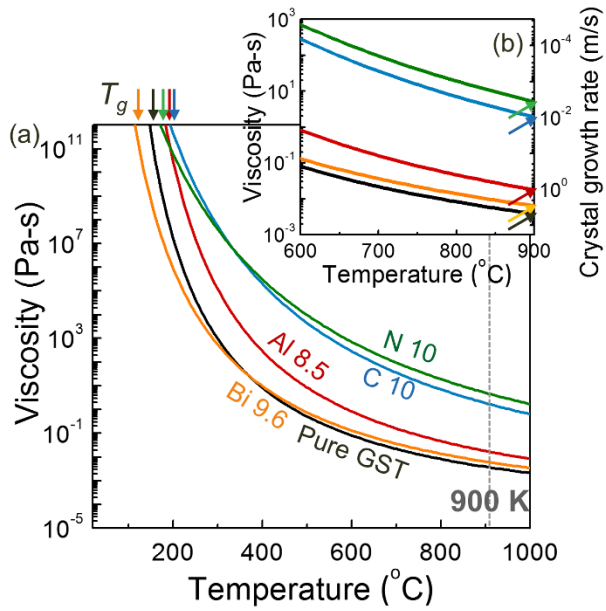

Figure 4.11 (a) Extrapolated curves of the logarithm of the viscosity as a function of the reciprocal of temperature according to the Vogel-Fulcher-Tammann relation for Al 8.5 at.%, Bi 9.6 at.% C 10 at.% and N 10 at.% GST (Arrhenius behavior) in comparison with pure GST. (b) Magnified view of (a).

Table 4.1 Crystallization growth rates (U_{growth}) obtained from the viscosities of $Ge_2Sb_2Te_5$ films with various dopant concentrations at T = 900 K.

	η_{900K} (Pa-s)	U_{growth} (m/s)
Pure	5.4×10^{-2}	3.4×10^{-1}
Al 8.5 at.%	5.0×10^{-1}	3.6×10^{-2}
Bi 9.6 at.%	9.0×10^{-2}	2.0×10^{-1}
C 10 at.%	1.6×10^{2}	1.2×10^{-4}
N 10 at.%	4.0×10^{2}	4.6×10^{-5}

4.6. Connection to device characteristics

The effects of doping on the crystallization behavior of GST were explored based on the experiments and the theoretical background. The results described above enabled the construction of 'treasure' maps of amorphous $Ge_2Sb_2Te_5$ doped with various doping elements, which is shown in **Figure 4.12**. **Figure 4.12(a)** shows a map of amorphous $Ge_2Sb_2Te_5$ tuned by various dopants as a function of the glass transition temperature (T_g) and fragility (m), while **Figure 4.12(b)** shows a map of amorphous $Ge_2Sb_2Te_5$ as a function of the glass transition temperature (T_g) and the super-cooled liquid region (T_x - T_g). The vertical axis describes the thermal stability (bonding enthalpy), and the horizontal axis describes the atomic mobility (free volume). In **Figure 4.12(b),** pure $Ge_2Sb_2Te_5$ is located in the left region but moves to the upper-right by C and N doping, to the upper-left by Al doping, and to the lower-left by Bi doping. The different effects of doping are related to the structural changes of amorphous $Ge_2Sb_2Te_5$, which depend upon the type of dopant. Both interstitial (C and N) and substitutional (Al and Bi) dopants change the bond enthalpies, which contribute to the thermal stability against crystallization. However, only interstitial dopants significantly change the portion of the free volume, which contributes to the atomic mobility of the system.

The characteristics of PcRAM are predicted using the underlying principle of structural stability based on T_g and T_x. As described above, a higher T_g can be regarded as a higher thermal stability against crystallization, which can achieve 10 yr data retention. In addition, the high atomic mobility above T_g can be regarded as the crystallization time, which is related to the SET speed. To compare the structural stability and PcRAM characteristics, **Figure 4.13** shows a map of PcRAM characteristics tuned by various dopings as a function of 10 yr data retention and SET time for different phase

change materials and dopants. The lines are obtained from the reported results of references[84-92]; if both the 10 yr data retention and the SET time were reported in same reference, they are marked as triangles, circles or squares. The pure phase change materials located in the lower-left region move to the upper-right by C and N doping or to the upper-left by Al doping. C and N (interstitial) doping in phase change materials generally increase 10 yr data retention but is disadvantageous for a low SET time. On the other hand, Al (substitutional) doping in phase change materials generally increases the 10 yr data retention while maintaining or even lowering the SET time, which is advantageous for reliability and performance. The comparison of PcRAM characteristics in **Figure 4.13** shows that the effects of doping on T_g and T_x - T_g successfully match the data retention and SET speed, respectively.

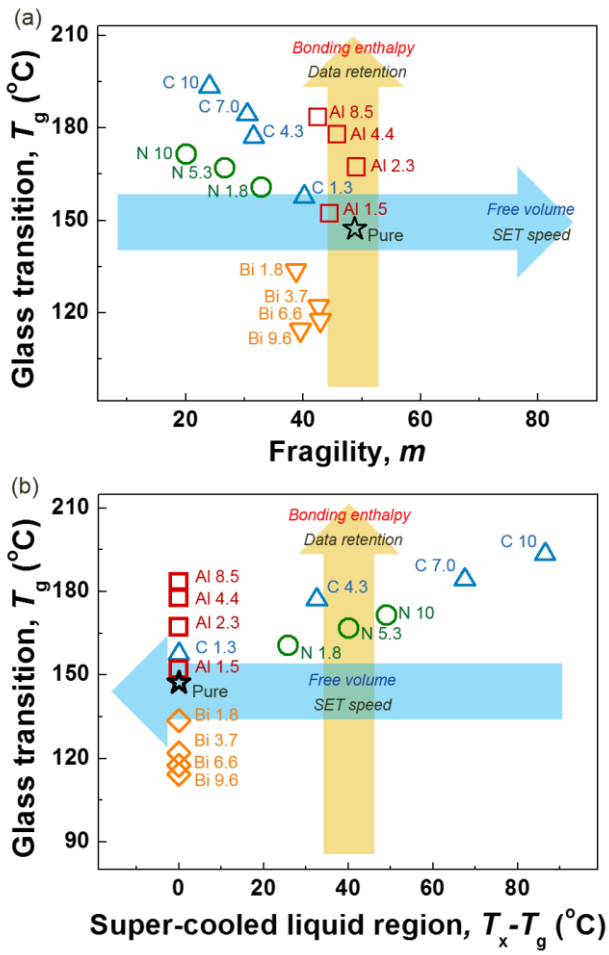

Figure 4.12 Maps of amorphous $Ge_2Sb_2Te_5$ tuned by various dopants as a function of (a) glass transition temperature (T_g) and fragility and (b) glass transition temperature (T_g) and the super-cooled liquid region (T_x - T_g). The vertical axis describes the thermal stability against crystallization (bonding enthalpy), and the horizontal axis describes the atomic mobility (free volume).

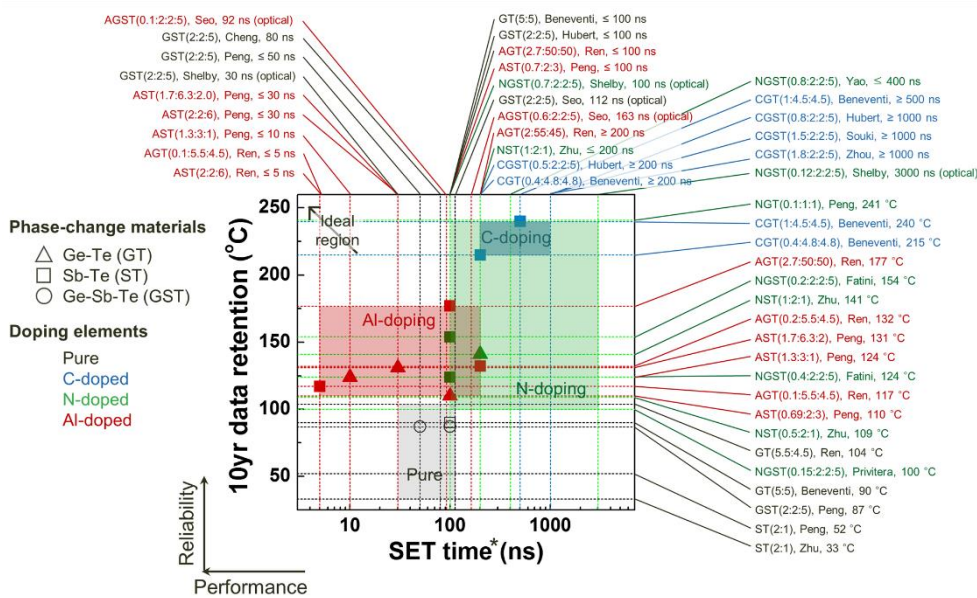

Figure 4.13 Map of PcRAM characteristics as a function of 10 yr data retention and SET time for various phase change materials and dopants[51, 52, 84-94] showing the successful match with Figure 4.12. The SET time* is determined for $R_{off}/R_{on} \sim 10^2$.

4.7. Summary

For a high switching speed and high stability of phase-change random access memory (PcRAM), we need to identify materials that enable rapid crystallization at elevated temperatures but are stable at and above room temperature. Achieving this goal requires a breakthrough in our understanding of the unique crystallization behavior of amorphous phase change materials. If crystallization was described by an Arrhenius behavior, we would only have to identify the activation barrier, which is a manageable task. For phase change materials, however, at the core of the crystallization kinetics is the unusual temperature dependence of the crystal growth velocity that is attributed to non-Arrhenius behavior. Therefore, the crystallization behavior can be predicted only if the non-Arrhenius crystallization kinetics are understood. Importantly, this unique behavior helps to develop phase change materials with high stability at low temperatures and rapid crystallization at higher temperatures because the crystallization kinetics at low and high temperatures are not linked by a strong relationship but are rather determined by different atomic mechanisms.

In this study, we observed the crystallization temperature (T_x), glass transition temperature (T_g), and super-cooled liquid region (T_x - T_g) of amorphous GST films using real-time mechanical stress analysis (the substrate curvature measurement with a multi-beam optical sensor). Interstitial (C, N) and substitutional doping (Bi, Al) were used to change the structural stability. C and N doping increase T_x, T_g and T_x - T_g, which is advantageous for thermal stability but is disadvantageous for atomic mobility. Al doping increases T_g and T_x while maintaining T_x - T_g, which is advantageous for both thermal stability and atomic mobility. Bi doping decreases T_g and T_x while maintaining T_x - T_g, which is disadvantageous for thermal stability but advantageous for atomic mobility.

From the heating rate dependence of T_g, the viscosity and fragility were also determined to describe the temperature dependence of atomic mobility in accordance with the Moynihan plot and the Vogel-Fulcher-Tammann relation. Similar to pure GST, large deviations from Arrhenius behavior are observed for Al- and Bi-GST, which likely lead to the high switching speeds at high temperatures.

The different effects of doping originate from the changes in the free volume and bonding enthalpy that are controlled by interstitial and substitutional doping. The effects of doping on the thermal stability against crystallization and atomic mobility match the desired effects of doping on data retention and SET speed, respectively. The results provide guidelines for the high performance and reliability of PcRAM.

CHAPTER 5

Effects of doping on elastic strain in crystalline Ge-Sb-Te

5.1. Introduction

The long-term instability issues of the characteristics of PcRAM are usually controlled by the inherently metastable nature of amorphous phase change materials; therefore, several studies have been devoted to controlling the structural stability of amorphous phase change materials. The most popular approach for amorphous stabilization is the doping of various elements, which was addressed in **Sec. 2.2.1**, because the stability of an amorphous phase change material can be improved by structural modification by doping. The effect of doping as an amorphous stabilizer is usually manifested in an increase in crystallization temperature or activation energy for crystallization obtained from electrical or optical analysis. However, to describe the exact roles of the dopants, the quantitative parameters need to be addressed by considering the kinetic and thermodynamic aspects based on a fundamental understanding of the structural stability of amorphous phase change materials.

Figure 5.1 shows a schematic plot of the Gibbs free energy and the logarithm of the viscosity as a function of time. As was discussed in **Sec. 2.1.3.**, viscosity decreases with increasing temperature and provides sufficient atomic mobility for crystallization at T_x. At the same time, the difference in Gibbs free energy between the amorphous and crystalline states (ΔG) decreases with increasing temperature. Because ΔG acts as the driving force for crystallization, a lower value of ΔG is disadvantageous for crystallization. In other words, crystallization relies on the competition between the driving force (thermodynamic factor) and the atomic mobility (kinetic factor). The study presented in Chapter 4, focused mainly on the kinetic stability of amorphous phase change materials. This chapter addresses thermodynamic stabilization induced by dopants that is related to the energy state of the amorphous state and the crystalline state of phase change materials.

To facilitate the discussion of the thermodynamic stabilization of amorphous structures by doping, it is useful to represent the energy landscape of amorphous materials with different configurational features. **Figure 5.2(a)** shows the landscape of the energy (E) as a function of the atomic configuration (Z^*). $E_{amorphous}$ is the energy of the amorphous state, and the nearby minima are intermediate amorphous states. $E_{crystalline}$ is the energy state of crystalline material, which has the lowest energy state. ΔE is the energy difference between the amorphous and crystalline states. The topology of the energy landscape is determined by the interplay between the configuration of the bond network and the energy required for atomic rearrangements, which is closely related to the fragility of the amorphous solids in the thermodynamic and kinetic factors.[32] This idea enables individual descriptions of thermodynamic and kinetic stabilization, which helps to characterize the exact role of dopants in amorphous phase change materials.

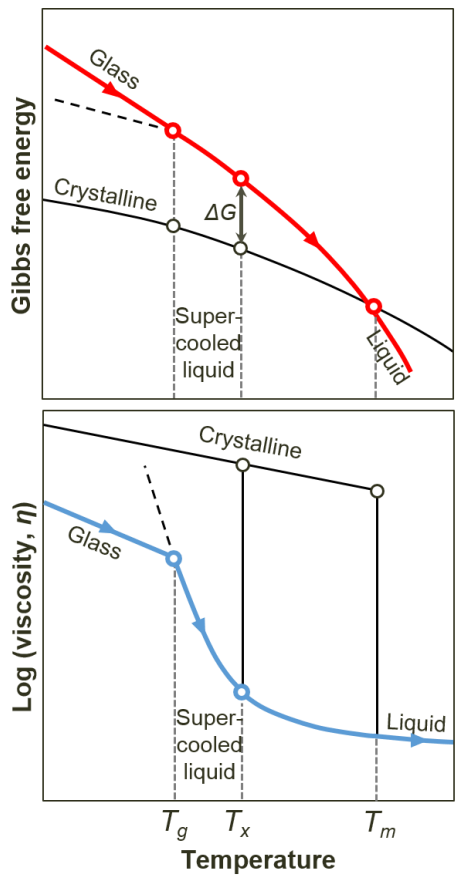

Figure 5.1 Schematic plot showing how crystallization relies on the competition between the driving force (thermodynamic factor) and the atomic mobility (kinetic factor).

The kinetic stabilization of amorphous materials is described by an increase in the energy barriers between intermediate minima in the energy landscape in **Figure 5.2(a)**. Increases in the energy barriers result in the restriction of atomic rearrangements in amorphous materials, which eventually leads to stabilization. The thermodynamic stabilization of amorphous materials is described by changes of the energy states of the amorphous and crystalline material that lead to a decrease in ΔE, which is related to the thermodynamic driving force for crystallization and includes 1) an increase in $E_{crystalline}$ and 2) a decrease in $E_{amorphous}$. This case includes the stabilization of the amorphous structure (decrease in $E_{amorphous}$) by decreasing E through the stabilization of amorphous GST by C-induced tetrahedral bonding[95, 96] or an increase in the disorder in amorphous GST by Al doping[55]. However, the destabilization of the crystalline structure (increase in $E_{crystalline}$) is also known to result in the relative stabilization of an amorphous structure by decreasing E with the N-induced strain field in the crystalline lattice of GST.[97, 98]

Figure 5.2(b) shows a schematic model of the thermodynamic destabilization of crystalline GST by a strain field in the crystalline lattice. If dopants are inserted in the crystalline lattice of GST, they distort the lattice, which produces a compressive strain field. This compressive strain field produces elastic strain energy in the crystalline GST films, which increases the energy state $E'_{crystalline}$ ($> E_{crystalline}$). As a result, the driving force for crystallization also decreases, and a relative stabilization of the amorphous state will be observed in the distorted crystalline GST.

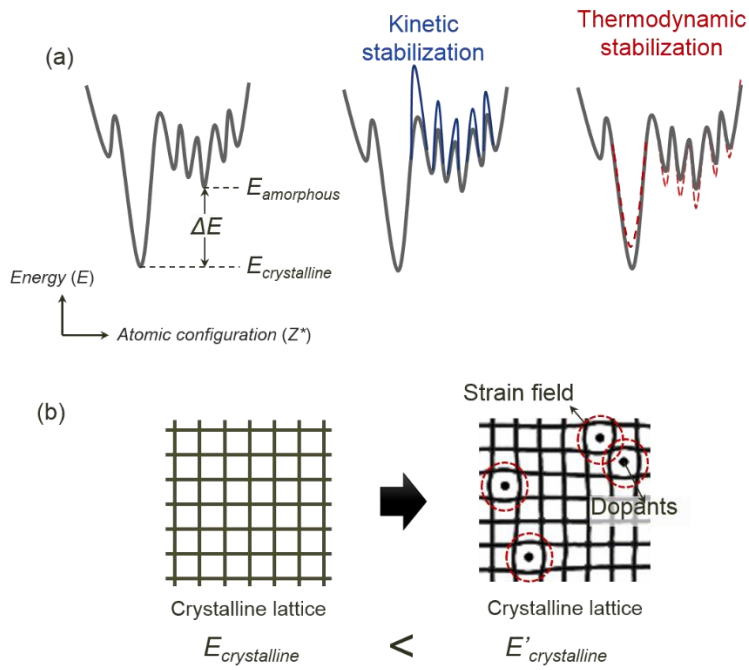

Figure 5.2 (a) The energy landscape showing energy (E) as a function of the atomic configuration (Z^*). $E_{amorphous}$ is the energy of the amorphous state, and the nearby minima are intermediate amorphous states. $E_{crystalline}$ is the energy state of crystalline state, which has the lowest energy state. ΔE is the energy difference between the amorphous and crystalline states. (b) Schematic of a distorted crystalline lattice in GST caused by a dopant-induced strain field.

However, no experimental evidence or quantitative properties have demonstrated how much the energy increases with a dopant-induced strain field (in terms of the elastic strain energy). In addition, the amount of elastic strain energy in the crystalline lattice would be significantly dominated by the structural features of the dopant and especially the atomic radii of the dopants. As shown in **Table 2.1**, interstitial dopants with C and N would have a greater impact on the elastic strain energy than substitutional dopants, including Al and Bi. Therefore, it would be interesting to verify the impact of dopants with various atomic radii on the elastic strain energy in the crystalline lattice, which affects the thermodynamic stabilization of amorphous GST. Achieving this goal requires experimental and theoretical investigations; the elastic strain energy is obtained by measuring the thickness changes associated with the crystallization of GST.

This study investigates the impact of doping-induced strain energy in the crystalline lattices of GST films by comparing the strain energies obtained from film-thickness changes associated with crystallization for interstitial (C and N) and substitutional (Al and Bi) dopants. The insight obtained will provide an explanation for the greater impact of C and N as an amorphous stabilizer.

5.2. Experiment

The as-deposited GST films were scraped off using a razor blade, and 50 to 60 mg powdered samples were prepared for the DSC measurements. GST thin films that were 300-nm-thick were prepared on 4-in-diameter glass substrates using DC magnetron sputtering at room temperature under the deposition conditions listed in **Table 3.1**. A differential scanning calorimeter (DSC, TA Instrument, DSC-Q1000) was utilized to

measure the difference in enthalpy between the amorphous and crystalline GST powder samples. The thicknesses of the thin film samples were observed using a field emission scanning electron microscope (FESEM, Carl Zeiss SUPRA 55VP) in the cross-sectional direction.

5.3. Effects of doping on thermodynamic stability

5.3.1. Enthalpy differences between amorphous and crystalline GST

The dopant-induced enthalpy difference between amorphous and crystalline GST was determined as follows:

$$\Delta H_{a\text{-}c,doping} = \Delta H_{a\text{-}c}(\text{doped}) - \Delta H_{a\text{-}c}(\text{pure}) \quad (5.1)$$

Figure 5.3(a) and **(b)** shows the DSC profiles of the C- and N-doped GST powders upon heating, respectively. Consistent with the effects of C and N on the crystallization temperature T_x in **Figure 4.5(a)**, which was measured through mechanical stress analysis in **Sec. 4.4.1.**, the exothermic peaks indicating T_x in **Figure 5.3(a)** and **(b)** increase with increasing C and N concentrations. The area under the heat flow during crystallization indicates the enthalpy difference between the amorphous and crystalline states ($\Delta H_{a\text{-}c}$). The $\Delta H_{a\text{-}c}$ of GST powders are broadened, and the area under the heat flow decreases with increasing C and N concentration as shown in **Figures 5.3(a)** and **(b)**. **Figures 5.3(c)** and **(d)** show the values of $\Delta H_{a\text{-}c}$ and $\Delta H_{a\text{-}c,doping}$ obtained from the area under the heat flow during crystallization in accordance with **Eq. (5.1)**. $\Delta H_{a\text{-}c}$ significantly decreases with C and N

doping of GST, which is likely due to the effect of C and N doping on the thermodynamic stabilization that was discussed in **Sec. 5.1.**

Two mechanisms for the decrease of $\Delta H_{a\text{-}c}$ by doping have been suggested by other researchers: i) the stabilization of the amorphous state by dopant-induced changes in the amorphous bonding networks, and ii) the destabilization of the crystalline state by the dopant-induced elastic strain field in the crystalline lattice. The enthalpy difference between the amorphous and crystalline states is controlled by these two effects. The enthalpy difference is important because it strongly affects the determination of the T_x point, which works as a driving force. Therefore, the doping-induced elastic strain energy is quantitatively investigated to verify the contribution of each effect to the changes in the enthalpy difference between the amorphous and crystalline states.

To investigate the exact role and quantify the effect of C and N on the energy state of amorphous GST, the elastic strain energy generated by doping was measured by measurements of the thickness changes.

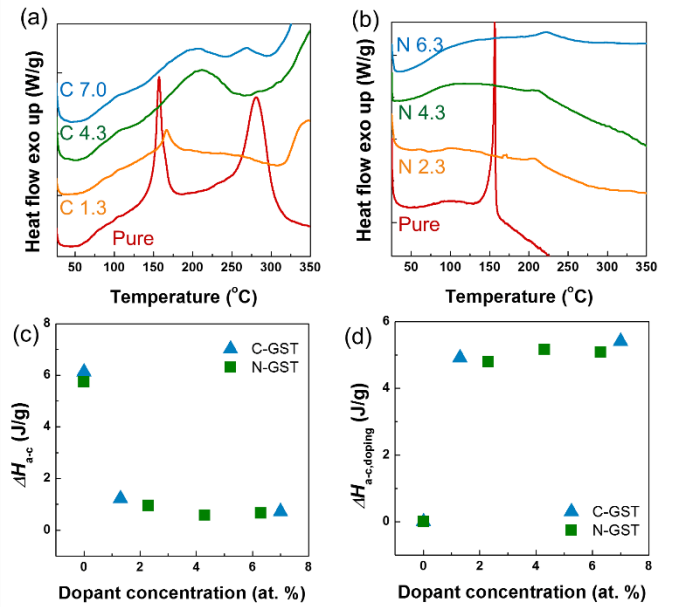

Figure 5.3 (a) DSC profiles of (a) C-doped GST and (b) N-doped GST. (c) Calculated enthalpy differences between amorphous and crystalline GST (=$\Delta H_{a\text{-}c}$) and (d) $\Delta H_{a\text{-}c,doping}$.

5.3.2. Elastic stain and stress induced by crystallization

The elastic stress $\Delta\sigma_{a\text{-}c}$ induced by crystallization in a film is expressed by the strain normal to the film based on following equation related to **Eq. (2.30)**.

$$\Delta\sigma_{a-c} = -Y_f \frac{1\text{-}\nu}{1+\nu}\varepsilon_{zz} \tag{5.2}$$

where Y_f is the biaxial modulus and is 54.9 GPa[99], and ν is Poisson's ratio and is 0.33[99]. In the calculations, the material properties described above were assumed to be same in the pure and doped GST films.[100]

As mentioned in **Sec. 2.1.2.**, the crystallization of the amorphous GST is accompanied by significant densification in the film. Because the amorphous GST film is attached to the substrate, changes in the horizontal dimensions are constrained. However, the thickness is not constrained and can be regarded as a change in the elastic strain (if the plastic deformation by Poisson's compression that accompanies horizontal changes is negligible.) Therefore, the normal strain obtained from the thickness change is:

$$\varepsilon_{zz} = \frac{h - h_0}{h_0} \tag{5.3}$$

where h is the thickness of the film after crystallization, and h_0 is the initial thickness of the film. This value can be utilized to determine the effect of doping on the elastic strain energy of amorphous GST. It will also help to verify the contribution of doping on the changes in enthalpy.

The decrease in ε_{zz} with dopant concentration can be explained as follows. The strain ε_{zz} is expected to be tensile (negative) because crystallization leads to densification and a decrease in thicknesses. However, when the interstitial dopant, such as C and N, distorts the crystalline lattice,[97, 98] a compressive strain field will be produced. As a result the tensile strain associated with crystallization will be compensated for.

Figure 5.4(a) shows cross-sectional FESEM images of as-deposited (left) and after crystallization (right) pure GST films. **Figure 5.4(b), (c)** and **(d)** show images of Al 2.3 at.%, C 1.3 at.% and N 1.3 at.% GST films, respectively. The crystallization of the samples were performed by annealing; the annealing temperatures were determined and are shown in **Figure 5.4**. The thickness changes associated with the crystallization were measured, and the strains in the normal direction (ε_{zz}) for the Al-, C- and N-doped GST films are obtained according to **Eq. (5.3)** and are shown in **Figure 5.4**.

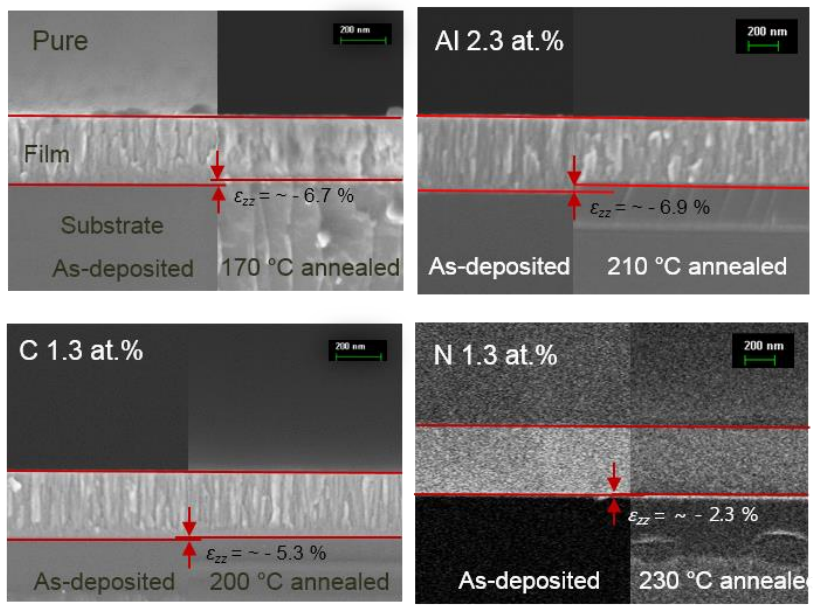

Figure 5.4 Cross-sectional FESEM images of (a) pure GST, (b) Al 2.3 at.% GST, (c) C 1.3 at.% GST, and (d) N 1.3 at.% GST before and after crystallization (the annealing temperatures are indicated in the images).

5.3.3. Elastic strain energy

Figure 5.5(a) shows the strain in the normal direction induced by crystallization in C-, N- and Al-GST. Interstitial doping (C, N) produces more compressive strain in the crystalline lattice than substitutional doping (Al). The strains associated with changes in film thickness after crystallization for C-doped and N-doped GST were utilized to calculate the dopant-induced elastic strain energy. The elastic strain energy (E_s) from thickness changes in film associated with crystallization was calculated using the following equation:

$$E_s\ (\mathrm{J/m^3}) = 0.5\ \sigma\varepsilon \tag{5.4}$$

By assuming elastic deformation, $\varepsilon = \sigma/Y$ is obtained according to Hooke's law in **Eq. (2.15)**,

$$E_s\ (\mathrm{J/m^3}) = \Delta\sigma_{a\text{-}c}{}^2 / Y_f, \text{ and } E_s\ (\mathrm{J/g}) = \Delta\sigma_{a\text{-}c}{}^2 / \rho \cdot Y_f, \tag{5.5}$$

where ρ is the density of the film and is 6.13 g/cm^3.[101]

The dopant-induced elastic strain energy was determined as follows:

$$\Delta E_{s,doping} = E_{strain}(\text{doped}) - E_{strain}(\text{pure}) \tag{5.6}$$

Values of $\Delta E_{strain,doping}$ were obtained and are shown in **Figure 5.5(b)**. The values of $\Delta E_{strain,doping}$ are ~ 9 (J/g) for C- and N-GST and ~ 5 (J/g) for Al-GST. Interstitial doping (C, N) produces more compressive strain in the crystalline lattice than substitutional

doping (Al). This effect is controlled by the structural features of the dopants. Interstitial dopants (C and N) distort the crystalline lattice and produce the elastic strain energy. In contrast, substitutional dopants (Al) have a small effect on the distortion of the crystalline lattice because they are located in atomic positions.

Because the values of $\Delta E_{s,doping}$ and $\Delta H_{a\text{-}c,doping}$ agree well with those of N-doped GST, the N-induced strain field in the crystalline lattice is likely to cause the enthalpy difference between the amorphous and crystalline states. In contrast, in C-doped GST, the stabilization of the amorphous phase by C-doping also has a significant effect on the enthalpy difference between the amorphous and crystalline states because the values of $\Delta E_{s,doping}$ are not similar to the values of $\Delta H_{a\text{-}c,doping}$.

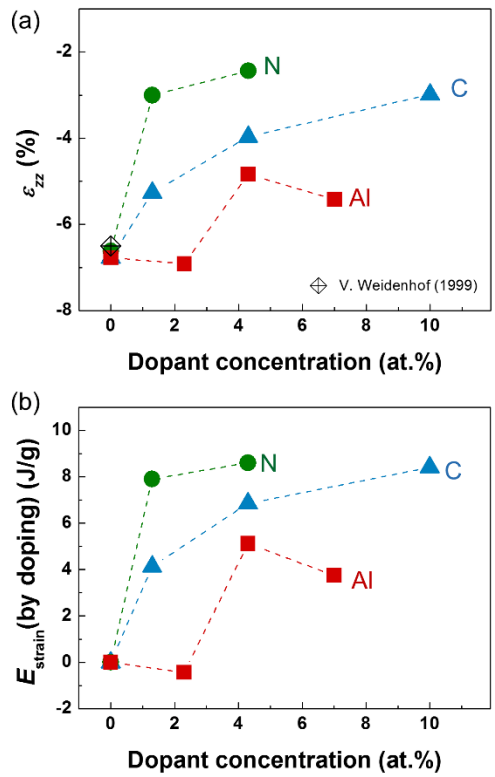

Figure 5.5 (a) Strain associated with changes in film thickness after crystallization for C-doped and N-doped GST. (b) Values of $\Delta E_{s,doping}$ and $\Delta H_{a\text{-}c,doping}$ for C-, N- and Al-GST.

5.4. Summary

In this chapter, C-, N- and Al-induced elastic strain and stress in crystalline lattices were investigated through measurements of the thickness in films associated with the crystallization process. The elastic stress induced by crystallization varies significantly with the doping elements and their concentrations; a large amount of compressive strain is produced in C- and N-doped GST, while Al doping has no significant effect on the stress change. This effect is strongly related to the structural features of the dopants. Interstitial dopants (C and N) distort the crystalline lattice and produce compressive stress and strain. Conversely, substitutional dopants (Al) have small effects on the distortion of the crystalline lattice. The elastic strain energy was calculated from the elastic stress and strain obtained from the thickness change in films. Compared to the enthalpy difference between amorphous and crystalline GST measured by DSC, the contributions of the dopants in producing strain were investigated. C- and N-induced strains have a dominant effect on the increase in $E_{crystalline}$. The instability of PcRAM can be evaluated using this methodology and can be developed further using material optimization. In addition, determining the exact role of the dopant can allow the successful selection of dopant for improving the reliability of PcRAM.

CHAPTER 6

Structural relaxation and resistance drift of amorphous Ge-Sb-Te

6.1. Introduction

The metastable nature of amorphous materials results in time-dependent properties due to their self-stabilization process, so called as structural relaxation as indicated in **Sec. 2.1.5.**.[16] Overall structural change with time occurs so that the materials can reach a more stable state and results in time-dependent electrical properties as well as mechanical stress.[10, 12] This feature surely affects the performance and the reliability of the devices, including the amorphous materials used in phase-change random access memory (PcRAM). PcRAM is a memory device that utilizes reversible amorphous-to-crystalline phase transitions to store information using the resistance difference between the phases of its component materials. With the development of PcRAM technology into a multi-level cell (MLC) storage devices, which has more than two intermediate resistance levels,[14] such devices have become more vulnerable to the instability of their amorphous phase, e.g., resistance drift.[14] Resistance drift, a steady increase in the

resistance of the amorphous state of phase-change materials according to a power-law relationship with time ($R/R_0 \sim t^{\nu}$),[10-13] results in the overlap of resistance between phases in **Figure 1.2(b)-(c)**.[14]

Defect annihilation model and strained bandgap model have been proposed to explain the origins of resistance drift.[10, 11, 15] According to the defect annihilation model,[11] the defects inside of the amorphous phase are reduced to reach a more stable state due to the metastable nature of amorphous phase-change materials as a self-stabilization process in amorphous GST as depicted in **Figure 6.1(a)**. Under the assumption of Poole-Frenkel conduction,[102] defect annihilation leads to an increase in inter-trap distance and the mobility edge, which results in an increase in resistance. According to the strained bandgap model,[10, 12] band broadening due to stress relaxation is the origin of resistance drift. In the real PcRAM, which is confined structure, compressive stress is applied to the amorphous phase-change material due to volume expansion when melt-quenching occurs. The compressive stress in the device results in a narrowing of the energy band gap for conduction. As the stress is relaxed against the compressive stress, the band gap is broadened and resistance increases with time as depicted in **Figure 6.1(b)**. The effect of the residual stress also could have been explained by theoretical model of pressure-induced subcritical nucleation leading to continuous increase of the resistance as depicted in **Figure 6.1(c)**.[103]

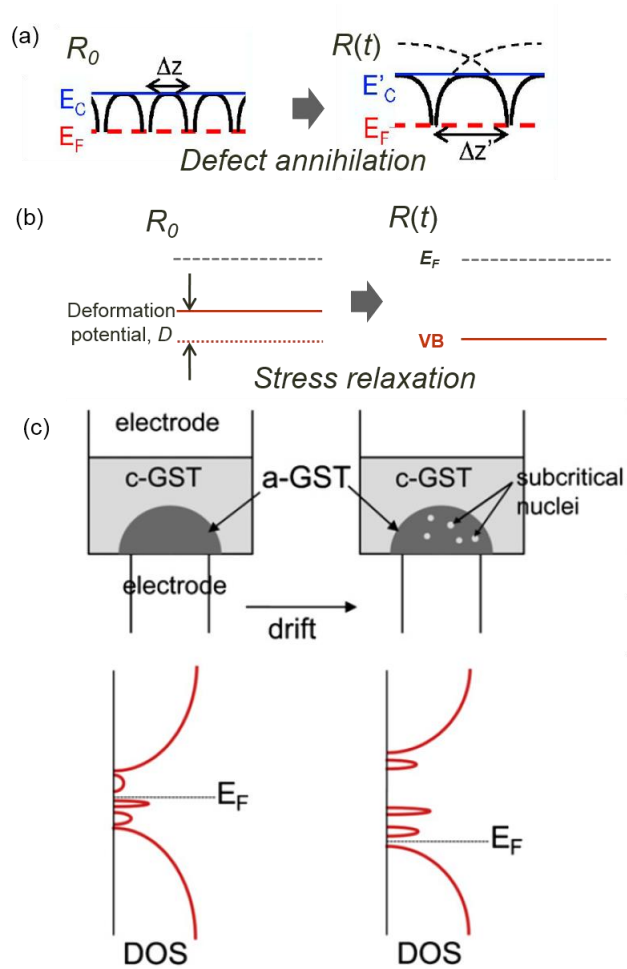

Figure 6.1 (a) Defect (dangling bonds) annihilation leads to reduction of localized state in Poole-Frenkel conduction. (b) Relaxation of compressive stress leads to bandgap broadening. (c) Pressure-induced subcritical nucleation leading to continuous increase of the resistance.

In this study, the effect of stress on the resistance drift over time was analyzed by using mechanical stress relaxation and electrical resistance measurements of amorphous (as-deposited) $Ge_2Sb_2Te_5$ (GST) thin films under the same sample conditions. The models that enable the time-dependent resistance change to be calculated from mechanical stress relaxation have been proposed and the calculated resistances were compared to the electrically measured data. To simulate the resistance change, the changes in the defect concentration were estimated by fitting the stress relaxation measurement to the bimolecular defect annihilation kinetics.[16] The changes in the strain were also extracted from the same fitting. The calculated defect concentration and strain were substituted into the given equations that describe the resistance drift according to each model. Finally, herein we suggest the origin of the resistance drift through the quantitative analysis of stress relaxation in amorphous GST.

6.2. Experiment

Un-passivated 300-nm-thick $Ge_2Sb_2Te_5$ (GST) films were used for this study. DC magnetron sputtering onto 300-μm-thick glass substrate of 2×2 cm at room temperature were used. The as-deposited films were prepared for amorphous processing. In order to investigate the effect of the stress relaxation on the resistance drift under highly controlled annealing temperature, real-time substrate curvature measurement was used. **Figure 6.2(a)** displays the schematic image of the real-time substrate curvature measurement for measuring mechanical stress and electrical resistance under the same condition. **Figure 6.2(b)** shows the viewgraph describing our unique approach to measure the electrical and mechanical properties of thin films in same time to provide the understanding of the correlation between electrical and kinetic (or mechanical) properties. This method utilizes the GST that is metal-wired in the edge to measure the electrical resistance while measuring the curvature of substrate by using multi-beam optic system. Variations in the mechanical stress of the thin film were determined by the substrate curvature measurement system using a multi-beam optic sensor technique at a vacuum level of 5×10^{-5} Torr. The changes in biaxial stress in thin film were determined from the changes in the curvature, according to Stoney equation in **Eq. (2.24)**. The stress relaxation was detected during isothermal annealing at 80 ℃. Electrical measurements were utilized to measure the resistance drift in the as-deposited GST films at a constant voltage of 0.1 V during isothermal annealing at 80 ℃ under the same heating conditions as the mechanical stress measurement.

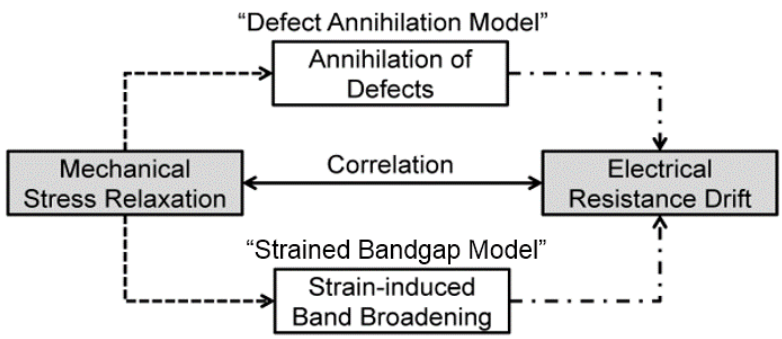

Figure 6.2 The viewgraph describing the approach to measure the electrical and mechanical properties of thin films in same time to provide the understanding of the correlation between electrical and kinetic (or mechanical) properties.

6.3. Stress relaxation and resistance drift

The normalized stress data in double linear scale is presented in **Figure 6.3(a)**. By using the stress data in the reference of J. Kalb[16] in **Figure 6.3(b)**, comparison of two stress data can be readily made. Regarding the mechanical stress relaxation data, initial stress (σ_0) was compressive stress amount of about 15 MPa and relaxation of compressive stress was observed as in the case of previous study.[16]

Figure 6.4 describes the resistance drift and stress relaxation of as-deposited GST during isothermal annealing at 80 ℃ on a log-log scale. The electrical resistance drift was observed to follow a power-law relationship with time ($R/R_0 \sim t^{\nu}$), which is depicted by the dashed line, the power-law exponent (ν) of which is observed to be 0.076. This exponent is observed to be in a similar range as values in real devices (0.03 ~ 0.1),[10] even though the sample is an as-deposited thin film structure. This result indicates that resistance drift also occurs in thin film structures.

This compressive stress differs greatly from that observed in real PcRAM cells, which is approximated to be 500 MPa,[103] though the power-law exponent for resistance drift is in a similar range as the exponents observed for real devices. **Figure 6.4** shows that the resistance drift and the stress relaxation exhibit quite different time-dependence. For the drift to be analyzed from the stress relaxation data, the adequate model is necessary in order to relate the stress and the resistance.

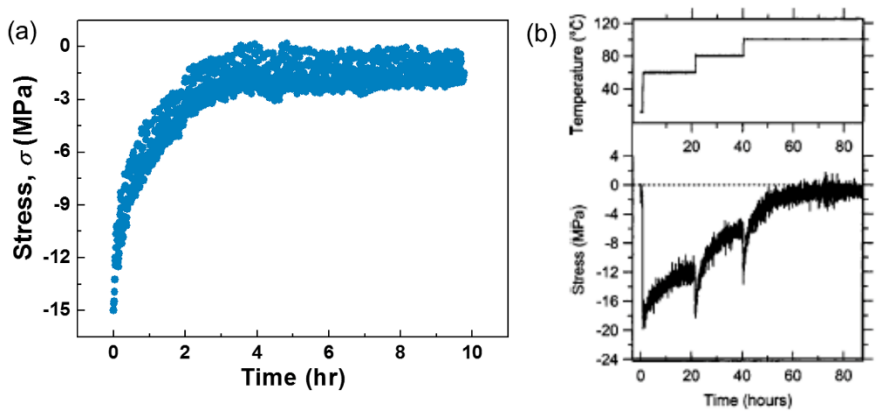

Figure 6.3 The normalized stress data (a) in this study (b) and in the reference of J. Kalb[16].

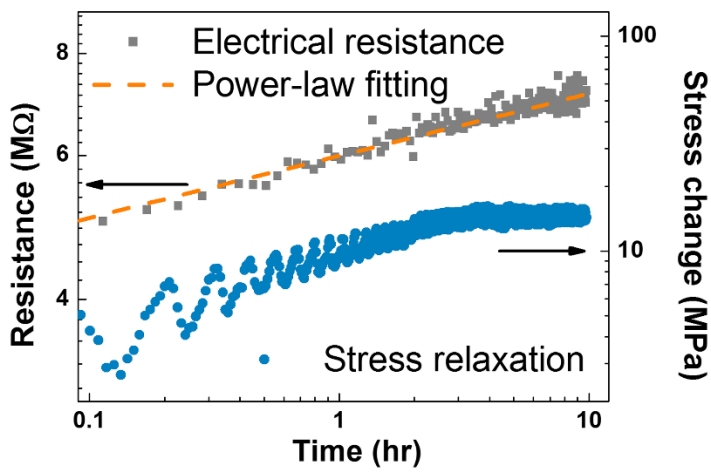

Figure 6.4 Power-law resistance drift (gray square) and relaxation of stress (black circle) in as-deposited GST during isothermal annealing at 80 ℃.

6.4. Defect annihilation model

6.4.1. Estimation of defect concentration

For the quantitative analysis of the origin of the resistance drift, the changes in resistance according to the defect annihilation model were calculated. The parameters required for the estimation, the defect concentration were obtained from the stress relaxation measurement. This unconventional approach; finding correlation between the electric properties and the mechanical stress is only possible due to the physical meaning of the viscosity in the glass. As discussed in **Sec. 2.1.3.**, the viscosity is defined as a resistance to flow and the defects are regarded as a center of the flow in atomic-scale. Thanks to its unique structural origin, the viscosity can describe the structural behaviors in glass (e.g. structural relaxation in **Sec. 2.1.5.**), besides, it can also describe the plastic deformation associated with the mechanical stress (explained in **Sec. 2.3.4.**) First, the quantification of defect concentration using the stress relaxation is as follows. According to the study on the structural relaxation in glass,[16] amorphous GST exhibits 'bimolecular defect annihilation kinetics', which gives the following relation between the stress and the viscosity as follows[16]:

$$\ln\left(\frac{\sigma(t)}{\sigma_0}\right) = -\frac{Y_f}{6\eta}t \tag{2.37}$$

$$\ln\left(\frac{\sigma(t)}{\sigma_0}\right) = -\frac{Y_f}{6k}\ln\left(1+\frac{k}{\eta_0}t\right) \tag{2.38a}$$

$$\ln\left(\frac{\sigma(t)}{\sigma_0}\right) = -\frac{Y_f}{6k_r\eta_0}(1-\exp(-k_r t)) \qquad (2.38b)$$

where σ is the stress in the film, k, k_r and η_0 are fitting parameters. Y_f is the biaxial modulus of amorphous GST, which has been determined to be 29.5 GPa by measuring the stress–temperature behavior in the elastic deformation region of two different substrates.[104] Because the wafer curvature measurement only provides the changes in stress, the initial stress σ_0 is determined from the entire amount of stress relaxation, -15 MPa, which is compressive stress. Based on **Eq. (2.37)**, **Eq. (2.38a)** and **Eq. (2.38b)** stress relaxation was fitted well to the bimolecular defect annihilation kinetics as seen in **Figure 6.5(a)** and less matched to the no annihilation and unimolecular defect annihilation model. By using these fitting parameters, we obtained the relevant time-dependent changes of viscosity as depicted in **Figure 6.5(b)**.

The bimolecular defect annihilation kinetics describe the situation in which two defects are combined and ultimately disappear. The annihilation of two dangling bonds leads to the relaxation of stress in the amorphous covalent system according to the works of F. Spaepen[105] who has studied the behaviors and properties of amorphous materials. The defect annihilation results in an increases in the viscosity of amorphous GST according to the **Eq. (2.11)**. Where n_f is the defect concentration and $n_{f,0}$ is the initial defect concentration before annihilation. According to the bimolecular defect annihilation fitting shown in **Figure 6.5(a)**, the normalized defect concentration was estimated as shown in **Figure 6.5(c)**.

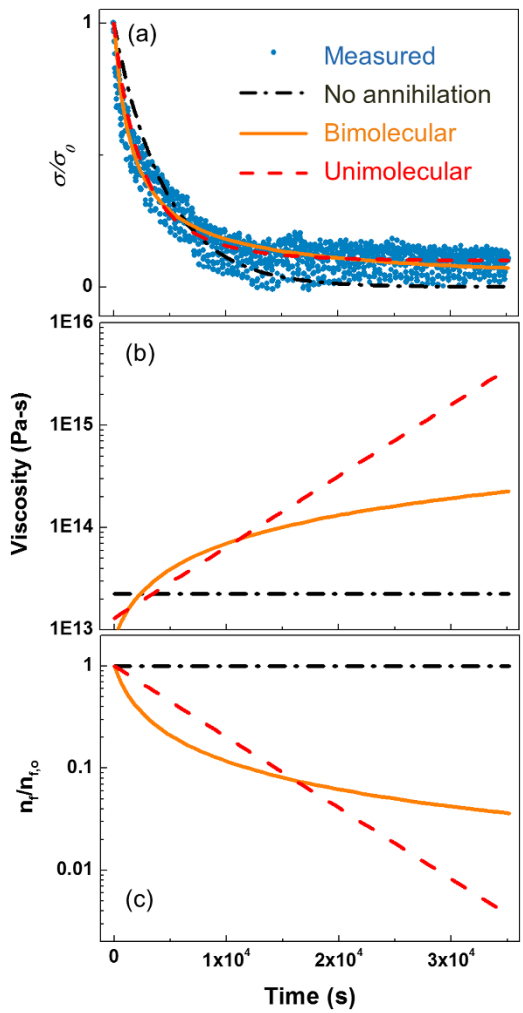

Figure 6.5 (a) Fitting of stress relaxation. (b) Viscosity and (c) normalized defect concentration as a function of time during isothermal annealing at 80 ℃.

6.4.2. Resistance modeling by Poole-Frenkel model

The normalized defect concentration was translated into the calculated resistance change by modeling the increase in the mobility edge under Poole-Frenkel conduction. The reported resistance of amorphous GST in general cases obeys the Arrhenius law given by $R = B \cdot \exp(E_A / k_B T)$,[10, 11] and with constant B assumed to be time-independent the following expression is easily obtained :

$$\ln \frac{R(t)}{R_0} = \frac{E_A'(t) - E_A}{k_B T} = \frac{\Delta E_A(t)}{k_B T} \tag{6.1}$$

where the $\Delta E_A(t)$ is change in the energy barrier for conduction during the resistance drift, R_0 is the initial resistance, and $R(t)$ is the drifted resistance. k_B and T are the Boltzmann constant and temperature, respectively. **Eq. (6.1)** is modified to express the defect annihilation model under the assumption of Poole-Frenkel conduction. The ΔE_A(t) is expressed as $\Delta E_A(t) = (\alpha q^2 / \pi\varepsilon) \cdot (\Delta z^{-1} - \Delta z'^{-1})$,[11] where α and β are correction terms determined from previous work,[11] q is 1.6 × 10^{-19} C, and ε is the dielectric constant of amorphous GST, 1.5 × 10^{-10} F/m.[106] The initial distance between defects, Δz is expressed as $\Delta z = \beta n_{f,0}^{-\frac{1}{3}}$,[11] and this increases to $\Delta z' = \beta n_f^{-\frac{1}{3}}$ as the defect annihilation occurs. Therefore, when n_f is assumed to be time-dependent, ΔE_A is time-dependent, while other parameters were considered to be time-independent. Therefore, **Eq. (6.2)** is taken from the substitution of ΔE_A into **Eq. (6.1)**:

$$\ln \frac{R(t)}{R_0} = \frac{\alpha q^2}{\pi \beta \varepsilon} \frac{n_{f,0}^{\frac{1}{3}}}{k_B T} \left(1 - \left(\frac{n_f(t)}{n_{f,0}} \right)^{\frac{1}{3}} \right) \quad (6.2)$$

The resistance drift was then modeled according to **Eq. (6.2)** as the lines in **Figure 6.7**, where the $n_{f,0}$ is fitting parameter. For the calculation, the defect concentrations in **Figure 6.5(c)** were substituted into **Eq. (6.2)**. Then the measured resistance, the same the data in **Figure 6.4**, was used for comparison. In **Figure 6.7**, the bimolecular defect annihilation model matches quite well with the measured resistance when $n_{f,0}$ is 2.5×10^{21} m^{-3}.

It should be noted that the physical meaning initial defect concentration of 2.5×10^{21} m^{-3} is controversial because of its small value. Considering the volumetric dimension of PcRAM cell (e.g. 2.5×10^4 nm^3),[107] total number of defect would be 6.25×10^{-2}, which is not feasible. This inconsistency is likely originated from the ambiguous concept of the defect in amorphous materials. The defects are known as unoccupied bond which acts as a center of structural relaxation and localized states of Poole-Frenkel conduction. However, the defects are more likely not only unoccupied bond (positively charged or negatively charged), but also distorted bond angles or free volumes. These various types of defect differently affect the structural relaxation and the time-dependent resistance, resulting in the large deviation of the defect concentration.

6.5. Strained bandgap model

For the estimation of resistance drift according to the strained bandgap model, the change in biaxial strain was obtained from the stress relaxation fitted with **Eq. (5)**, as depicted in **Figure 6.7**. The biaxial strain was obtained from the biaxial stress-strain relation regarding Hooke's law in **Eq. (2.15)** as follows. In **Figure 6.6**, because the strain calculated from the measured stress data is well matched with the strain obtained from the bimolecular fitting of stress, the latter was used for further calculations. It should be noted that the use of bimolecular fitting was only for the demonstration, not for borrowing the theory of the bimolecular defect annihilation kinetics. The modeling of band gap broadening by the strain can be achieved by using the concept of the deformation potential, $dE_A / du = D$.[10] The substitution of this relation into **Eq. (6.1)** derives the resistance change according to the strained bandgap model as follows:

$$\ln \frac{R(t)}{R_0} = \frac{Du(t)}{k_B T} = \frac{2D\Delta\varepsilon(t)}{k_B T} \tag{6.3}$$

This equation is modified from previous work regarding the strained bandgap model,[10, 12] where the deformation potential D is reported to be 1 ~ 3 eV,[10] and u is the dilation, which is assumed to be $u \approx 2\Delta\varepsilon$ for the thin film system in this study.

The calculation of resistance change according to the stained bandgap model is depicted using **Eq. (6.3)** as indicated by the dashed line in **Figure 6.7**. The change in strain in **Figure 6.6** is substituted into **Eq. (6.3)** to model the stress relaxation. As in the defect annihilation model, a comparison with the electrically measured data was carried out in **Figure 6.7.** While the resistance calculated from the defect annihilation

model shows a strong correlation with the measured data, the strained bandgap model produces resistance saturation, which is not consistent with the electrically measured data; moreover, the model produces a deformation potential of ~ 5 eV , which does not match the reported range of 1 ~ 3 eV. Such a result indicates that the resistance drift in amorphous GST can be modeled more accurately according to defect annihilation rather than stress relaxation.

The insight obtained above shows that the defect annihilation due to structural relaxation explains the resistance drift better; structural stability is dominant factor in the view of mechanical stress relaxation. Therefore, in order to enhance the structural stability of GST film and retard the resistance drift phenomenon, the resistance drift of N-doped GST film was measured using same measurement system in same condition. **Figure 6.8(a)** and **(b)** shows power-law resistance drift and normalized resistance drift as a function of time of as-deposited pure GST and N-GST film during isothermal annealing at 80 ℃, respectively. N doping (N 10 at.%) decreases power-law exponent from 0.076 to 0.051, which is slight changes. N-induced structural stabilization below T_g is not significant compared to the case of above T_g as observed in Chapter 4, since the liquid-like structure of the super-cooled liquid will more be sensitive to free volume, which is occupied by interstitial dopant such as N. The solid-like structure of the glass would less be affected by the occupation of the free volume by doping.

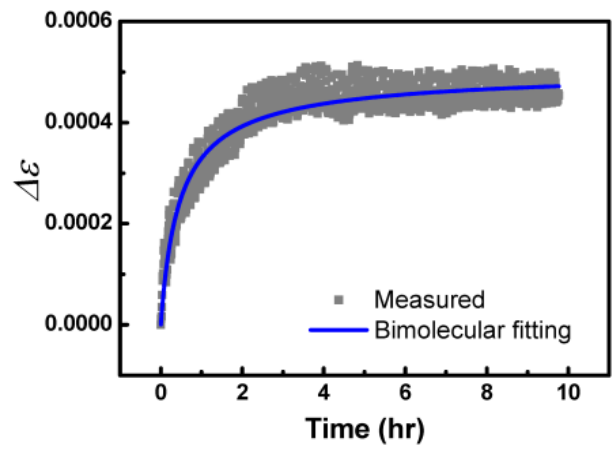

Figure 6.6 The change in biaxial strain calculated from the stress data of as-deposited GST during isothermal annealing at 80 ℃.

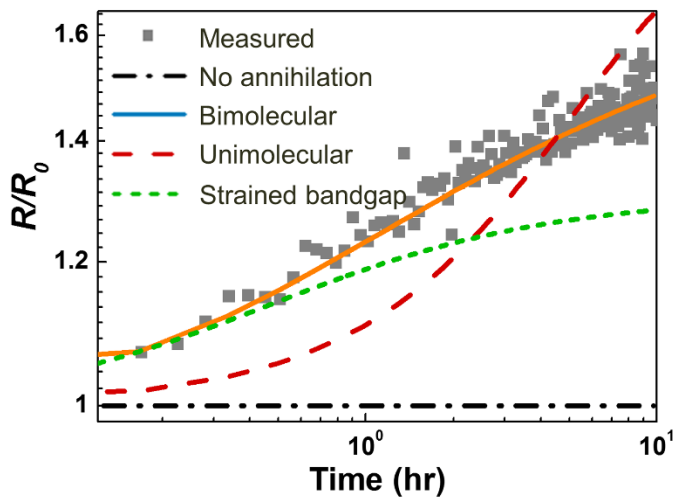

Figure 6.7 Resistance drift estimated using two different models described in **Eq. (6.2)** and **Eq. (6.3)**, respectively. The electrically measured resistance drift data are shown for comparison, which means that the defect annihilation due to structural relaxation explains the resistance drift: structural stability is dominant factor.

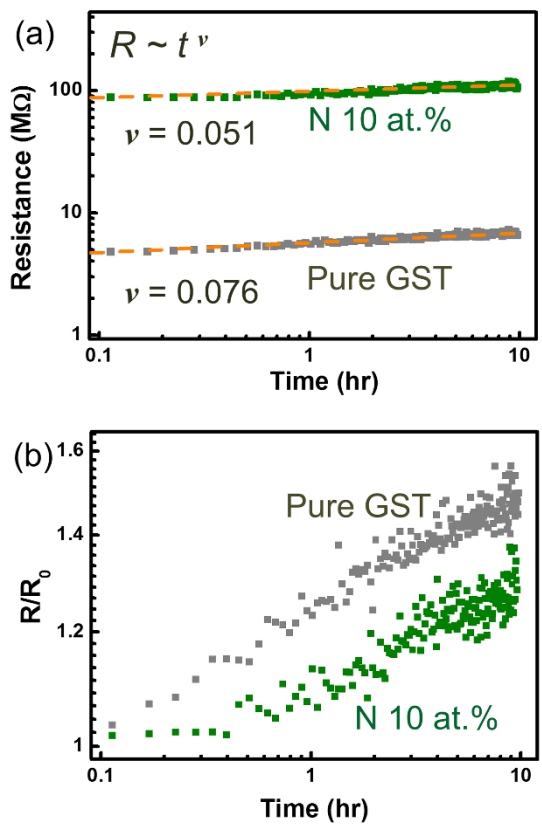

Figure 6.8 (a) Power-law resistance drift and (b) normalized resistance drift as a function of time of as-deposited pure GST and N-GST film during isothermal annealing at 80 ℃. N doping (N 10 at.%) decreases power-law exponent from 0.076 to 0.051, which is slight changes.

6.6. Summary

In this Chapter, power-law resistance drift was observed in the isothermal annealing of as-deposited GST at 80 ℃, with a power-law exponent, which falls in a similar ranges as that observed in conventional PcRAM devices.[5] The stress relaxation was measured under the same sample conditions and the same heating history using resistance drift measurements. The stress relaxation data of amorphous GST were fitted with bimolecular defect annihilation kinetics to extract the parameters required to model the temporal resistance drift. The resistance change estimated from the defect annihilation model matched well with the electrically measured data, while the strained bandgap model exhibited a large deviation. In conclusion, defect annihilation due to the metastable nature of amorphous GST better explains the drift phenomena than band-gap broadening due to stress relaxation based on the quantitative results. Our results suggest that the resistance drift of PcRAM can be minimized by selecting a stable glass as a phase-change material rather than used in the optimized design of PcRAM devices to reduce the compressive stress. Furthermore, we carried out the thin film structure test method to enable the quantitative analysis, which is impossible to be conducted in the device level due to the small scale of the devices, which feature a complex and confined structure.

CHAPTER 7

Effects of surface on glass transition of amorphous In-Ga-Zn-O for thin film transistor

7.1. Introduction

The use of amorphous materials as key functional materials in various electronic devices continues to increase because they exhibit superior flexibility, adequate processability and reasonable performance. However, because the amorphous phase is metastable structure compared with the crystalline phase, its properties may drift over time and cause instability when applied in devices. Therefore, an understanding of the structural stability of amorphous materials is a key step in the fabrication of stable electronic devices. However, there is limited understanding of structural stability, especially with regard to amorphous thin-films for device application.

Amorphous In-Ga-Zn-O (a-IGZO) has been actively employed in electronic applications due to its high electron mobility and high stability of amorphous structure as addressed in theoretical background of **Sec. 2.2.2.**[17] However, if a-IGZO is utilized as a thin film structure in electronic applications, high structural stability of a-IGZO can be

hindered by the effect of high surface-to-volume ratio. As thinner the film, higher the surface-to-volume ratio in film, therefore effect of the surface instability will be more significant: unconstrained bonds in surface are reported to be in high mobility of atoms,[64] and distinct coordination distributions in surface of amorphous Al_2O_3 films affect the structural stability.[78] Besides, the effects of ambient gas on the surface-reaction of oxide thin film have been also investigated.[108, 109]

Unfortunately, the structural stabilities of a-IGZO films remain unclear due to the difficulties encountered in experimental quantification. Because the structural changes in the amorphous film (e.g. the glass transition, the crystallization and the structural relaxation etc.) are determined by multiple mechanisms, which change based on temperature and deposition conditions, the identification of proper quantitative parameters for a stable amorphous phase is challenging.

In this study, we employed a mechanical analysis that uses wafer curvature measurements to monitor the phase and structural changes of amorphous films. Small changes in the volume of the film causes substantial changes in the curvature of the film/substrate system[24]. If the change in the volume of 0.015 % in the film produces a change in thickness of ~0.005 %, a stress change of ~5 MPa simultaneously occurs (elastic behavior is assumed) in a detectable range (> ~1 MPa for 50-nm-thick film/100-μm-thick Si wafer) using our mechanical analysis. This range is better than the detectable range for conventional ellipsometry. We can measure T_g and the fragility to obtain the instability that originates from the surface layer. The structural relaxation of glass at temperatures below T_g is also identified. These results comprise the first report on these parameters and the mechanisms of this material system.

7.2. Experiment

As mentioned in **Sec. 3.1.**, amorphous $In_{25}Ga_{44}Zn_{31}O_x$ films with various thicknesses (20-300 nm) were deposited on Si wafers using RF magnetron sputtering at room temperature . The RF power and the chamber pressure were 50 W and 5 mTorr, respectively. The gas mixing ratio was Ar/O_2 = 99/1. The phase of the as-deposited IGZO film was amorphous, as confirmed by grazing incident X-ray diffraction (GIXRD, New D8 Advance). The substrate curvature measurement system with multi-beam optic sensor was used (kSA Multibeam Optic System) as depicted in **Figure 3.3** to determine the mechanical biaxial stress in the film during thermal cycling (room temperature ~ 640 ℃) in the N_2 atmosphere at 10 Torr. The biaxial stress (σ) was determined from the curvature according to Stoney equation in **Eq. (2.24)**. The thicknesses and densities of the films were determined using X-ray reflectivity (X'pert-Pro, Philips Inc.)

7.3. Effect of surface on glass transition

7.3.1. Stress evolution during heat cycling

Figure 7.1 displays the stress change as a function of temperature curve for a-IGZO films with various thicknesses of 20 nm. The positive stress and negative stress indicate the tensile direction and compressive direction, respectively, of the film stresses. When the temperature increases to ~80 ℃, the stress evolves toward the compressive direction because the a-IGZO film has a larger coefficient of thermal expansion (CTE) than the Si wafer. The CTE of a-IGZO film was measured as 5.23 ppm/K, whereas the CTE of

Si was 2.61 ppm/K. The CTE of a-IGZO could be determined by the fitting of linear slope in stress-temperature curve during cooling in accordance with **Eq. (2.26)**. The biaxial modulus of film assumed to be 214 GPa for a-IZO,[110] α_s is CTE of Si substrate, 2.61 ppm/K. α_f is the CTE of a-IGZO film, obtained as 5.23 ppm/K. Large deviation with the CTE in other paper of 16.0 ppm/K[23] is may due to they used normal direction. For 80-400 ℃, the stress changed toward the tensile direction, which indicates that volume shrinkage occurred. This change is associated with the structural relaxation of glass; we denote the temperature at which the relaxation occurred by T_{relax}.

After heating above 400 - 550 ℃, another change in the stress toward the compressive stress direction was observed. This change is related to the glass transition: the glass state transforms into a super-cooled liquid state while its volume gradually expands (T_g). Interestingly, a glass transition was observed at two separate temperatures: $T_{g,1}$ and $T_{g,2}$ as observed in **Figure 7.1(b)** (the magnified view of stress change-temperature curve for various heating rates). At approximately 630 ℃, the stress sharply changed toward the tensile direction, and it indicates that the volume decreased by the crystallization, making this temperature T_x.

7.3.2. Thickness dependence of structural changes

Figure 7.2 shows the $T_{g,1}$ distinctly dependent on the thickness of the film, whereas $T_{g,2}$ and T_x is invariant with the thickness. The $T_{g,1}$ approaches $T_{g,2}$ as the film thickness increases, finally the $T_{g,1}$ and $T_{g,2}$ merged to one value (~557 ℃) at 300 nm. **Figure 7.3** indicates the values of T_x, $T_{g,1}$, and $T_{g,2}$ determined from the **Figure 7.2.** The clear thickness dependence of $T_{g,1}$ is due to the structural instability that originates from the surface layer, whereas no thickness dependence is shown in T_x.

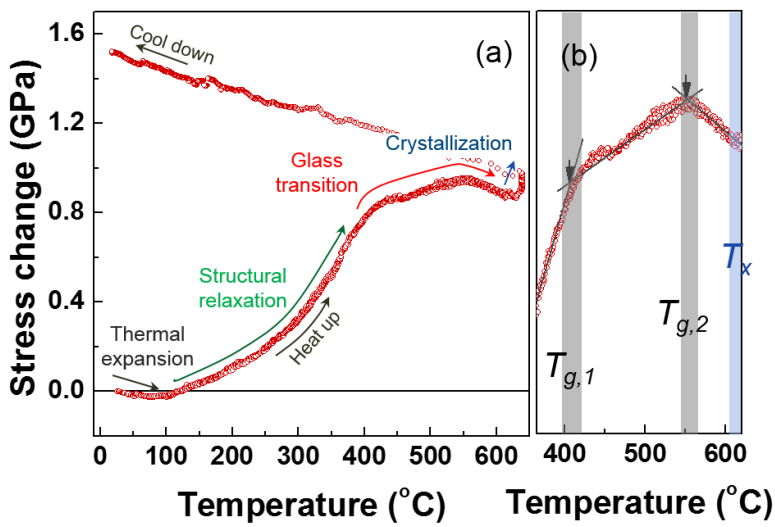

Figure 7.1 (a) Stress change-temperature curves and (b) Changes near T_g and T_x of a-IGZO films with 20 nm-thick for heating rate of 1.0 ℃/min.

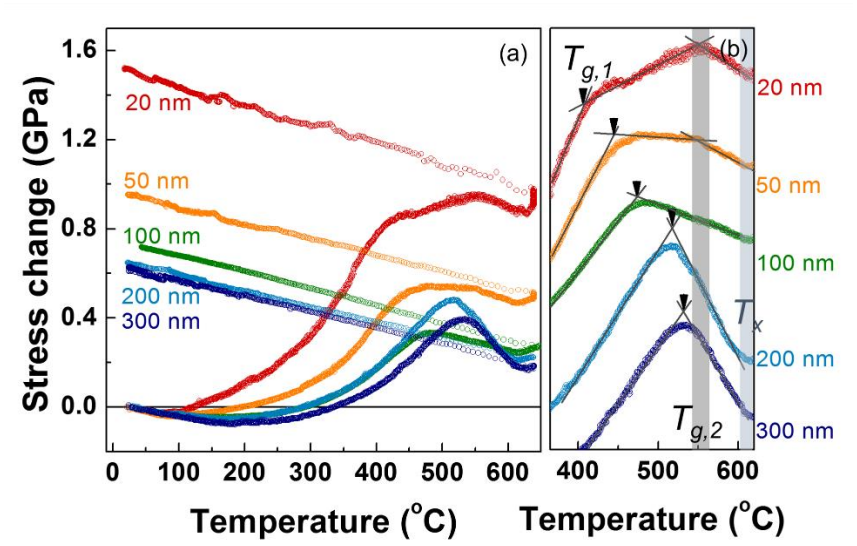

Figure 7.2 (a) Stress change-temperature curves and (b) Changes near T_g and T_x of a-IGZO films with various film thickness (from 20 nm to 300 nm) for heating rate of 1.0 ℃/min.

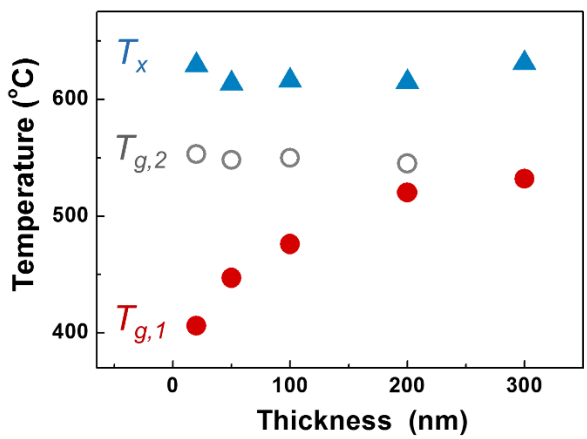

Figure 7.3 Thickness dependence of crystallization temperature and separated glass transition temperatures for heating rates of 1.0 ℃/min.

The separation of T_g in thinner films indicates the significant effect of the surface layer because the surface-to-volume ratio is larger for thinner films. If the surface layers exhibit different properties, such as different values of T_g compared with the bulk, a separated T_g will result. Accordingly, the separation of T_g in thinner films in **Figure 7.1** was caused by the surface layer; this layer has a relatively lower T_g compared to the bulk due to its structural instability. **Figure 7.4** displays the schematic that describes the separation of T_g, which is called as two layer model. If the surface layer exhibits different value of T_g ($T_{g,suface}$) than the T_g of bulk region ($T_{g,bulk}$) due to the instability originating from surface, separated volume expansion points will result. As the film thickness increases, the $T_{g,surface}$ of surface layer (red dashed line) approaches the bulk region (blue solid line) as the surface-to-volume ratio lowers with increasing thickness. Therefore, for a-IGZO film, the T_g of the surface layer is $T_{g,1}$ and is represented as $T_{g,surface}$; the T_g of the bulk region is $T_{g,2}$ and is represented by $T_{g,bulk}$.

The dependence of T_g on film thickness is unusual for amorphous oxide materials. This behavior can be well explained by the dependence of T_g on film thickness that is previously investigated for polymeric glass.[65-75] The release of steric constraints of the free surface cause a reduction in T_g,[65] and the surface is more mobile than the bulk[66]; the particles in bulk are caged by their neighbors and cannot easily change their local environment, whereas the particles in a free surface can move within a larger region and undergo configurational changes to attain lower energy states.[64]

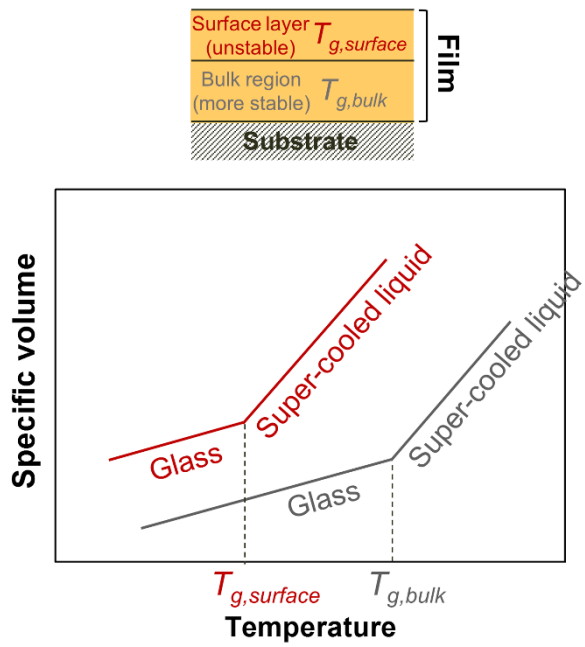

Figure 7.4 Schematic of the specific volume-temperature curve for a-IGZO films for the surface layer and bulk region, describing the separation of T_g. Inset describes a film composed of a surface layer and bulk region.

7.3.3. Continuous surface layer modeling

However, gradual increase of T_g as a function of film thickness is not completely explained using the two layer model. To more precisely describe the surface effect, a continuous layer model[67] was used to fit the thickness-dependence of the $T_{g,surface}$. As described by the inset of **Figure 7.5**, a continuous layer model assumes that a film is composed of infinitesimal multilayers, each of which exhibits its own glass transition temperature ($S_g(x)$), where x is the distance from the free surface of the film. The sum of the infinitesimal multilayers with $S_g(x)$ generates the thickness-dependent $T_g(l)$, where l is the thickness of film. The thickness dependence of T_g reveals the empirical form of the following equation[67]

$$T_g(l) = (T_{g,\infty} \cdot l)/(\xi + l) \tag{7.1}$$

where ξ and $T_{g,\infty}$ are the fitting parameters. Subsequently, the differentiation of **Eq. (7.1)** generates the equation for $S_g(x)$ as follows:[67]

$$S_g(l) = \{T_{g,\infty} \cdot l(2\xi + l)\}/(\xi + l)^2 \tag{7.2}$$

In **Figure 7.5**, the measured $T_{g,surface}$ data (for the heating rate of 1 K/min) were fitted to the $T_g(l)$ of **Eq. (7.1)** and denoted by a dashed line. The $T_{g,\infty}$ was 558±14.2 ℃ and the ξ was 4.25±0.90 nm. Substituting these parameters into **Eq. (7.2)** yields $S_g(x)$, which is depicted as a solid line in **Figure 7.5.** The abrupt decrease in $S_g(x)$ near the free surface (x~0) indicates an unstable surface layer with an approximate thickness of 30 nm.

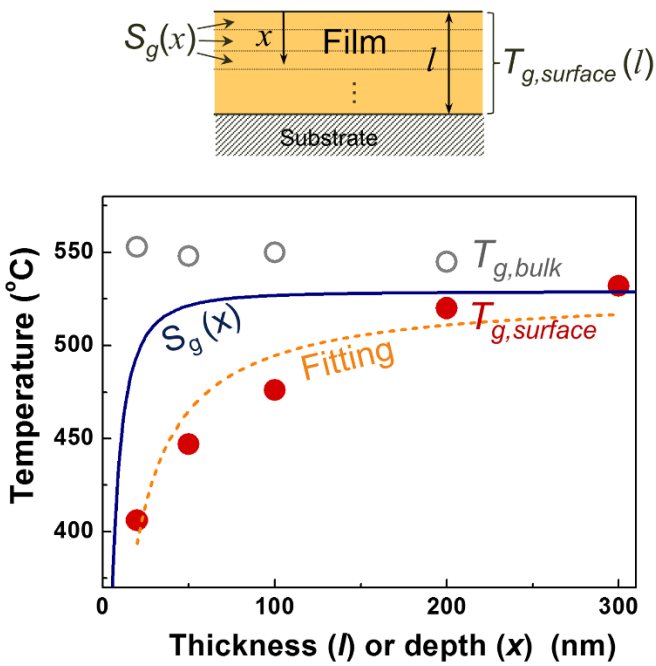

Figure 7.5 Thickness dependence of $T_{g,surface}$ (solid circles) and the fitting according to Eq. (7.1) (dashed line) and Eq. (7.2) (solid line). Inset displays schematic of film composed of infinitesimal multilayers.

7.4. Effect of surface on fragility

We further examined the fragility (*m*), which is the universal criterion for the structural stability of amorphous materials and is defined as the degree of structural reconfiguration near the T_g.[30] As *m* approaches 16, the glass is categorized as a relatively stable "strong glass", whereas larger values reveal a relatively unstable "fragile glass". We obtained *m* from the heating rate dependence of $T_{g,suface}$ using Moynihan's plot, where *E* is the apparent activation energy viscosity at $T = T_g$. and β is the heating rate (K/min).

The heating rate dependence of $T_{g,suface}$ in **Figure 7.6(a)** was obtained from the stress-change curves for various heating rates (from 1.0 ~ 5.0 K/min). As depicted in **Figure 7.6(b)**, the reciprocals of $T_{g,surfaces}$ demonstrate a linear dependence on lnβ; this linear slope provides *E* and *m* according to **Eq. (2.5)** and **(2.9)**, respectively. **Figure 7.6(b)** shows fragility for various film thicknesses, revealing a 300-nm-thick a-IGZO film is a strong (*m*~18) and highly stable glass. Note that these data comprise an initial report on the fragility value for this material. The measured value is reasonable compared with the measured values of other amorphous oxides. (*m*~18 for bulk SiO_2.[32]) We observed that the stability decreases (fragility increases) significantly with decreasing thickness as shown in **Figure 7.6(c)**. This finding can be attributed to the unstable surface layer, which is also supported by the thickness dependence of $T_{g,surface}$. The fragility is generally interpreted using energy landscapes for configuration; a higher energy barrier for configurational changes toward lower energy states generates less fragility.[32] For a-IGZO films, fewer neighbors on the free surface may cause facile configurational changes and greater fragility.

Extrapolated curves of logarithm of the viscosity as a function of reciprocal of

temperature were also obtained for 20 nm ~ 300 nm-thick a-IGZO films according to Vogel-Fulcher-Tammann relation in comparison with SiO_2[111] as depicted in **Figure 7.7**. T_g at which the viscosity is equal to 10^{12} Pa-s is denoted by arrows; T_g changes with various thicknesses and this changes are associated with unconstrained atoms (or ions) at surface regions. Fragility of a-IGZO also increases with decreasing thickness (larger surface-to-volume ratio), which means higher mobility of atoms (or ions) at surface regions.

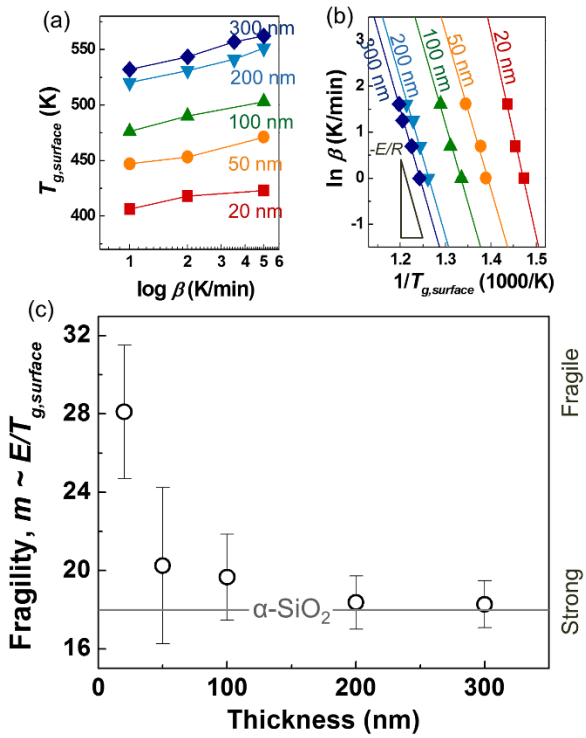

Figure 7.6 (a) Dependence of T_g on heating rates (β) and (b) linear dependences of ln β on $1/T_g$ for various film thickness. (c) Fragility for various film thicknesses. Strong characteristics of 300-nm-thick IGZO film (m ~ 18) changes to relatively fragile characteristics (m ~ 28) as thickness decreases, which means larger surface-to-volume ratio.

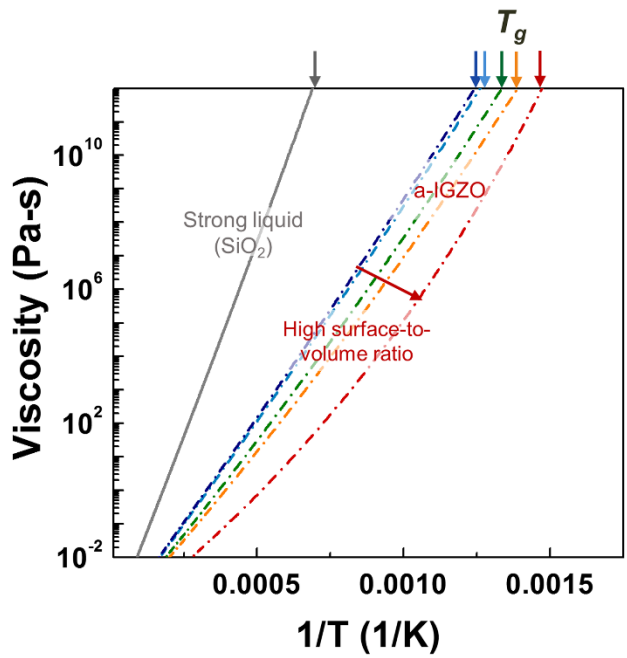

Figure 7.7 Extrapolated curves of logarithm of the viscosity as a function of reciprocal of temperature were also obtained for 20 nm ~ 300 nm-thick a-IGZO films according to Vogel-Fulcher-Tammann relation in comparison with SiO_2.[111]

7.5. Structural relaxation in glass

7.5.1. Stress evolution in glass

The previous discussion primarily focused on the characteristics of T_g and its dependence on thickness. As shown in **Figure 7.2**, significant structural relaxation of glass occurred at temperatures below T_g. We investigated the mechanisms responsible for this relaxation using stress-temperature curves and X-ray reflectivity (XRR) measurements. **Figure 7.8(a)** displays the stress-temperature curve of 50-nm-thick a-IGZO film. The gray solid lines depict the film's stress response toward thermal cycling with peak temperatures that vary from 87 to 550 ℃. The 1st heat cycle (up to 87 ℃) causes a linear and reversible stress change due to the CTE mismatch between the film and the Si wafer. In subsequent cycles with higher peak temperatures, the stress changes were linear and reversible to the peak temperatures of the previous cycle. After heating above the peak temperatures of the previous cycle, an irreversible stress change occurred, which coincided with the stress curve during the continuous heating; these changes are denoted by open circles. Therefore, the irreversible structural changes occurred in the range of 87-550 ℃ during heating rather than during cooling.

Figure 7.9 show the GIXRD data indicating that the crystallization occurred after annealing to 640 ℃ as the evolution of tensile stress is observed around this temperature. No significant phase change was detected up to 550 ℃, thus the stress change up to this point is mainly due to structural change or glass transition of amorphous phase, not due to crystallization.

7.5.2. Thickness and density changes

Changes in thickness and density along with the temperature were measured using *ex-situ* XRR, as presented in **Figure 7.8(b)**. Along with the real-time mechanical stress measurement of a-IGZO film, the *ex-situ* measurement of X-ray reflectivity (XRR) were accompanied to observe how the thickness and density of the film changes with annealing. For the samples after the annealing to various peak temperatures (87 - 640 ° C), XRR measurement was conducted. It should be noted that the thicker 525 μm Si wafer was used as a substrate for the XRR measurements because the bending of samples restricts the accurate measurement. However, the samples experienced the same annealing condition as the samples of **Figure 7.8(a)**. Open circles in **Figure 7.10(a)-(g)** indicate the XRR signal of the samples for various peak temperatures (peak temperatures are denoted in the figures), and the solid lines indicate the fitting of the measured data. The fitting provides material parameters, such as the thicknesses and the densities for the films. **Figure 7.10(h)** indicates the solid lines in **Figure 7.10(a)-(g)** (fitting) for the comparison. As the lateral positions of the fringes determines the thicknesses of the films, the shift of the fringes from 450 ℃-annealed samples manifests the thickness change begins after 450 ℃. Obtained values of material parameters (thicknesses and densities) are shown in **Figure 7.8(b)** in manuscript.

For the stress changes, the relaxation occurred in the range of 87 - 450 ℃; however, a noticeable densification and change in thickness began after 350 ℃. The inconsistencies can be explained by the different types of mechanisms for the structural relaxation of glass: i) densification, thermally induced volume shrinkage and ii) viscous flow, the relaxation of stress caused by a reduction in viscosity at relatively high temperatures.[112, 113]

Densification is stress-independent: the stress change in the 350-450 ℃ region is dominated by the densification because the stress evolves toward the tensile direction above the stress-free point ($\sigma = 0$) and accompanies changes in thickness and density. The densification region can be utilized to optimize the stabilization temperature of a-IGZO-based electronic devices, where the major structural changes begin. Conversely, the viscous flow is stress-dependent: the stress changes toward the zero value to relieve the absolute stress. Therefore, the stress changes below 350 ℃ are dominated by the viscous flow because this region relaxes compressive stress without a noticeable increase in density. T_{relax} is the temperature at which viscous flow begins and shows a distinct dependence on the residual stresses (deposition stress) of the films as shown in **Figure 7.11**. The stress change in viscous flow region can be used to predict the stress-induced delamination of films. Besides, the change of deposition method and condition varies the density of the film. Film with lower density will more easily relax the stress, which ends up with lower residual stress. Lower absolute stress will change the stress change during viscous flow and T_{relax}.

We believe that the structural instability of a-IGZO film has the relevance to the reliability issues for a-IGZO thin-film transistor (TFT), especially for the surface-originated instability. However, direct measurement of the relevance is restricted by the inconsistency between them: small island structure of TFT is in the situation distinct from the thin film, mostly the stress and the surface-to-volume ratio. Moreover, there is no proper methodology to directly measure the mechanical stress in small island structure of TFT, while the thin film structure is suitable for real-time mechanical stress measurement.

However, value of absolute stress will not significantly change the parameters for phase and structural changes (T_g, T_x and fragility) which is determined by the inherent

amorphous structure. Therefore, the main findings of this manuscript will also be applicable for TFT, which is supported by experimental observations: the threshold voltage shift during bias stress shows thickness dependence[114] and the surface treatment improves the TFT characteristics.[115]

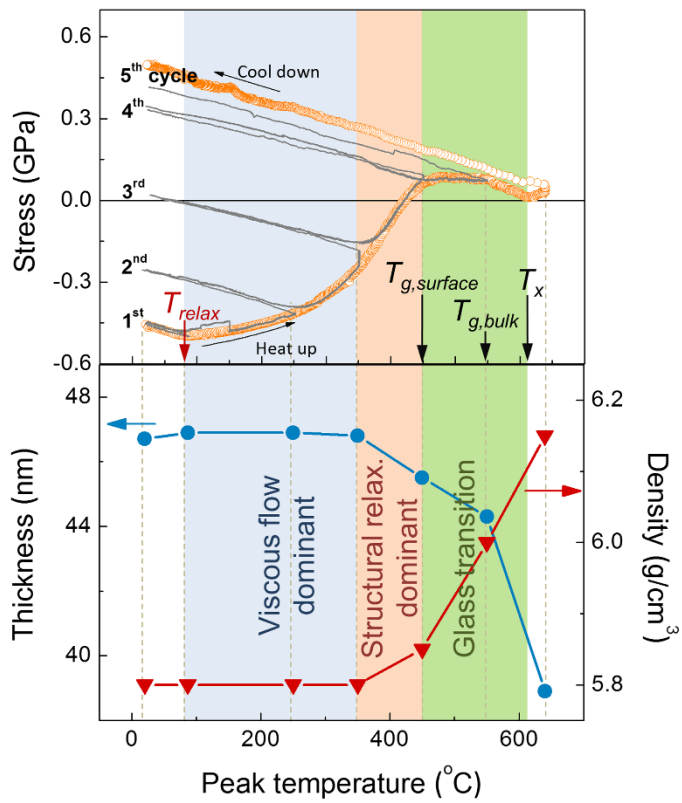

Figure 7.8 (a) Stress-temperature curve for a 50 nm-thick a-IGZO film, which describes the repeated cycling with increasing peak temperature. (b) Thickness and density changes as measured by *ex-situ* X-ray reflectivity measurement.

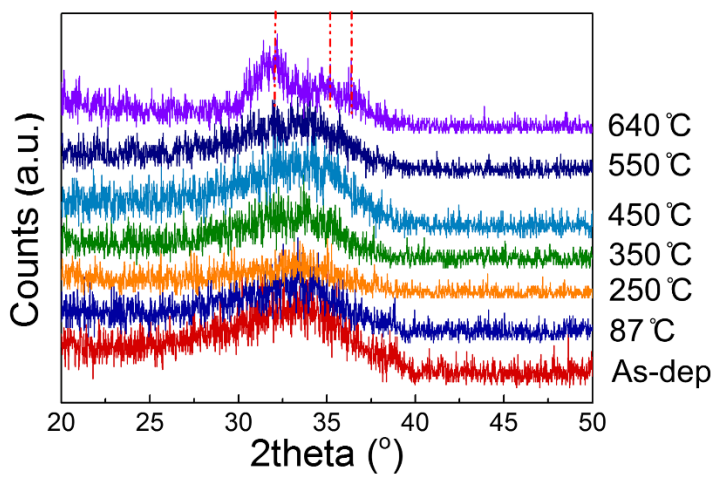

Figure 7.9 Grazing incident X-ray diffraction patterns of 50 nm-thick a-IGZO thin film for various peak temperatures of thermal cycling. This data indicates that crystallization has not occurred up to 550 ℃ annealing.

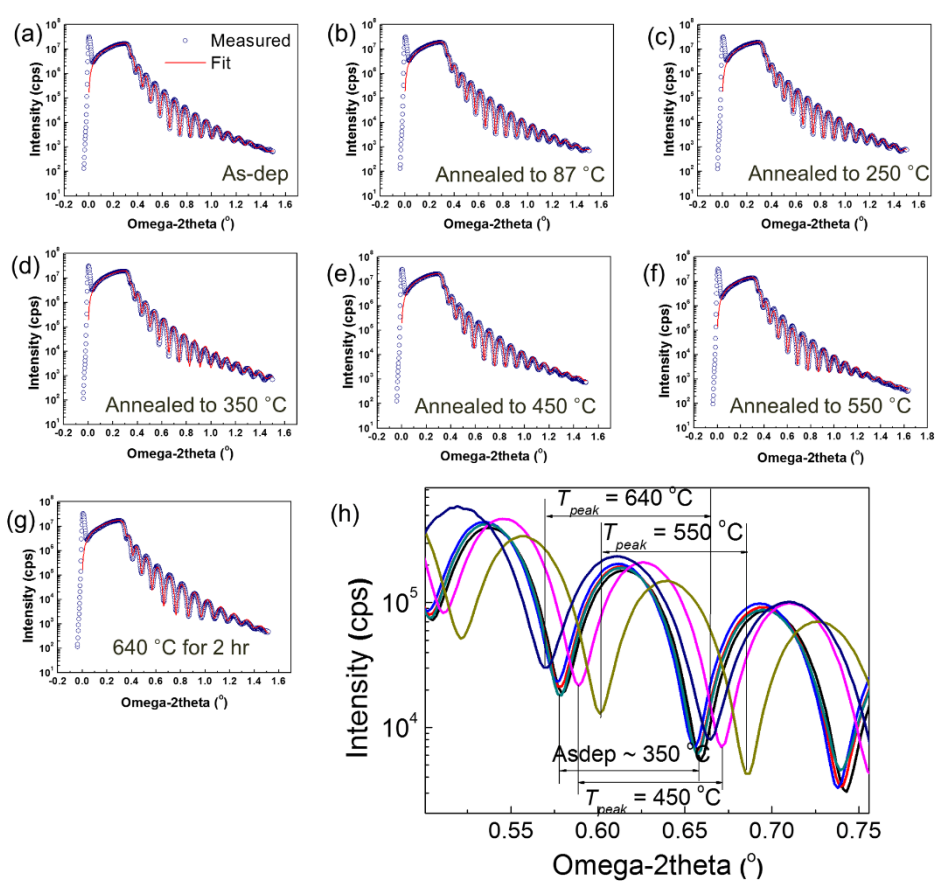

Figure 7.10 (a)-(g) X-ray reflectivity spectra of 50 nm-thick a-IGZO thin film for various peak temperatures (87-640 ℃) of thermal cycling (Cu K_α : λ=1.54056 Å). (h) Lateral positions of fringes begin to be shifted from the 450 ℃-annealed samples, which reflects the change of thickness started from 450 ℃ sample.

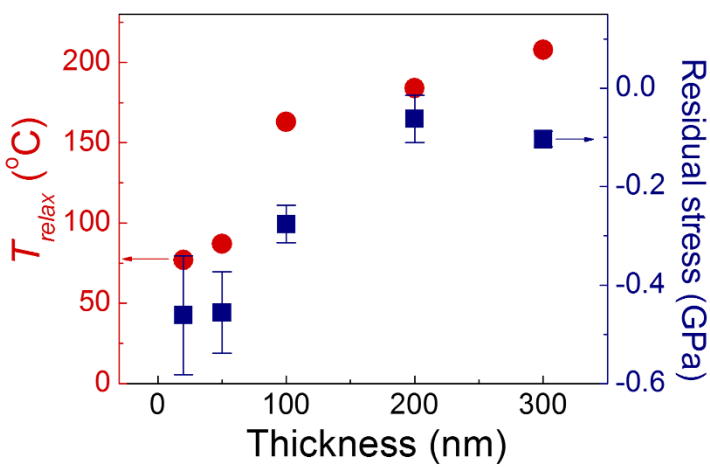

Figure 7.11 T_{relax} (solid circles) obtained from the Figure 7.2 and the residual stresses (solid squares) for film thicknesses.

7.6. Summary

This Chapter reports the first measurements of the glass transition and fragility of a-IGZO film investigated by a mechanical stress analysis.[116] Through the dependence of these behaviors on film thickness, we can identify that the structural instability near the glass transition temperature originates from the surface layer. At temperatures below the glass transition temperature, we also find that the structural relaxation of glass was attributed to the viscous flow that relieves the residual stress and densification. Our study offers a physical understanding of the mechanisms that govern the structural instability of amorphous materials. The structural instability changes with the temperature and deposition condition of films, such as thickness and residual stress. We demonstrated that a real-time mechanical stress analysis is effective for detection of the slight variation in volume that is associated with the phase and structural changes for interpreting the structural instability of amorphous materials.

In conclusion, the glass transition, crystallization, and structural relaxation of glass were quantified using real-time mechanical analysis. The glass transition is determined by the structural instability that originates from the surface layer, which is manifested by the lower T_g (423 ℃) and fragility (~28) of 20-nm-thick films compared with the T_g (562 ℃) and fragility (~18) of 300-nm-thick films. At temperatures below T_g, the structural relaxation of glass was explained by the viscous flow and densification of the films.

CHAPTER 8

Conclusion

8.1. Modulating amorphous materials

This study investigated the structural changes of amorphous semiconductors and unraveled the physics that are relevant to bond networks using mechanical stress analysis. A thorough analysis of experimental data in conjunction with theoretical models helped to build a framework to describe and explain the unconventional properties of amorphous semiconductors that are used in applications for electronic devices.

Based on the insight obtained, a comprehensive understanding of amorphous semiconductors, including phase change materials and amorphous oxide semiconductors, has been developed. **Figure 8.1** shows the extrapolated curves of the logarithm of the viscosity as a function of the reciprocal of temperature that were obtained for GST films doped with various dopants (Al 8.5 at.%, Bi 9.6 at.%, C 10 at.% and N 10 at.%) and a-IGZO films with various thicknesses according to the Vogel-Fulcher-Tammann relation in comparison with strong and stable behavior (SiO_2) in the

Arrhenius relationship.[111] Phase change materials (GST) show large deviations from the Arrhenius behavior of SiO_2, which results in relatively rapid decreases in η and τ (rapid increase in atomic mobility) with temperature. Therefore, GST can be regarded as a fragile glass, as was described in Chapter 4. In contrast a-IGZO shows less deviation from Arrhenius behavior, which results in a gradual decrease in η and τ (gradual increase in atomic mobility) with temperature. Therefore, a-IGZO is relatively strong.

Structural variations in GST and a-IGZO change the fragility (tendency for deviation from Arrhenius behavior). For GST films, C and N doping leads to less fragile behavior and a gradual increase in atomic mobility with temperature. However, Al doping maintains the fragile characteristics. For a-IGZO films, thinner films (higher surface-to-volume ratios) lead to more fragile characteristics and larger deviations from the Arrhenius behavior of 300-nm-thick a-IGZO films, as was described in Chapter 7

The temperatures T_g at which the viscosity is equal to 10^{12} Pa are denoted by arrows in **Figure 8.1**; T_g changes with doping, and these changes are associated with the bonding enthalpy in covalently bonded systems of phase change materials, as was discussed in Chapter 4. For a-IGZO, the less-constrained bonding of atoms in the surface region (fewer neighboring atoms) likely leads to lower T_g and lower thermal stability against crystallization.

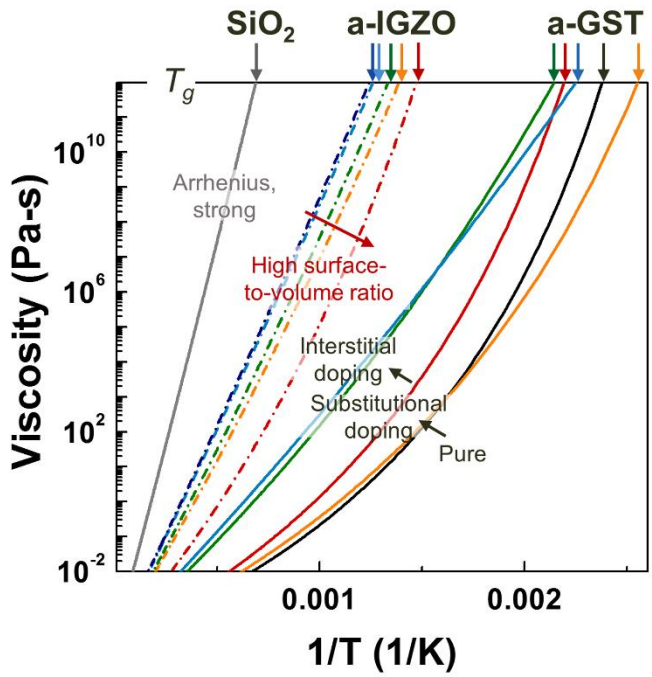

Figure 8.1 Extrapolated curves of the logarithm of the viscosity as a function of the reciprocal of temperature for GST films doped with various dopants (Al 8.5 at.%, C 10 at.% and N 10 at.%) and a-IGZO films with various thicknesses according to the Vogel-Fulcher-Tammann relation in comparison with strong and stable behavior (SiO_2) in the Arrhenius relation.[111]

8.2. Material design for the improvement of devices

The findings on the structural stability of the various amorphous materials provide a strategy for the improvement of the reliability problems in electronics, which are described in **Figure 8.2**. For phase change materials (e.g., GST), the inherently fragile and the unstable nature of the material leads to structural instability. Therefore, the overall structure should be stabilized by doping. Because the stability is controlled by the bonding enthalpy of the system (while the fragility is controlled by the free volume), substitutional doping will be a better choice to enhance the stability while maintaining fragility. For a-IGZO, it has inherent stability and strong nature leading to high structural stability. However, the unstable surface layer can act as a weak point that leads to structural instability and reliability issues in devices. Therefore, surface treatment (e.g., passivation, UV treatment) would enhance the structural stability, which has been confirmed by experimental data.[115]

This thesis establishes guidelines for improving devices based on the structural stability of amorphous semiconductors.

8.3. Future work and suggested research

In this study, the concepts described above are based on *macroscopically observable properties*. To establish the relationship between the bond networks and the material properties that are relevant for the crystallization behavior, new concepts need to be explored: *the atomic scale approach*.

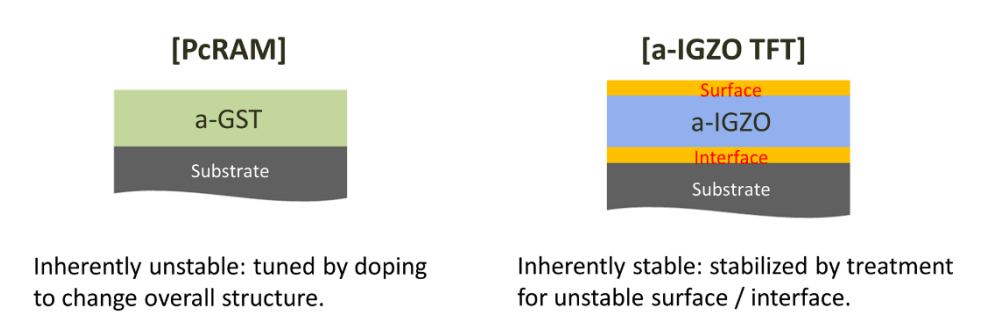

Figure 8.2 Description of a strategy for improving the reliability problems in electronics based on the findings on the structural stability of various amorphous materials.

The unique features of crystallization in phase change materials are known to be closely related to the atomic arrangement in the bond network. For example, the interplay of heteropolar and homopolar bonding is important for device characteristics because homopolar bonding needs to be broken when the transformation occurs; this was investigated in my previous research with co-workers.[117, 118] Therefore, the verification of the atomic scale mechanism of phase transformation based on the unique bonding characteristics of amorphous phase change materials is required.

In a future project, the relationship between the bond networks of amorphous phase change materials and the material properties that are relevant to crystallization will be investigated using a combination of characterization methods. A theoretical model will be established based on macroscopic and atomic scale observations. Based on the theoretical background and experimental analysis, the material properties of amorphous phase change materials will be tuned to improve the PcRAM device characteristics.

Extended x-ray absorption fine-structure spectroscopy (EXAFS) is a fascinating method of determining the local atomic arrangement for a selected atomic species in phase change materials. EXAFS will be utilized to determine the distances, coordination numbers and species of the neighbors of absorbing atoms. Importantly, crystallinity is not required for EXAFS measurements, which makes it one of the few structural probes available for amorphous phase change materials.

A theoretical model to relate the bond network to the material properties needs to be established. This relationship must be based on macroscopically observable properties, such as the glass transition temperature, crystallization temperature, fragility, viscosity and relaxation time. These properties will be related to the material properties, such as the bonding enthalpy and the free volume, to provide the first ‘treasure’ map. Such a map needs to include insights obtained from the atomic arrangement of the bond

network. Hence, the structural properties of amorphous phase change materials and their relevance to the resulting properties must be established.

The properties will be tuned based on the established framework described above that relates the material properties to the bond network. To facilitate the discussion, it will be useful to represent the energy landscapes for different glasses. The topology of the energy landscape is determined by the interplay of the configuration of the bond network and the energy required for atomic rearrangements, which are closely related to the thermodynamic and kinetic fragility of the amorphous solids. This concept allows the individual control of the thermodynamic and kinetic stabilities, which helps to develop amorphous phase change materials with high stabilities at low temperatures and rapid crystallization at higher temperatures. A model for the bond network in ideal phase change materials will be developed for this purpose. Subsequently, the bond network will be tuned and optimized by stoichiometry changes.

As described above, controlling the networks of amorphous phase change materials is important because it is beneficial for improving advanced functional devices. Hence, we must be able to control the bond networks in the materials to improve current devices and to develop a novel concept of tailoring material properties. The material properties of amorphous phase change materials will be tuned based on the findings from the bond networks.

PcRAM devices based on Ge-Sb-Te alloys will be fabricated to verify the relationship between the material properties and the characteristics of the devices. The memory device has an electrode contact that is less than 300 nm in diameter. The data retention, SET time and resistance drift of PcRAM devices will be investigated and compared to the material properties.

References

1. R. Zallen, *The Physics of Amorphous Solids*, Wiley-VCH, Weinheim (2004).

2. D. Lencer, M. Salinga, B. Grabowski, T. Hickel, J. Neugebauer and M. Wuttig, *Nature Materials*, **7**, 972 (2008).

3. H. S. P. Wong, S. Raoux, S. Kim, J. Liang, J. P. Reifenberg, B. Rajendran, M. Asheghi and K. E. Goodson, *Proc. IEEE*, **98**, 2201 (2010).

4. H. Y. Cheng, M. Brightsky, S. Raoux, C. F. Chen, P. Y. Du, J. Y. Wu, Y. Y. Lin, T. H. Hsu, Y. Zhu, S. Kim, C. M. Lin, A. Ray, H. L. Lung and C. Lam, in *2013 IEEE International Electron Devices Meeting, IEDM 2013*, p. 30.6.1, Washington, DC (2013).

5. J. Y. Cho, T. Y. Yang, Y. J. Park and Y. C. Joo, *Electrochemical and Solid-State Letters*, **15**, H81 (2012).

6. Y. H. Shih, J. Y. Wu, B. Rajendran, M. H. Lee, R. Cheek, M. Lamorey, M. Breitwisch, Y. Zhu, E. K. Lai, C. F. Chen, E. Stinzianni, A. Schrott, E. Joseph, R. Dasaka, S. Raoux, H. L. Lung and C. Lam, in *2008 IEEE International Electron Devices Meeting*, San Francisco, CA (2008).

7. B. Gleixner, A. Pirovano, J. Sarkar, F. Ottogalli, E. Tortorelli, M. Tosi and R. Bez, in *45th Annual IEEE International Reliability Physics Symposium 2007, IRPS*, p. 542, Phoenix, AZ (2007).

8. Y. H. Chiu, Y. B. Liao, M. H. Chiang, C. L. Lin, W. C. Hsu, P. C. Chiang, Y. Y. Hsu, W. H. Liu, S. S. Sheu, K. L. Su, M. J. Kao and M. J. Tsai, in *2010 IEEE*

International Conference on Integrated Circuit Design and Technology, ICICDT 2010, p. 20, Grenoble (2010).

9. J. Li, B. Luan and C. Lam, in *2012 IEEE International Reliability Physics Symposium, IRPS 2012*, p. 6C.1.1, Anaheim, CA (2012).

10. I. V. Karpov, M. Mitra, D. Kau, G. Spadini, Y. A. Kryukov and V. G. Karpov, *J. Appl. Phys.*, **102**, 124503 (2007).

11. D. Ielmini, S. Lavizzari, D. Sharma and A. L. Lacaita, *IEDM Tech. Dig.* (2007).

12. M. Mitra, Y. Jung, D. S. Gianola and R. Agarwal, *Appl. Phys. Lett.*, **96**, 222111 (2010).

13. S. Kim, B. Lee, M. Asheghi, F. Hurkx, J. P. Reifenberg, K. E. Goodson and H. S. P. Wong, *IEEE Trans. Electron Devices*, **58**, 584 (2011).

14. Y.-H. Chiu, Y.-B. Liao, M.-H. Chiang, C.-L. Lin, W.-C. Hsu, P.-C. Chiang, Y.-Y. Hsu, W.-H. Liu, S.-S. Sheu, K.-L. Su, M.-J. Kao and M.-J. Tsai, in *IC Design and Technology (ICICDT), 2010 IEEE International Conference on*, p. 20 (2010).

15. A. Pirovano, A. L. Lacaita, F. Pellizzer, S. A. Kostylev, A. Benvenuti and R. Bez, *Electron Devices, IEEE Transactions on*, **51**, 714 (2004).

16. J. Kalb, F. Spaepen, T. P. L. Pedersen and M. Wuttig, *J. Appl. Phys.*, **94**, 4908 (2003).

17. K. Nomura, H. Ohta, A. Takagi, T. Kamiya, M. Hirano and H. Hosono, *Nature*, **432**, 488 (2004).

18. H. Hosono, *J. Non-Cryst. Solids*, **352**, 851 (2006).

19. J. F. Conley Jr, *IEEE Transactions on Device and Materials Reliability*, **10**, 460 (2010).

20. A. Suresh and J. F. Muth, *Appl. Phys. Lett.*, **92** (2008).

21. K. Nomura, T. Kamiya, M. Hirano and H. Hosono, *Appl. Phys. Lett.*, **95** (2009).

22. K. Nomura, T. Kamiya, H. Ohta, K. Shimizu, M. Hirano and H. Hosono, *Physica Status Solidi (A) Applications and Materials Science*, **205**, 1910 (2008).

23. K. Ide, K. Nomura, H. Hiramatsu, T. Kamiya and H. Hosono, *J. Appl. Phys.*, **111** (2012).

24. W. D. Nix, *Metall. Trans. A*, **20**, 2217 (1989).

25. S. R. Elliott, *Physics of Amorphous Materials*, Longman Scientific & Technical (1984).

26. R. Abbaschian and R. Reed-Hill, *Physical Metallurgy Principles*, Cengage Learning (2008).

27. R. Abbaschian, L. Abbaschian and R. E. R. Hill, *Physical Metallurgy Principles*, Cengage Learning (2008).

28. F. Spaepen, *Acta Metall.*, **25**, 407 (1977).

29. A. K. Doolittle, *J. Appl. Phys.*, **22**, 1471 (1951).

30. C. A. Angell, *J. Non-Cryst. Solids*, **102**, 205 (1988).

31. P. G. Debenedetti and F. H. Stillinger, *Nature*, **410**, 259 (2001).

32. C. A. Angell, *J. Non-Cryst. Solids*, **131–133, Part 1**, 13 (1991).

33. R. Böhmer and C. A. Angell, *Physical Review B*, **45**, 10091 (1992).

34. T. A. Vilgis, *Physical Review B*, **47**, 2882 (1993).

35. J. Rault, *J. Non-Cryst. Solids*, **271**, 177 (2000).

36. J. Orava, A. L. Greer, B. Gholipour, D. W. Hewak and C. E. Smith, *Nature Materials*, **11**, 279 (2012).

37. R. Böhmer, *J. Non-Cryst. Solids*, **172-174**, 628 (1994).

38. C. T. Moynihan, A. J. Easteal, J. Wilder and J. Tucker, *Journal of Physical Chemistry*, **78**, 2673 (1974).

39. A. A. Elabbar, *Physica B: Condensed Matter*, **403**, 4328 (2008).

40. A. A. Elabbar, *Journal of Alloys and Compounds*, **476**, 125 (2009).

41. A. T. Patel and A. Pratap, *Journal of Thermal Analysis and Calorimetry*, **110**, 567 (2012).

42. O. A. Lafi, M. M. A. Imran, M. K. Abdullah and S. A. Al-Sakhel, *Thermochimica Acta*, **560**, 71 (2013).

43. O. A. Lafi and M. M. A. Imran, *Journal of Alloys and Compounds*, **509**, 5090 (2011).

44. S. S. Tsao and F. Spaepen, *Acta Metall.*, **33**, 881 (1985).

45. K. Shportko, S. Kremers, M. Woda, D. Lencer, J. Robertson and M. Wuttig, *Nature Materials*, **7**, 653 (2008).

46. M. Salinga, E. Carria, A. Kaldenbach, M. Bornhöfft, J. Benke, J. Mayer and M. Wuttig, *Nat Commun*, **4** (2013).

47. M. Wuttig and M. Salinga, *Nature Materials*, **11**, 270 (2012).

48. D. Dimitrov and H. P. D. Shieh, *Materials Science and Engineering B: Solid-State Materials for Advanced Technology*, **107**, 107 (2004).

49. I. M. Park, J. Y. Cho, T. Y. Yang, E. S. Park and Y. C. Joo, *Jpn. J. Appl. Phys.*, **50** (2011).

50. I.-M. Park, T.-Y. Yang, S. W. Jung, Y. K. Kim, H. Horii and Y.-C. Joo, *Appl. Phys. Lett.*, **94**, 061904 (2009).

51. Q. Hubert, C. Jahan, A. Toffoli, G. Navarro, S. Chandrashekar, P. Noé, D. Blachier, V. Sousa, L. Perniola, J. F. Nodin, A. Persico, R. Kies, S. Maitrejean, A. Roule, E. Henaff, M. Tessaire, P. Zuliani, R. Annunziata, G. Pananakakis, G. Reimbold and B. De Salvo, in *2012 4th IEEE International Memory Workshop, IMW 2012*, Milano (2012).

52. Q. Hubert, C. Jahan, A. Toffoli, G. Navarro, S. Chandrashekar, P. Noé, V. Sousa, L. Perniola, J. F. Nodin, A. Persico, S. Maitrejean, A. Roule, E. Henaff, M. Tessaire, P. Zuliani, R. Annunziata, G. Reimbold, G. Pananakakis and B. De Salvo, in *42nd European Solid-State Device Research Conference, ESSDERC 2012*, p. 286, Bordeaux (2012).

53. T. Y. Yang, J. Y. Cho, Y. J. Park and Y. C. Joo, *Acta Materialia*, **60**, 2021 (2012).

54. S. F. Chen, J. K. Chen and T. P. Chen, *Materials Science and Technology*, **24**, 501 (2008).

55. G. Wang, X. Shen, Q. Nie, R. Wang, L. Wu, Y. Lv, F. Chen, J. Fu, S. Dai and J. Li, *Journal of Physics D: Applied Physics*, **45** (2012).

56. S. Raoux, M. Salinga, J. L. Jordan-Sweet and A. Kellock, *J. Appl. Phys.*, **101**

(2007).

57. C. T. Lie, P. C. Kuo, W. C. Hsu, T. H. Wu, P. W. Chen and S. C. Chen, *Japanese Journal of Applied Physics, Part 1: Regular Papers and Short Notes and Review Papers*, **42**, 1026 (2003).

58. J. Zhou, Z. Sun, L. Xu and R. Ahuja, *Solid State Communications*, **148**, 113 (2008).

59. K. H. Song, S. W. Kim, J. H. Seo and H. Y. Lee, *J. Appl. Phys.*, **104** (2008).

60. T. Kamiya and H. Hosono, *NPG Asia Mater.*, **2**, 15 (2010).

61. M. I. Ojovan, *Advances in Condensed Matter Physics*, **2008** (2008).

62. X. P. Tang, U. Geyer, R. Busch, W. L. Johnson and Y. Wu, *Nature*, **402**, 160 (1999).

63. A. Nathan, S. Lee, S. Jeon, I. Song and U. I. Chung, *Inf Disp*, **29**, 6 (2013).

64. G. Parisi and F. Sciortino, *Nature Materials*, **12**, 94 (2013).

65. J. A. Torres, P. F. Nealey and J. J. De Pablo, *Physical Review Letters*, **85**, 3221 (2000).

66. K. F. Mansfield and D. N. Theodorou, *Macromolecules*, **24**, 6283 (1991).

67. J. H. Kim, J. Jang and W. C. Zin, *Langmuir*, **17**, 2703 (2001).

68. O. Bäumchen, J. D. McGraw, J. A. Forrest and K. Dalnoki-Veress, *Physical Review Letters*, **109** (2012).

69. C. J. Ellison and J. M. Torkelson, *Nature Materials*, **2**, 695 (2003).

70. D. S. Fryer, P. F. Nealey and J. J. De Pablo, *Macromolecules*, **33**, 6439 (2000).

71. J. L. Keddie, R. A. L. Jones and R. A. Cory, *Faraday Discussions*, **98**, 219 (1994).

72. P. A. O'Connell and G. B. McKenna, *Science*, **307**, 1760 (2005).

73. R. D. Priestley, C. J. Ellison, L. J. Broadbelt and J. M. Torkelson, *Science*, **309**, 456 (2005).

74. H. Wang, J. K. Keum, A. Hiltner, E. Baer, B. Freeman, A. Rozanski and A. Galeski, *Science*, **323**, 757 (2009).

75. H. Zhou, H. K. Kim, F. G. Shi, B. Zhao and J. Yota, *Microelectronics Journal*, **33**, 221 (2002).

76. S. Napolitano and M. Wübbenhorst, *Nat. Commun.*, **2** (2011).

77. G. B. DeMaggio, W. E. Frieze, D. W. Gidley, M. Zhu, H. A. Hristov and A. F. Yee, *Physical Review Letters*, **78**, 1524 (1997).

78. S. K. Lee and C. W. Ahn, *Scientific Reports*, **4** (2014).

79. S. K. Lee, S. Y. Park, Y. S. Yi and J. Moon, *Journal of Physical Chemistry C*, **114**, 13890 (2010).

80. Z. Cao and X. Zhang, *Journal of Physics D: Applied Physics*, **39**, 5054 (2006).

81. M. H. R. Lankhorst, *J. Non-Cryst. Solids*, **297**, 210 (2002).

82. L. Tichý and H. Tichá, *J. Non-Cryst. Solids*, **189**, 141 (1995).

83. T. Y. Yang, J. Y. Cho, Y. J. Park and Y. C. Joo, in *18th IEEE International Symposium on the Physical and Failure Analysis of Integrated Circuits, IPFA 2011*, Incheon (2011).

84. J. H. Seo, K. H. Song and H. Y. Lee, *J. Appl. Phys.*, **108** (2010).

85. C. Peng, Z. Song, F. Rao, L. Wu, M. Zhu, H. Song, B. Liu, X. Zhou, D. Yao, P. Yang and J. Chu, *Appl. Phys. Lett.*, **99** (2011).

86. C. Peng, L. Wu, F. Rao, Z. Song, X. Zhou, M. Zhu, B. Liu, D. Yao, S. Feng, P. Yang and J. Chu, *Scripta Materialia*, **65**, 327 (2011).

87. K. Ren, F. Rao, Z. Song, C. Peng, J. Li, L. Wu, B. Liu and S. Feng, *Appl. Phys. Lett.*, **103** (2013).

88. K. Ren, F. Rao, Z. Song, L. Wu, M. Xia, B. Liu and S. Feng, *J. Appl. Phys.*, **113** (2013).

89. M. Zhu, L. Wu, F. Rao, Z. Song, X. Li, C. Peng, X. Zhou, K. Ren, D. Yao and S. Feng, *Journal of Alloys and Compounds*, **509**, 10105 (2011).

90. R. M. Shelby and S. Raoux, *J. Appl. Phys.*, **105** (2009).

91. X. Zhou, L. Wu, Z. Song, F. Rao, M. Zhu, C. Peng, D. Yao, S. Song, B. Liu and S. Feng, *Appl. Phys. Lett.*, **101** (2012).

92. G. Betti Beneventi, L. Perniola, V. Sousa, E. Gourvest, S. Maitrejean, J. C. Bastien, A. Bastard, B. Hyot, A. Fargeix, C. Jahan, J. F. Nodin, A. Persico, A. Fantini, D. Blachier, A. Toffoli, S. Loubriat, A. Roule, S. Lhostis, H. Feldis, G. Reimbold, T. Billon, B. De Salvo, L. Larcher, P. Pavan, D. Bensahel, P. Mazoyer, R. Annunziata, P. Zuliani and F. Boulanger, *Solid-State Electronics*, **65-66**, 197 (2011).

93. G. B. Beneventi, L. Perniola, A. Fantini, D. Blachier, A. Toffoli, E. Gourvest, S. Maitrejean, V. Sousa, C. Jahan, J. F. Nodin, A. Persico, S. Loubriat, A. Roule, S. Lhostis, H. Feldis, G. Reimbold, T. Billon, B. De Salvo, L. Larcher, P. Pavan, D.

Bensahel, P. Mazoyer, R. Annunziata and F. Boulanger, in *2010 European Solid State Device Research Conference, ESSDERC 2010*, p. 313, Sevilla (2010).

94. C. Peng, L. Wu, Z. Song, F. Rao, M. Zhu, X. Li, B. Liu, L. Cheng, S. Feng, P. Yang and J. Chu, *Applied Surface Science*, **257**, 10667 (2011).

95. K. B. Borisenko, Y. Chen, D. J. H. Cockayne, S. A. Song and H. S. Jeong, *Acta Materialia*, **59**, 4335 (2011).

96. E. Cho, Y. Youn and S. Han, *Appl. Phys. Lett.*, **99** (2011).

97. E. Cho, S. Han, D. Kim, H. Horii and H. S. Nam, *J. Appl. Phys.*, **109** (2011).

98. T. H. Jeong, M. R. Kim, H. Seo, J. W. Park and C. Yeon, *Jpn. J. Appl. Phys.*, **39**, 2775 (2000).

99. C. F. Chen, A. Schrott, M. H. Lee, S. Raoux, Y. H. Shih, M. Breitwisch, F. H. Baumann, E. K. Lai, T. M. Shaw, P. Flaitz, R. Cheek, E. A. Joseph, S. H. Chen, B. Rajendran, H. L. Lung and C. Lam, in *2009 IEEE International Memory Workshop, IMW '09*, Monterey, CA (2009).

100. S. J. Kim, S. C. Lee and J. H. Choi, *Journal of Nanoscience and Nanotechnology*, **12**, 6113 (2012).

101. T. Nonaka, G. Ohbayashi, Y. Toriumi, Y. Mori and H. Hashimoto, *Thin Solid Films*, **370**, 258 (2000).

102. S. M. Sze, *Physics of Semiconductor Devices*, Wiley, New York (1981).

103. J. Im, E. Cho, D. Kim, H. Horii, J. Ihm and S. Han, *Current Applied Physics*, **11**, e82 (2011).

104. I.-M. Park, J.-K. Jung, S.-O. Ryu, K.-J. Choi, B.-G. Yu, Y.-B. Park, S. M. Han and Y.-C. Joo, *Thin Solid Films*, **517**, 848 (2008).

105. A. Witvrouw and F. Spaepen, *J. Appl. Phys.*, **74**, 7154 (1993).

106. S. W. Ryu, J. H. Lee, Y. B. Ahn, C. H. Kim, B. S. Yang, G. H. Kim, S. G. Kim, S.-H. Lee, C. S. Hwang and H. J. Kim, *Appl. Phys. Lett.*, **95**, 112110 (2009).

107. M. Boniardi, D. Ielmini, S. Lavizzari, A. L. Lacaita, A. Redaelli and A. Pirovano, *IEEE Trans. Electron Devices*, **57**, 2690 (2010).

108. B. Yaglioglu, Y. J. Huang, H. Y. Yeom and D. C. Paine, *Thin Solid Films*, **496**, 89 (2006).

109. H. Y. Yeom, N. Popovich, E. Chason and D. C. Paine, *Thin Solid Films*, **411**, 17 (2002).

110. B. J. Kim, K. Y. Park, J. H. Ahn and Y. J. Kim, *Jpn. J. Appl. Phys.*, **51** (2012).

111. M. L. F. Nascimento and E. D. Zanotto, *Physical Review B - Condensed Matter and Materials Physics*, **73** (2006).

112. C. A. Volkert, *J. Appl. Phys.*, **74**, 7107 (1993).

113. Z. Cao and X. Zhang, *Sensors and Actuators, A: Physical*, **127**, 221 (2006).

114. S. Y. Lee, D. H. Kim, E. Chong and Y. W. Jeon, *Appl. Phys. Lett.*, **98** (2011).

115. M. Kimura, T. Hasegawa, K. Ide, K. Nomura, T. Kamiya and H. Hosono, *Solid-State Electronics*, **75**, 74 (2012).

116. J.-Y. Cho, T.-Y. Yang, Y.-J. Park, Y.-Y. Lee and Y.-C. Joo, *ECS Solid State Letters*, **3**, P73 (2014).

117. S. Sen, T. G. Edwards, J. Y. Cho and Y. C. Joo, *Physical Review Letters*, **108** (2012).

118. B. Kalkan, S. Sen, J. Y. Cho, Y. C. Joo and S. M. Clark, *Appl. Phys. Lett.*, **101** (2012).

요약(국문초록)

비정질 재료는 규칙적 원자구조의 결정질 재료와 대비되는 무질서한 원자 구조를 가진 재료이다. 특유한 원자구조에서 유발되는 특성 덕분에 다양한 다기능성 전자소자에 적용되고 있다. 우선 상변화 재료라고 분류된 재료들은 극도로 빠른 결정화 속도와 동시에 결정화에 따른 큰 폭의 전기적 특성변화를 보여 상변화 메모리를 구현하는데 응용되고 있다. 비정질 산화물 반도체는 대면적 균일 특성, 투명성 및 높은 캐리어 이동도를 갖고 있어 대면적 디스플레이 용 박막 트랜지스터에 응용된다. 그러나 비정질 재료 기반의 전자소자는 재료 고유의 구조적 불안정성에서 기인한 신뢰성 문제에 시달리고 있다. 비정질 재료는 준안정상 물질이며, 따라서 결정질 재료에서는 관찰되지 않는 다양한 구조적 변화 (구조적 완화, 유리 전이, 결정화)가 발생한다. 이러한 구조적 변화는 시간이나 온도에 따른 특성 변화를 야기하므로, 소자의 신뢰성을 저해하는 심각한 원인으로 작용한다

따라서, 소자 특성과 신뢰성을 향상시키기 위해서는 비정질 재료의 구조적 안정성을 이해하고 조정하는 것이 필요하다. 실시간 기계적 응력 측정법을 이용하여 온도와 시간에 따른 비정질 재료의 구조적 변화를 측정하였으며, 원자 결합구조와 재료 특성의 물리적 연계를 통해 구조적 변화 결과의 이론적 해석 기반을 마련하였다.

상변화 메모리의 스위칭 속도(SET speed)를 높이고 정보 보유시간(data retention time)을 향상시키기 위해서는 비정질 상변화 재료의 결정화 거동을 연구해야 한다. 상변화 재료의 결정화 거동은 특유의 액체와 같은 특성에 기인하여 고온 구간에서 재료 물성이 민감하게 변화하는 비아레니우스(non-Arrhenius) 거동을 보인다. 따라서 일반적인 아레니우스 결정화 거동의 분석법에 비해 실험적 또는 이론적인

어려움이 있다. 본 연구에서는 기계적 응력 측정법을 이용하여 다양한 물질로 도핑 된 비정질 $Ge_2Sb_2Te_5$ (GST) 박막의 결정화 온도(T_x), 유리 전이 온도(T_g) 과냉각 액체 영역($T_x - T_g$)을 측정하였다. 또한 T_g의 가열 속도 의존성으로부터 점도(viscosity) 및 프레질리티(fragiltiy)를 측정하여, 이를 통해 비정질 GST 박막의 원자 이동 특성을 정량적으로 도출하였다. 도펀트의 효과는 침입형(interstitial) 도핑과 치환형(substitutional) 도핑에 대해 각각 자유 체적 영향과 결합 엔탈피의 영향으로 나누어 기구를 제시하였다. 도핑에 따른 상변화 메모리의 스위칭 속도, 정보 보유시간은 각각 도핑에 따른 원자 이동도와 열 안정성과 일치하는 경향을 보였다.

비정질 GST 가 상온 또는 비교적 높은 온도에서 시간에 따라 점차적으로저항이 증가하는 현상은 상변화 메모리의 신뢰성 문제를 유발하며, 이를 저항 표류현상(resistance drift)이라고 한다. 저항 표류현상의 근본적인 원인은 여러 모델을 이용하여 제시되었는데, 대표적으로 결함 소멸 모델(defect annihilation model)과 밴드갭 변형 모델(strained bandgap model)이 있다. 본 연구에서는 기계적 응력 및 전기 저항의 실시간 측정을 실시하여 구조적 완화 현상과 저항 표류현상 사이의 관계를 규명하였다. 위에 제시된 이론적 모델에 따라 측정된 기계적 응력으로부터 시간에 따른 저항변화를 계산하여 측정된 저항 값과 비교했다. 결론적으로 구조 완화에 의해 유도된 결함 소멸을 이용해 정량적으로 저항 표류현상을 설명하였다.

비정질 In-Ga-Zn-O (a-IGZO)는 박막 트랜지스터의 활물질로 매우 유망하지만, 표면에서 유발되는 구조적 불안정성이 신뢰성 문제를 유발할 수 있다. 본 연구에서는 표면 불안정성이 구조적 안정성에 주는 영향을 연구하기 위해 a-IGZO 박막의 두께를 변화시켜 표면적 대 체적비를 변화시켰다. 두께가 얇아지면 불안정한 표면층의 영향으로 T_g 가 감소하고 프레질리티가 증가하는 것을 정량적으로 측정하였다.

본 연구는 기계적 응력 측정법을 사용하여 비정질 반도체의 구조적 변화를 측정 및 분석하고, 원자 결합구조와의 연관성을 규명한 연구이다. 이를 통해 소자의 성능과 신뢰성을 향상시키기 위한 비정질 재료 설계에 대한 기준을 제시하였다.

표제어: 비정질 재료, 결정화 거동, 상변화 메모리 (PcRAM), $Ge_2Sb_2Te_5$, In-Ga-Zn-O, 기계적 응력 측정

학 번: 2009-20641

CURRICULUM VITAE

Ju-Young Cho

EDUCATION

2009. 3. ~ **Seoul National University**

Seoul, Korea

Ph. D. candidate in Materials Science and Engineering

Research on structural stability of amorphous materials for electronic devices investigated by mechanical analysis

Advisor: Young-Chang Joo, Professor

2009. 2. **Seoul National University** Seoul, Korea

B. S. in Materials Science and Engineering

RESEARCH EXPERIENCES

Analysis on structural stability of amorphous materials for electronic devices

- Mechanical analysis of doping effect on crystallization, glass transition and structural relaxation of amorphous chalcogenide for phase-change random access memories (PcRAM)
- Theoretical study to correlate material properties to electronic devices characteristics
- Investigation of surface instability in amorphous oxide semiconductors
- Measurement of thermo-mechanical properties of thin films (real-time substrate curvature method)

- Investigation of structural stability of amorphous materials: Viscosity and fragility measurement from stress analysis

Correlating mechanical and electrical properties of materials

- Experimental and theoretical analysis on the change of electrical resistance and structural relaxation in amorphous chalcogenide
- Mechano-resistive behaviors of PEDOT:PSS film for flexible electrode

Atomic migration in chalcogenide materials

- Identifying mass-transport behavior in phase change material during PcRAM operation
- Improving the stability of phase change materials by adding dopants

AWARDS AND HONORS

2013 **Outstanding Poster Presentation Award**, 2013 European Symposium on Phase Change and Ovonic Science (E\PCOS), Berlin, Germany

2013 **Best Poster Presentation Award**, MLC-PRAM Technical Forum, Seoul, Korea

2012 **Best Presentation Silver Medal**, 2012 Fall Conference of the Korean Institute of Metals and Materials, Changwon, Korea

2011 ~ **Ph. D. Scholarship**, Samsung Electronics Co., Ltd., Korea

2009 **Best Presentation Award**, 2009 Korea-Japan-China Student Workshop, Beijing, China

2007 **United States Army Commendation Medal (ARCOM)**, Korean Augmentation Troops to the United States Army (KATUSA), Korea

PROFESSIONAL ACTIVITIES

2011 **Conference Staff Outstanding Poster Presentation Award**

2011 IEEE - International Symposium on the Physical and Failure Analysis of Integrated Circuits (IPFA), Incheon, Korea

2005 ~ 2007 **Mandatory Military Service**

Sergeant, Korean Augmentation Troops to the United States Army (KATUSA), Korea

PUBLICATIONS

- Mechanical analysis on glass transition and crystallization kinetics of Al, Bi, C and N-doped $Ge_2Sb_2Te_5$ films for prediction of phase-change memory characteristics, **J.-Y. Cho**, D.-H. Kim, Y.-J. Park, T.-Y. Yang, Y.-Y. Lee, and Y.-C. Joo*, *in preparation*
- Doping-induced elastic strain energy in crystalline $Ge_2Sb_2Te_5$ films, **J.-Y. Cho**, Y.-J. Park, H.-Y. Kim, D.-H. Kim, Y.-Y. Lee, and Y.-C. Joo*, *in preparation*
- Structural instability in amorphous In-Ga-Zn-O films investigated by mechanical stress analysis, **J.-Y. Cho**, T.-Y. Yang, Y.-J. Park, Y.-Y. Lee, and Y.-C. Joo*, *ECS Solid-State Lett.*, 3 (6) (2014)
- Study on the resistance drift in amorphous $Ge_2Sb_2Te_5$ according to defect annihilation and stress relaxation, **J.-Y. Cho**, T.-Y. Yang, Y.-J. Park and Y.-C. Joo*, *Electrochem. Solid-State Lett.*, 15 (4) (2012)
- Electrical current-induced gradual failure of crystalline $Ge_2Sb_2Te_5$ for phase-change memory, Y.-J. Park, T.-Y. Yang, **J.-Y. Cho**, S.-Y. Lee, and Y.-C. Joo*, *Appl. Phys. Lett.*, 103, 073503 (2013)

- Stretching-induced growth of PEDOT-rich cores: A new mechanism for strain-dependent resistivity change in PEDOT:PSS films, Y.-Y. Lee, J.-H. Lee, **J.-Y. Cho**, N.-R. Kim, D.-H. Nam, I.-S. Choi*, K. T. Nam*, and Y.-C. Joo*, *Adv. Funct. Mater.*, 23 (32) (2013)
- Driving forces for elemental demixing of GeSbTe in phase-change memory: Computational study to design a durable device, T.-Y. Yang, **J.-Y Cho**, Y.-J. Park, and Y.-C. Joo*, *Curr. Appl. Phys.*, 13 (7) (2013)
- Observation of polyamorphism in the phase change alloy $Ge_1Sb_2Te_4$, B. Kalkan, S. Sen, **J.-Y. Cho**, Y.-C. Joo and S. M. Clark*, *Appl. Phys. Lett.*, 101, 151906 (2012)
- Influence of dopants on atomic migration and void formation in molten $Ge_2Sb_2Te_5$ under high-amplitude electrical pulse, T.-Y. Yang, **J.-Y. Cho**, Y.-J. Park, and Y.-C. Joo*, *Acta Mater.*, 60 (5) (2012)
- Te-centric view of the phase change mechanism in Ge-Sb-Te alloys, S. Sen*, T. G. Edwards, **J.-Y. Cho** and Y.-C. Joo, *Phys. Rev. Lett.*, 108 (19) (2012)
- Thermomechanical analysis on the phase stability of nitrogen-doped amorphous $Ge_2Sb_2Te_5$ films, I.-M. Park, **J.-Y. Cho**, T.-Y. Yang, E. S. Park and Y.-C. Joo*, *Jpn. J. Appl. Phys.*, 50 (6 part 1) (2011)
- Inhibition of the electrostatic force-induced atomic migration in $Ge_2Sb_2Te_5$ by nitrogen doping, T.-Y. Yang, **J.-Y. Cho**, and Y.-C. Joo*, *Electrochem. Solid-State Lett.*, 13 (9) (2010)

PRESENTATIONS IN INTERNATIONAL CONFERENCE

Oral Presentations

- Thermal instability of amorphous In-Ga-Zn-O thin film related to glass stability, **J.-Y. Cho**, T.-Y. Yang, Y.-J. Park, and Y.-C. Joo, 2012 Fall Conference of the Korean Institute of Metals and Materials, 2012. 10. 26., Changwon, Korea, *Best presentation award*

- Effect of defect annihilation and stress relaxation on the resistance drift in amorphous $Ge_2Sb_2Te_5$, **J.-Y. Cho**, T.-Y. Yang, Y.-J. Park, and Y.-C. Joo, 2012 Materials Research Society (MRS) Spring Meeting, 2012. 4. 10., San Francisco, USA
- Study of doping effect on the phase stability of amorphous $Ge_2Sb_2Te_5$ through the thermomechanical and electrical measurements, **J.-Y. Cho**, T.-Y. Yang, Y.-J. Park, and Y.-C. Joo, 2011 Materials Research Society (MRS) Spring Meeting, 2011. 4. 25., San Francisco, USA
- Effects of doping on the crystallization characteristics of $Ge_2Sb_2Te_5$ thin film for phase change nonvolatile memory, **J.-Y. Cho**, T.-Y. Yang, Y.-J. Park, and Y.-C. Joo, 18th Korean Conference on Semiconductors, 2011. 2. 16., Seogwipo, Korea
- Electric current-induced atomic migration and failure mechanism in crystalline Bi-Te alloy, Y.-J. Park, T.-Y. Yang, **J.-Y. Cho**, and Y.-C. Joo, 2012 Materials Research Society (MRS) Fall Meeting, 2012. 11. 27., Boston, USA
- Effect of defect annihilation and stress relaxation on the resistance drift in amorphous $Ge_2Sb_2Te_5$, Y.-C. Joo, T.-Y. Yang, **J.-Y. Cho**, and Y.-J. Park, 2012 Materials Research Society (MRS) Spring Meeting, 2012. 4. 12., San Francisco, USA
- Effect of mechanical deformation on the electrical properties of PEDOT:PSS films, Y.-Y. Lee, J.-H. Lee, N.-R. Kim, **J.-Y. Cho**, K. T. Nam, and Y.-C. Joo, 2011 Materials Research Society (MRS) Fall Meeting, 2011. 11. 29., Boston, USA
- Comparison of current-induced atomic migration between intermetallic and eutectic phase in crystalline states of chalcogenide, Y.-J. Park, T.-Y. Yang, **J.-Y. Cho**, and Y.-C. Joo, 2011 Materials Research Society (MRS) Spring Meeting, 2011. 4. 27., San Francisco, USA
- Change of electric-field-induced atomic mobility and void volume by controlling defect density in GeSbTe compounds, T.-Y. Yang, **J.-Y. Cho**, Y.-J. Park, and Y.-C. Joo, 2011 Materials Research Society (MRS) Spring Meeting, 2011. 4. 25., San Francisco, USA

- Effects of dopings on the electric-field-induced atomic migration and void formation in $Ge_2Sb_2Te_5$, T.-Y. Yang, **J.-Y. Cho**, Y.-J. Park, and Y.-C. Joo, 2011 IEEE - International Symposium on the Physical and Failure Analysis of Integrated Circuits (IPFA), 2011. 7. 4., Incheon, Korea
- Electric-field-enhanced atomic transport in phase change materials as the origin of the set-stuck failure in PRAM, Y.-C. Joo, T.-Y. Yang, **J.-Y. Cho**, and Y.-J. Park, 2010 European Symposium on Phase Change and Ovonic Science (E\PCOS), 2010. 9. 7., Milano, Italy, *Outstanding presentation award*
- Electromigration in GeSbTe-based chalcogenide materials under pulsed DC for set-stuck failure, T.-Y. Yang, **J.-Y. Cho**, and Y.-C. Joo, 2010 Materials Research Society (MRS) Spring Meeting, 2010. 4. 8., San Francisco, USA

Poster Presentations

- Stability of amorphous chalcogenide materials: phase transition and fragility, **J.-Y. Cho**, T.-Y. Yang, Y.-J. Park, and Y.-C. Joo, 2013 European Symposium on Phase Change and Ovonic Science (E\PCOS), 2013. 9. 8., Berlin, Germany, *Invited poster*, *Outstanding poster presentation award*
- Thermally-induced structural instability and phase transition characteristics in amorphous In-Ga-Zn-O thin film determined by mechanical stress analysis, **J.-Y. Cho**, T.-Y. Yang, Y.-J. Park, Y.-Y. Lee, and Y.-C. Joo, 2013 Materials Research Society (MRS) Spring Meeting, 2013. 4. 2., San Francisco, USA
- Analysis on mechanism of structural relaxation in amorphous $Ge_2Sb_2Te_5$ doped with Bi and N using thermomechanical measurement, **J.-Y. Cho**, T.-Y. Yang, and Y.-C. Joo, 2010 Materials Research Society (MRS) Spring Meeting, 2010. 4. 6., San Francisco, USA

- Gradual change of resistance on high current density induced by nano-scaled voids in the crystalline phase of $Ge_2Sb_2Te_5$, Y.-J. Park, T.-Y. Yang, **J.-Y. Cho**, and Y.-C. Joo, 2013 European Symposium on Phase Change and Ovonic Science (E\PCOS), 2013. 9. 8., Berlin, Germany
- Strong correlation between the resistivity and uniaxial strain on PEDOT:PSS films: Stretching induced growth of PEDOT-rich cores, Y.-Y. Lee, J.-H. Lee, **J.-Y. Cho**, N.-R. Kim, D.-H. Nam, I.-S. Choi, K. T. Nam, and Y.-C. Joo, 2013 Materials Research Society (MRS) Spring Meeting, 2013. 4. 4., San Francisco, USA
- Driving forces of mass transport in phase change materials and their effect on device failures, Y.-C. Joo, T.-Y. Yang, **J.-Y. Cho**, and Y.-J. Park, 2011 European Symposium on Phase Change and Ovonic Science (E\PCOS), 2011. 9. 5., Zurich, Switzerland, *Invited poster*, *Outstanding poster presentation award*

R&D PROJECTS

- "Development of High Performance Phase Change Materials", IT R&D Program funded by Ministry of Trade, Industry and Energy / Korea Evaluation Institute of Industry Technology, 2014. 3. ~ 2015. 2.
- "Improvement of Reliability in Phase-change Random Access Memory through Investigation of Failure Mechanisms", Cooperative System Project funded by Samsung Electronics Co., Ltd., 2010. 7. ~ 2015. 6.
- "Interfacial Property Test and Structural Design Technology for Thin Film Solar Cell", The Converging Research Center Program funded by the Ministry of Education, Science and Technology, 2010. 11. ~ 2014. 6.
- "Phase-change Random Access Memory Development", The National Research Project funded by Ministry of Commerce, Industry and Energy, 2005. 11. ~ 2010. 4.